Design, Modeling, and Optimization of Thin and Ultra-thin Photonic Power Converters Operating at 1310 nm Laser Illumination

by

Neda Nouri

Thesis submitted to the University of Ottawa in partial fulfillment of the

requirements for the degree of

Doctor of Philosophy

in

Electrical Engineering

Department of Electrical Engineering and Computer Science, Faculty of Engineering
University of Ottawa

Dedicated to my parents

Abstract

Photonic power converters (PPCs) are one of the main components of optical power transmission systems, converting optical power injected by a monochromatic optical source (laser or LED) to electrical power via the photovoltaic effect. This thesis focuses on designing and optimizing ultra-thin single junction InAlGaAs PPC with integrated back reflectors (BR) for operation at the telecommunications wavelength of 1310 nm and numerically studies the light trapping capability of three BR types: planar, cubic nanotextured, and pyramidal nanotextured. Optical simulations were performed by coupling finite difference time-domain (FDTD) calculations with a particle swarm optimization, while electrical simulations were carried out by the finite element drift-diffusion method. With 90% absorptance, optoelectrical simulations revealed that ultra-thin PPCs with 5.6- to 8.4-fold thinner absorber layers can have open circuit voltages (V_{oc}) that are 9-12% larger and power conversion efficiencies that are 9-10% (relative) larger than conventional thick PPCs. Of the studied BR designs, pyramidal BRs exhibit the highest performance for ultra-thin designs, reaching an efficiency of 43.2% with 90% absorptance, demonstrating the superior light trapping capability relative to planar and cubic nanotextured BRs.

The sensitivity of optical absorptance to variations in device thickness and incident light wavelength is also investigated numerically in thin PPCs with planar and pyramidal nanotextured BRs. Optical simulation results revealed that BR-induced resonances shift from constructive to destructive interference with thickness variations of ~100 nm and ~70 nm in planar and pyramidal nanotextured BRs, respectively. Also in PPCs with pyramidal BR, a 50 nm variation of the nanotextures' geometry (base width and height of pyramids) drops the absorptance by more than 25% (absolute).

Acknowledgments

First, I would like to express my sincere appreciation and thanks to my supervisor Prof. Karin Hinzer for her guidance, support, and inspiration over the course of my Ph.D. study. Karin's faith in me not only helped me in my academic career but also led me to build a positive attitude and strong personality in my personal life.

My special thanks go to Dr. Christopher Valdivia, for his patience, precious time, valuable guidance, insightful feedback, and discussions throughout my research, including enormous help in preparing manuscripts.

I am very thankful to my thesis proposal committee members Prof. Henry Schriemer and Prof. Winnie Ye for their constructive comments, suggestions, and advice that helped to shape this thesis for the better.

I would like to thank Prof. Jacob Krich for his insightful comments, help with the interpretation of results, and fruitful discussions. Also thank you to Dr. Meghan Beattie for sharing her experimental results, valuable conversations, and suggestions.

I would like to thank all SUNLAB members and my Iranian friends for their personal and research-related support which made my Ph.D. study period fun and joyful.

Finally, a heartfelt thank you to my parents and siblings, who gave me the strength to pursue my dreams, for their unconditional love and endless support, as well as my niece and nephews who were sources of joy and motivation and always knew how to cheer me up.

This project was accomplished with financial support provided by the Natural Sciences and Engineering Research Council of Canada (NSERC) award Number 497981 through the TOP-SET program. I am also thankful to the University of Ottawa for my International Admission Scholarship and International Doctoral Scholarship.

Statement of Original Contributions

The presented results in this thesis were obtained throughout my Ph.D. research project, under the supervision of Prof. Karin Hinzer. To the best of my knowledge the results are original. Chapters 1 and 2 provide background information from the literature. Material selection for modeled PPCs in Chapter 3 and all the experimental data for simulation was taken from Meghan Beattie's thesis where she conducted the experiments. Chapters 4, 5 and 6 are original contributions to the field. I undertook this work myself unless explicitly mentioned. The following is a breakdown of contributions for all papers resulting from this thesis that are included within the body of this thesis:

- I was the main author of the text and generated all figures.
- I designed thin PPC models and performed optoelectronic simulations.
- Modeled device material selection and experimental data including (*n*, *k* values and *I*-*V* curve) was performed by Meghan Beattie.
- Manuscript editing and reviewing were performed by Christopher Valdivia, Meghan Beattie, and Jacob Krich.
- Supervision was done by Karin Hinzer.

The work presented in this thesis led to the following publications and presentations:

List of Publications

Journals papers

N. Nouri, C. E. Valdivia, M. N. Beattie, J. J. Krich, and K. Hinzer, " Light management in ultra-thin photonic power converters for 1310 nm laser illumination". *Optics Express* **30** (13), 23417-23427 (2022).

Conference proceedings

1. **N. Nouri**, C. E. Valdivia, M. N. Beattie, J. J. Krich, and K. Hinzer, "Optical design considerations for thin photonic power converters with textured back reflector", in *2022 49th IEEE Photovoltaic Specialists Conference (PVSC)*, 1295-1298, (2022).

2. **N. Nouri**, C. E. Valdivia, M. N. Beattie, M. Zamiri, and K. Hinzer, "Thin photonic power converters designs with back reflector operating at 1310 nm wavelength", *in 2020 47th IEEE Photovoltaic Specialists Conference (PVSC)*, 2359-2362, (2020).

Conference presentations

1. M. N. Beattie, **N. Nouri**, H. Helmers, G. P. Forcade, C. E. Valdivia, O. Höhn, J. J. Krich, and K. Hinzer, " Strategies for high-performance O-band photonic power converters", In *Photonics West in the Physics, Simulation, and Photonic Engineering of Photovoltaic Devices XII conference* (Submitted)

2. **N. Nouri**, C. E. Valdivia, M. N. Beattie, J. J. Krich, and K. Hinzer, "Optical design considerations for thin photonic power converters with textured back reflector", *in 2022 49th IEEE Photovoltaic Specialists Conference (PVSC)*, Philadelphia, PA, June 5-10, 2022. (Poster)

3. N. P. Irvin, **N. Nouri**, C. Zhang, C. E. Valdivia, K. Hinzer, Richard R. King, C. B. Honsberg," Monochromatic light trapping in photonic power converters", *in 2022 49th IEEE Photovoltaic Specialists Conference (PVSC)*, Philadelphia, PA, June 5-10, 2022. (Oral)

4. **N. Nouri,** C. E. Valdivia, M. N. Beattie, N. P. Irvin, C. Zhang, R. R. King, C. B. Honsberg, J. J. Krich, and K. Hinzer, "Tolerance study of thin photonic power converters with planar back reflectors", 4th Optical Wireless and Fiber Power Transmission Conference, Online/Japan, April 18-21, 2022. (Oral)

5. **N. Nouri,** C. E. Valdivia, M. N. Beattie, M. Zamiri, and K. Hinzer. "Ultra-thin monochromatic photonic power converters with nanostructured back mirror for light trapping of 1310 nm laser

illumination", In *Physics, Simulation, and Photonic Engineering of Photovoltaic Devices X*, vol. 11681, p. 116810X. SPIE, 2021. (Oral)

6. **N. Nouri**, C. E. Valdivia, M. N. Beattie, M. Zamiri, and K. Hinzer, "Thin photonic power converters designs with back reflector operating at 1310 nm wavelength", *in 2020 47th IEEE Photovoltaic Specialists Conference (PVSC)*, 2020. (Oral)

7. **N. Nouri**, "Modeling of Highly Efficient Thin Photonic Power Converters Operating at 1310 nm", *Engineering and Computer Science Graduate Poster Competition*, University of Ottawa, 2020 (**Winner, IEEE First place prize**)

8. **N. Nouri**, C. E. Valdivia, M. N. Beattie, M. S. Zamiri, and K. Hinzer, "Simulation of thin high-efficiency photonic power converters under 1310 nm laser illumination", 19th International Conference on Numerical Simulation of Optoelectronic Devices, Ottawa, ON, July 8 to 12, 2019. (Poster)

9. M. Zamiri, **N. Nouri**, K. Kaller, M. N. Beattie, M. M. Wilkins, C. E. Valdivia, B. Lessard, Z. R. Wasilewski, and K. Hinzer, "Design for fabrication of high efficiency 1310 nm photonic power converter", 19th International Conference on Numerical Simulation of Optoelectronic Devices, Ottawa, ON, July 8 to 12, 2019. (Poster)

Table of Contents

List of Figures

List of Tables

List of Acronyms

2D	Two-dimensional
3D	Three-dimensional
ARC	Anti-reflection coating
ASF	Angular selective filter
BR	Back reflector
BSF	Back surface field
DLARC	Double layer anti-reflection coating
EQE	External quantum efficiency
FBR	Flat back reflector
FDTD	Finite Difference Time Domain
FF	Fill factor
FSF	Front surface field
PCE	Power conversion efficiency
PPC	Photonic power converter
PML	Perfectly matched layer
SRH	Shockley-Read-Hall
TBR	Textured back reflector

List of Symbols

a	Lattice constant
A	Absorptance
B_{rad}	Radiative recombination coefficient
c	Speed of light in vacuum
C_n, C_p	Electrons/holes capture rate coefficient for Auger recombination
D	Diffusion coefficient
e-h	electron-hole pair
E	Energy
E_F	Fermi level
E_{Fn}, E_{Fp}	Quasi-Fermi level of electrons/holes
E_g	Bandgap energy
E_{ph}	Energy of the incident photon
E_t	Trap state energy
E_v	Valence band edge
E_{vac}	Vacuum level
f	Lattice misfit
G	Generation rate
$\hbar$	Planck's constant
I_0	Dark saturation current
J_{ph}	Photocurrent
$J_{ph,th}$	Theoretical photocurrent

J_{SC}	Short-circuit current density
J_{dark}	Dark current density
k_B	Boltzmann constant
L	Diffusion length
n	Density of electrons
n_r	Real part of the refractive index
n_i	Intrinsic carrier density
N_c, N_v	Effective density of states for conduction/ valence band
p	Density of holes
P	Power
P_{abs}	Absorbed power
q	Elementary charge
r	Position
$R_{n,p}$	Recombination rate
T	Temperature
v_{th}	Thermal velocity
V_{OC}	Open-circuit voltage
x	Mole fraction
μ	Mobility
σ	Capture cross-section
Φ	Work function
w_n, w_p	Depletion widths for n-/p-type material
τ_n, τ_p	Lifetime of electrons/holes

τ_{SRH}	SRH recombination lifetime
τ_{rad}	Radiative recombination lifetime
τ_{Aug}	Auger recombination lifetime
μ_n, μ_p	Mobility of electrons/holes
ε_0	Permittivity of free space
η	Optical-to-electrical conversion efficiency
κ	Extinction coefficient
λ	Wavelength

Chapter

1 INTRODUCTION

Photovoltaic device applications are not limited to electrical power generation from sunlight. Over the past few decades, it has been shown that converting laser power to electricity yields higher conversion efficiency than solar cells. This is enabled by tuning the absorber layer bandgap to the incident light wavelength. It also can be used as a suitable alternative to copper wire powering where it is not safe or applicable. This chapter comprises an introduction to the photonic power converter (PPC) and its applications. In particular, this chapter discusses thin PPCs and the selection of operational wavelength for this thesis.

1.1 Introduction

Well-known for its revolutionary role in high-speed data transmission, optical fiber has demonstrated significant potential for optical power transmission applications in recent years. The efficiency of optical power transmission systems is less than half of the efficiency of conventional copper wire power transmission. However, electromagnetic interference immunity, galvanic isolation, and reduced fire hazard make optical fiber a safe and reliable power transmission alternative for driving sensors and low power electronics in hazardous and extreme environments such as near high voltage lines or in wind turbines, mines, and magnetic resonance imaging machines [1]–[5].

Besides power over fiber, free space optical power transmission (power beaming) also gained lots of attention for a wide range of applications [6]. Some applications include remote powering of equipment for which replacing the battery is challenging, inconvenient, or dangerous such as subcutaneous devices [7], [8], or electronics mounted across borders or within war zones [9]. Power beaming can also be used where wires are impractical such as for sensors mounted on rapidly oscillating mechanical parts [10]. There is also potential use in aerospace industry through harnessing sun power and beaming it to the earth in the form of laser to power moving objects such as aircrafts [11], [12].

A typical optical power transmission system consists of a narrowband light source such as a laser or LED, an optical fiber or free space optics, and a photonic power converter (PPC) -also called laser power converter- to convert photonic power into electrical power via the photovoltaic effect (Fig. 1.1). Depending on the applications of optical power transmission systems, operational wavelengths of PPCs vary. Fig. 1.2. depicts the attenuation loss of the single mode silica-based optical fiber as a function of the wavelength with highlighted three main telecommunication windows. For fiber-based optical power transmission applications, PPC design requires to be compatible with these three main wavelengths (850 nm, 1310 nm and 1550 nm) where light has minimum attenuation loss passing through the fiber [13]. For power beaming from space, wavelengths of interest lie around 1500 nm and 2100 nm, as at these wavelengths attenuation through Earth's atmosphere is minimized [14]. For powering of subcutaneous equipment, the

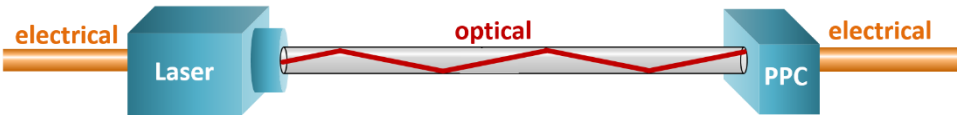

Figure 1.1: Schematic of the optical power transmission system (PPC: Photonic power converter).

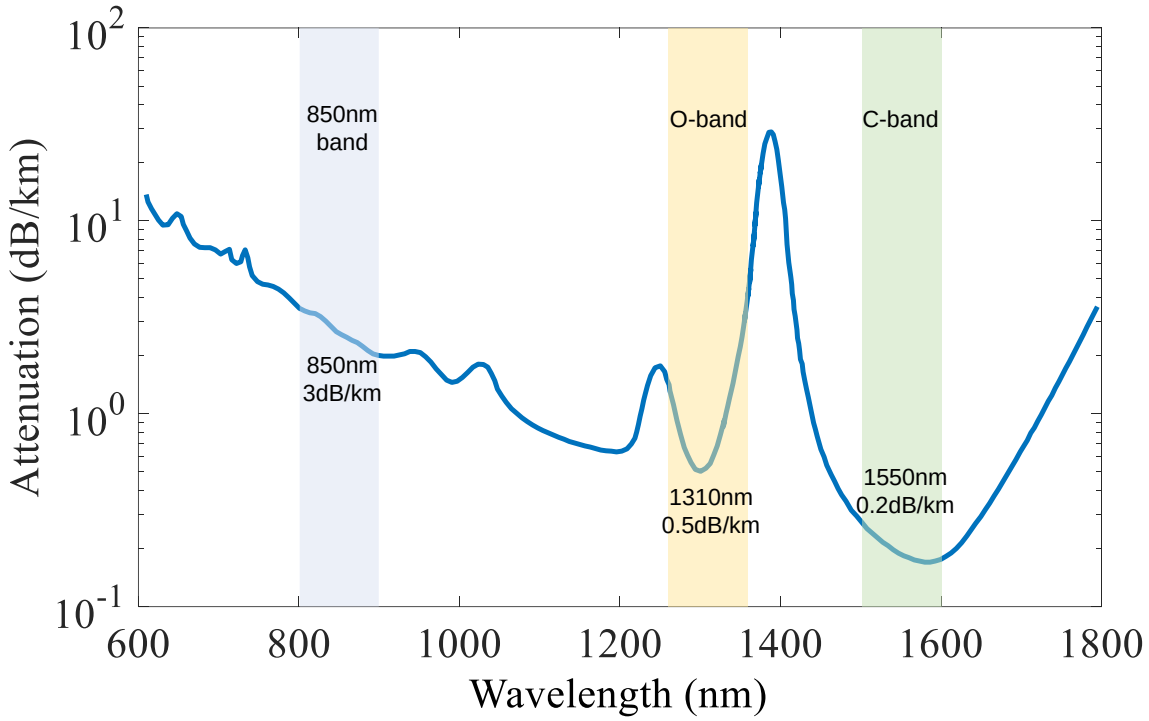

Figure 1.2: Single mode silica optical fiber attenuation versus wavelength. The key telecommunication wavelengths are highlighted.

irradiation safety to human beings matters. It has been shown that wavelengths above 1400 nm under irradiation intensity of 1kW/m^2 are both eye and skin safe [15].

The output voltage of PPCs is directly related to the bandgap of their absorbing material. For most applications, this is not sufficiently high. To boost the output voltage of PPCs to meet application requirements, they can be designed as devices with a single pn junction and combined with conventional DC-DC converters [16], or as stand-alone multi-junction devices which directly output voltages that scale linearly with the number of series-connected pn junctions [17], [18]. In both cases, the ability of the PPC to absorb the majority of incident irradiance is critical to achieving a high optical-to-electrical power conversion efficiency. As transmittance decreases exponentially with active layer thickness [19] , fulfilling high absorption requirements (> 90% of incoming light) typically requires absorber layers with thicknesses on the order of at least several micrometers. Absorptance versus thickness for single and multijunction PPCs for a material with

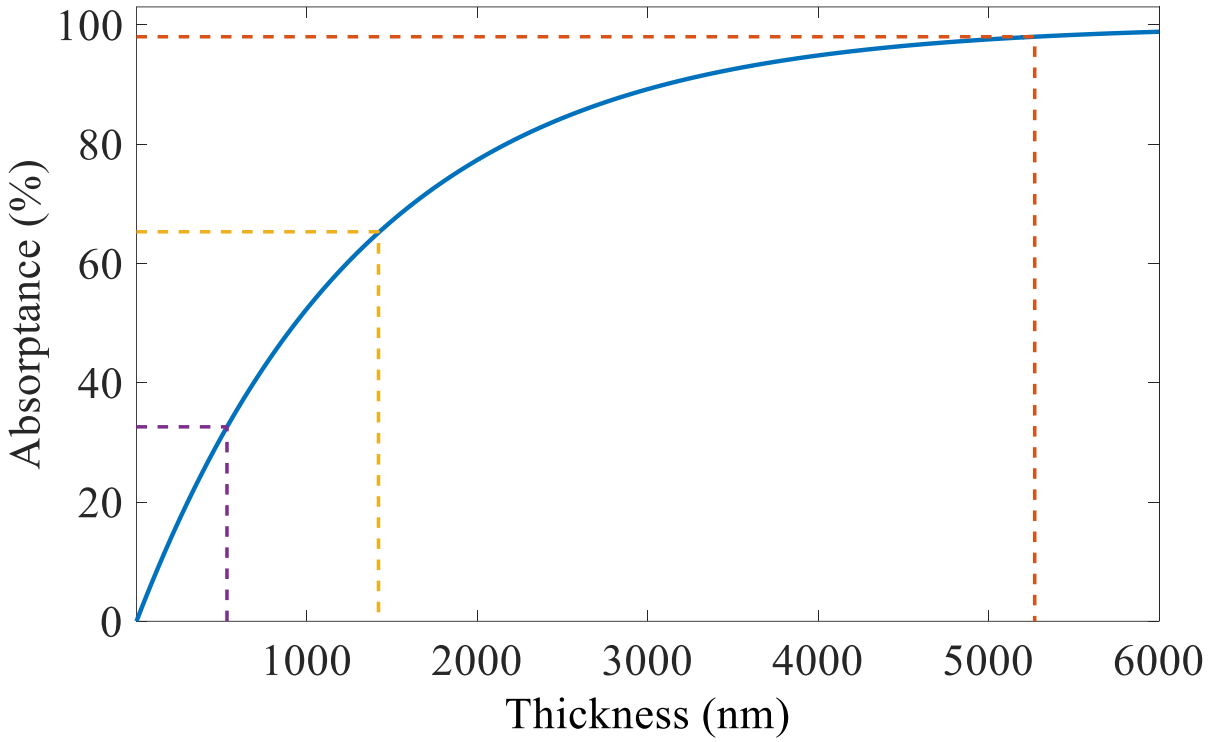

Figure 1.3: Light absorption versus thickness through a material with an absorption coefficient of 7424 cm^{-1} (blue line). 98% absorption corresponds to 5300 nm material thickness (red dashed line). The dashed lines correspond to 3 junction PPC thickness allocation to satisfy same current absorption at each junction.

an absorption coefficient of 7424 cm^{-1} at 1310 nm are illustrated in Fig. 1.3. This value was chosen based on experimental measurements by Dr. Meghan Beattie [20]. An alternative solution is to reduce the PPC thickness and apply light trapping techniques to compensate for the reduced absorption within the thin absorber. In addition to faster epitaxial growth and reduced material usage, thin devices benefit from higher open circuit voltages (V_{oc}) compared to thick devices due to increased carrier concentration and reduced bulk recombination [21] . They are less sensitive to bulk defects and are not limited by diffusion length [22]. An added benefit of thin devices is their enhanced power-to-weight ratio, flexibility, and superior radiation tolerance, which are critical for aerospace applications [23], [24]. The efficiency of thin PPCs is expected to exceed that of their optically thick counterparts when high absorption can be maintained through efficient light trapping.

1.2 Literature review

I listed some of the PPC devices with remarkable efficiencies at different wavelengths in Table 1.1. The record efficiencies for multi junction and single junction PPCs belong to GaAs based PPCs with efficiencies of 74.7% and 68.9%, respectively [25], [26]. It should be noted that PPCs operating at longer wavelengths fundamentally have lower efficiency than PPCs operating at shorter wavelengths due to the lower photon energy.

Table 1.1: PPC devices operating at different wavelengths

Wavelength (nm)	Material	Number of junctions	Output Voltage (V)	Intensity (W/cm^2)	Efficiency (%)	Ref.	year
808 nm	GaAs	5	7.18	6.75	74.7%	[25]	2022
809	AlGaAs/GaAs	Single	1.19	-	60	[27]	2016
830 nm	GaAs	5	>5	8	70%	[17]	2016
850 nm	GaAs	20	>23	36.5	60%	[28]	2016
858 nm	GaAs	Single	1.2	11.4	68.9%	[26]	2021
1064	InGaAs/GaAs	Single	0.8	-	44.1	[29]	2022
1070	InAlGaAs/InP	Single	0.8	0.16	40.7%	[30]	2016
1310	InGaAsP/InP	Single	-	10	51.1	[31]	2020
1470	InGaAs/InP	10	5.46	-	48.9	[32]	2022
1550	InGaAsP/InP	Single	-	0.1	44.6	[33]	2013
2100	InGaAs/InP	Single	0.29	3.78	22	[10]	1997

Numerous light harvesting strategies have been exploited for high-efficiency thin and ultra-thin solar cells including metal nano particles [34], [35], photonic crystals and gratings [36], [37],

nano pyramids [38], [39] nanocones [40], nanowires [41], and planar or patterned metal back reflectors (BRs) [42]–[44] or combinations of them [45]. Fig. 1.4 shows schematic diagram of several photonic nanostructure configurations that can be used to improve solar cell performance [46]. Among these methods, front surface texturing alone or in combination with rear mirroring is very common. Fig. 1.5 shows light ray propagation, reflection and hence light path enhancement using BR, and combination of BR with random and periodic front surface nanotexturing [47]. Besides trapping light, front surface texturing can decrease reflection losses across the broad solar spectrum.

While light trapping techniques for solar cells have been investigated extensively over the last few decades, there are only a few recent studies targeting thin PPCs. In 2020, Takeda [48] proposed that the combination of an angular selective filter (ASF) with diffuse BR enabled trapping of all illuminated light from the top and most reflected light from the back side with the exception of normally incident light (Fig 1.). In his work the ASF was comprised of a stack of 42

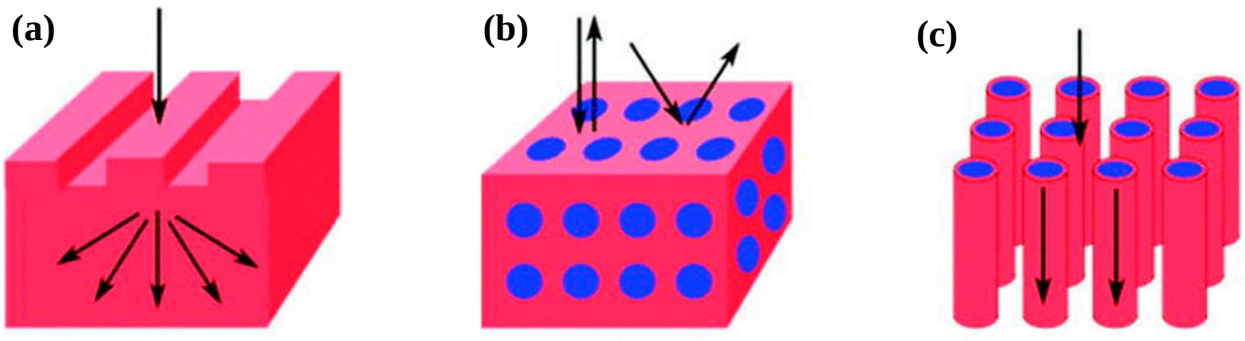

Figure 1.4: Schematic illustrations of nanophotonic structures used to improve solar cell performance: (a) 2D gratings, (b) photonic crystal, and (c) nanowires. Adapted from [46].

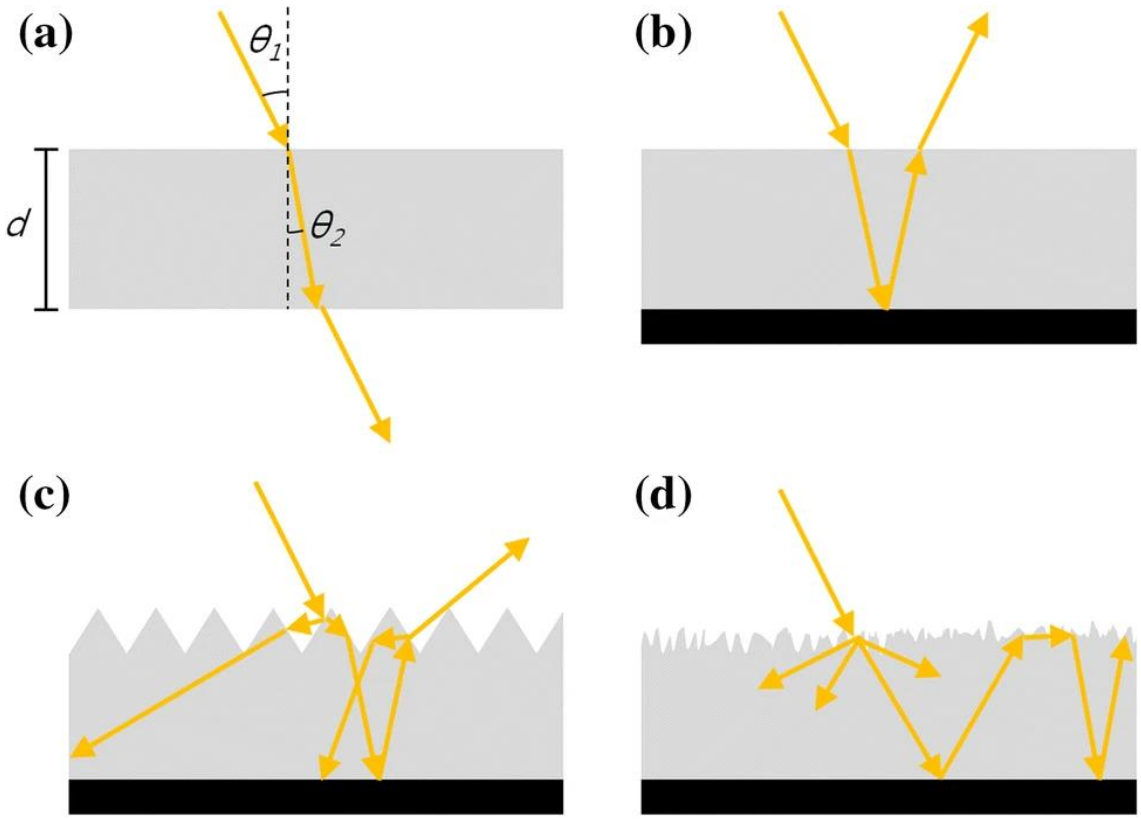

Figure 1.5: Trajectory of light rays through a medium for (a) a single-layer, (b) multi-layer with a planar reflecting layer, (c) periodic texturing on top with a planar reflecting layer, and (d) random texturing on top with a planar reflecting layer. Adapted from [47].

dielectric layers that were optimized to maximize efficiency for GaAs PPC at 872 nm with illumination angles of 0°-5°. His numerical results revealed that for an absorber layer thickness of 35.3 nm, the efficiency can reach up to 81.1% under intensity of 1 W/cm^2. In his research high reflectivity of the rear reflector is determined to be the main priority for high efficiency PPCs. Fabrication of multilayer dielectric is feasible with acceptable accuracy of each layer thickness and is compatible with epitaxial lift off technique for thin film PV cells [49]. However, the efficiency sensitivity to ASF layer thickness variation is not evaluated in this work.

In 2021, Helmers et al. [26] experimentally demonstrated unprecedented efficiency of 68.9% for a thin (1750 nm absorber layer thickness) GaAs PPC at 858 nm under intensity of 11.4 W/cm^2.

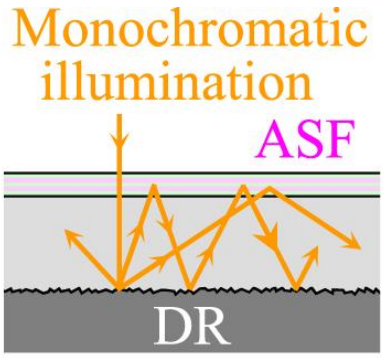

Figure 1.6: Light propagation of normally incident light in a PV cell with configuration of ASF and diffuse reflector. ASF: Angular selective filter, DR: Diffuse reflector. Adapted from [48].

This high efficiency arises from formation of an optical cavity utilizing BR. The optical cavity boosts absorptance near the bandgap by exhibiting a fringe pattern that resulted from BR induced Fabry-Perot resonances. Another impact of the optical cavity is that generated photons from radiative recombination are trapped inside the absorber region and can be reabsorbed to contribute to photocurrent generation. This phenomenon is called photon recycling and results in open circuit voltage (V_{oc}) and subsequently efficiency enhancement through both reducing radiative recombination loss and increasing photon concentration. The only drawback of this work was that the optimal performance wavelength was determined after fabrication, whereas the design could have been optimized for a specific wavelength prior to fabrication.

In 2022, Irvin et al. [50] showed theoretically that increasing the optical path-length by 2- to 10- times caused a peak efficiency improvement from 61.7% to 69.4% for a 40 nm thin GaAs PPC. Their study showed that front surface texturing using nanocones and planar silver BR integration yielded an increase in the optical path length of 18.6% corresponding to 62% absorptance, which was only 7% without light trapping. Based on their study, high absorptances implied the presence of Fabry-Perot resonances formed by constructive interference of light at the front interface. Tolerance study of constructive interference and hence absorptance to nanocones geometry showed that slight (3%) deviation in nanocones array pitch results in significant (50%) drop in

absorptance. This implies that this light trapping approach may not be suitable for devices fabricated using common nanolithography techniques. They hypothesized combination of nanocones with other designs such as diffuse BR could result in further light path enhancement and designs less sensitive nanocones pitch variations.

1.3 Thesis objective

The overall efficiency of power over fiber system is the product of the efficiencies of its components: narrow band light source, optical fiber, and PPC. Being a member of the SUNLAB-photovoltaic research group- my PhD research focuses on design of thin yet high efficiency PPCs.

In power over fiber systems with propagation of optical power over 1 km, the fiber attenuation coefficient becomes the most critical design consideration. The majority of commercially available high-efficiency PPCs are based on GaAs absorbers, operating in the range of 800-850 nm wavelengths [28], [51], [52]. The optical fiber attenuation loss at these wavelengths is ~3 dB/km (50% per kilometer), which limits the use of these devices for short-distance power over fiber transmission. Longer wavelengths can significantly extend this reach but require lower bandgap absorbers for which bandgap-voltage offsets represent a larger relative loss, resulting in lower expected maximum optical-to-electrical conversion efficiencies. Nevertheless, this study focuses on the O-band telecommunications window near 1310 nm which provides much lower optical fiber attenuation loss of ~0.5 dB/km (11% per kilometer), resulting in higher total system transmission efficiency in longer-reach photonic power systems [31], [53], [54]. It enables feeding nodes with longer distribution links for internet of things applications [55].

As discussed in section 1.2, BR integration is a common approach for light trapping in both thin broadband and narrowband photovoltaics. Studies on broadband photovoltaics such as solar

cells are mainly focused on increasing the number of BR induced resonances for a broad spectrum of sun light and are usually combined with front surface texturing to reduce reflection loss. In the case of thin PPCs, BR is combined with front filtering or nanocones. The main drawback of the work without front texturing is that the design is not optimized for a specific wavelength, instead

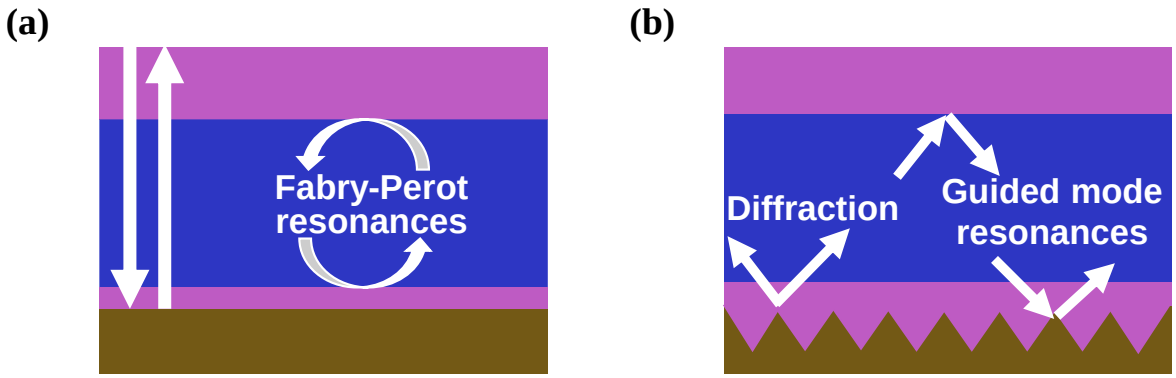

Figure 1.7: Schematic of: (a) Fabry-Perot resonances induced by flat back reflector (b) guided mode resonances induced by textured back reflector.

the optimum operational wavelength was determined after fabrication. In addition, all previously published thin PPC designs were in the 850 nm wavelength region. My goal in this thesis is to design a PPC with near-zero reflection losses and thus high absorptance at 1310 nm. My design uses a back mirror to increase the optical path length and form an optical cavity. The resulting resonances are optimized for 1310 nm, assuming no anti-reflection coating is present. Additionally, the BR can increase the V_{oc} through photon recycling [56], [57]. Besides planar BRs, it has been shown that nanotextured BRs further improve light trapping through inducing guided mode resonances. The BR induced Fabry-Perot and guided mode resonances in the flat and textured BR photovoltaic cells [58] are illustrated schematically in Fig. 1.7.

In this thesis, I numerically investigated the light trapping capability of flat and nanotextured BRs with cubic and pyramidal structures as for 1310 nm, as shown in Fig. 1.8.

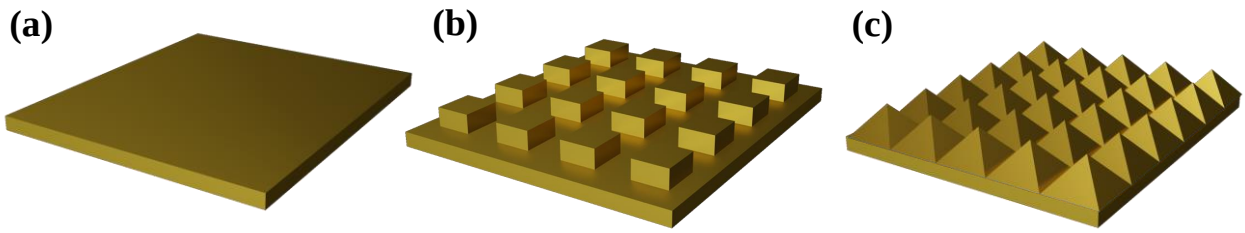

Figure 1.8: Three types of modeled back reflectors (BR): (a) flat BR, (b) Cubic BR, and (c) pyramidal BR.

1.4 Thesis outline

This thesis focuses on the study of light management in ultra-thin PPCs under 1310 nm laser illumination using a BR. The first chapter is an introduction to thin PPCs and light trapping methods. It also includes a literature review and the thesis objective. The theory necessary to provide a better understanding of PPCs, their design, and how to simulate them is explained in chapter 2. This includes the physics of semiconductors and photovoltaic devices, as well as relevant terminologies. Chapter 3 presents the design and characterization of modeled thin PPCs including the material selection for 1310 nm laser illumination, layer thicknesses, refractive indices, and doping. Chapter 4 begins with introducing the simulation software and optimization methods, followed by material modeling and simulation considerations in both optical and electrical domains. Chapter 5 presents the modeling and simulation results. It also discusses the loss mechanisms and potential solutions for optimum operation. Chapter 6 discusses optical design considerations by reporting a tolerance study of thin PPCs to the incident wavelength and geometrical variations. Finally, chapter 7 wraps up this thesis with a summary of work completed, proposed applications of the results, and a discussion of future work.

Chapter 2

PHYSICS OF PPCS

PPCs are photovoltaic devices that are comprised of layers of semiconductor materials. Knowing the properties of semiconductor materials, the mechanism of the photovoltaic effect, and the terminologies associated with them can helps understanding their design and function.

2.1 Semiconductors

Semiconductors are a group of materials with conductivity characteristics between conductors and insulators. The most significant feature of semiconductor materials is that their conductivity can be altered by heat, alloying, illumination, electric field, and doping. As such, they can be engineered to obtain a desired conductivity under different conditions, making them highly suitable for electronic and photonic devices applications [59].

Semiconductors include groups of pure elemental and compound materials. Elemental semiconductors are composed of single species of atoms such as Si and Ge. Compound semiconductors are either binary or ternary and quaternary -alloy materials- where the properties of the semiconductor vary considerably by the percentage of each element. The material selection for compound semiconductors is based on compositions from the periodic table that yield the chemical bonding with an average of four valence electrons per atom [60]. Some examples of the materials from the semiconductor family are listed in Table.2.1.

2.1.1 Energy band structure

According to Bohr's model, a single atom has quantized energy levels, which means electrons

Table 2.1: Semiconductor materials

Elemental	IV-IV binary	III-V binary	II-VI binary	Ternary alloy	Quaternary alloy
Si	SiC	GaAs	CdS	AlGaAs	AlGaAsSb
Ge	SiGe	InP	ZnTe	InGaAs	AlInGaAs
As		AlAs	ZnO	InGaN	InGaAsP

can only occupy specific discrete energy levels. An electron in an atom can be described by four quantum numbers that substituting these numbers in the Schrödinger equation, describe the energy level of electrons. Based on the Pauli exclusion principle [61], two electrons cannot have the same combination of four quantum numbers. This means that more than two electrons (which have different spins) cannot have identical energy levels (Fig. 2.1.(a)). When two atoms covalently

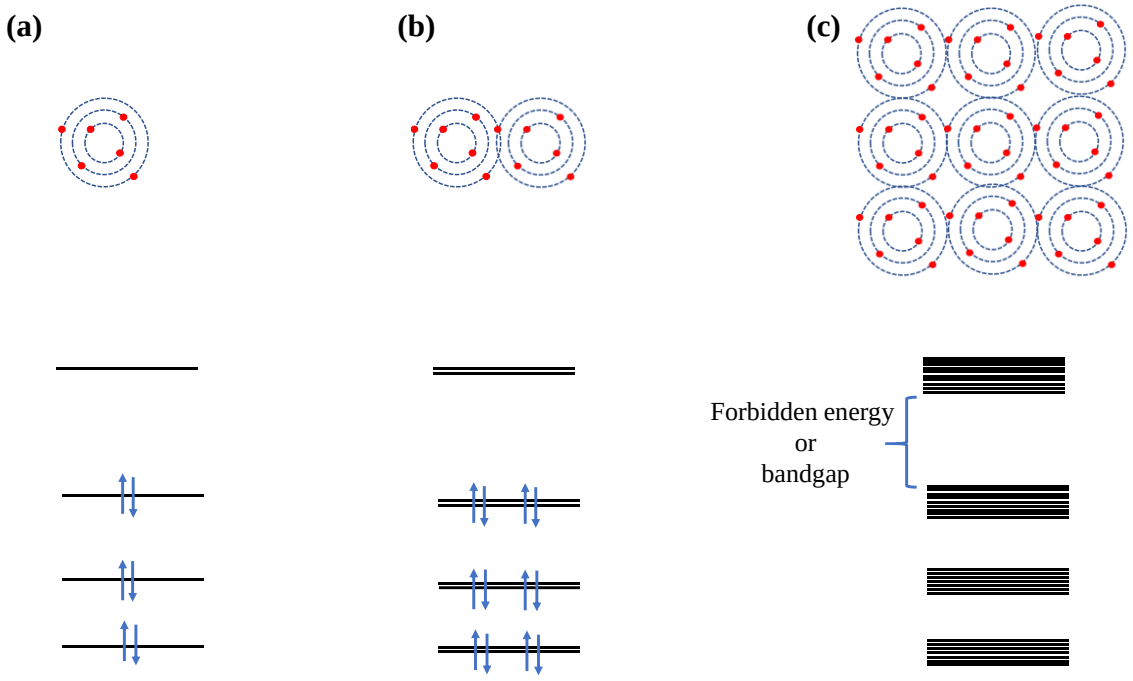

Figure 2.1: Atomic orbitals in (a) single atom (b) two atoms (c) N-atoms.

bond, they share electrons that occupy different but close energy states (Fig. 2.1 (b)). In solid crystals, N atoms are brought together and form extremely compact but still discrete energy levels that can be considered a continuum band energy (Fig. 2.1 (c)). Parts of the energy levels filled with electrons under stationary conditions are called the valence band, and those not occupied by electrons are referred to as the conduction band. The region between the highest level of the valence band and the lowest level of the conduction band is defined as the forbidden energy gap or bandgap and the corresponding energy difference is called the bandgap energy (*E*g). Conductors, semiconductors, and insulators are distinguished by their bandgap. In conductors, the valence and conduction bands overlap, which means there is no bandgap. Contrary to conductors, insulators have a significant large bandgap (about 3 to 7 eV) [62]. In semiconductors, the bandgap is small enough (<3.5 eV) that electrons can lift from the valence band to the conduction band by gaining energy via heat, light, or applied voltage.

Eq. 2.1 describes the general form of one-dimensional time-independent Schrödinger wavefunction:

$$\psi(x) = U_{+}e^{+jkx} + U_{-}e^{-jkx} \tag{2.1}$$

where U_{+} and U_{-} are solution constants, k is the wavenumber. Using this equation one can calculate the energy of the bands of a one-dimensional lattice that can be illustrated by energy-momentum (**E-k**) plots. In real three-dimensional lattices, the **k** vectors are presented in Brillouin zones. Fig. 2.2 (a) shows the first Brillouin zone of the face-centered cubic (FCC) lattice where the crystal cube is truncated by crystal planes in different directions. Fig. 2.2 (b) shows the corresponding **E-k** diagram for GaAs and AlAs. Semiconductor materials based on their band diagrams can be classified into direct and indirect bandgap types. In direct bandgap materials, the valence band's maximum aligns with the conduction band's minimum at **k**=0 or also called the Γ-

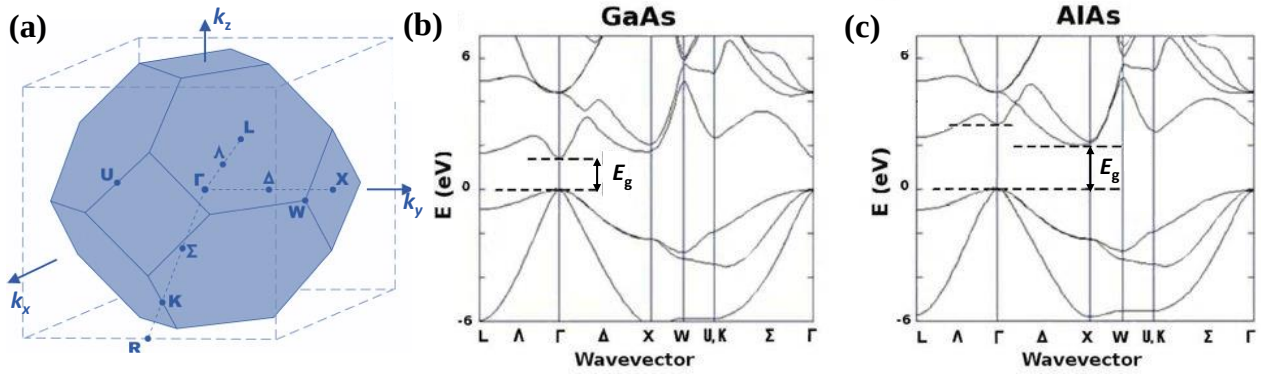

Figure 2.2: (a) First Brillouin zone for the material in FCC lattice. (b) GaAs and (c) AlAs electronic band diagrams. (Figure (a) and (b-c) adapted from [63] and [64] , respectively).

point. This is presented for GaAs in Fig. 2.2 (b). If the maximum of the valence band does not align with the minimum of the conduction band, the material has an indirect bandgap like AlAs (Fig. 2.2 (c)). In direct bandgap materials, electrons can hop from the valence band to the conduction band by gaining energy (for example by photon absorption). In contrast, in the indirect bandgap material, electrons require momentum (phonon absorption) in addition to energy to promote to the conduction band.

2.1.2 Lattice constant and crystal growth

Semiconductors can be classified as amorphous, polycrystalline, and crystalline, depending on their structure. In an amorphous form, there is no long-range order in the atoms' arrangement. In polycrystalline structure, atoms are formed in a periodic sequence in some regions while this periodic formation for crystalline structures are over the crystal lattice [65]. One of the parameters which plays a key role during the fabrication process of devices is their lattice constant. Lattice constants are dimensions of a unit cell in a crystal lattice (on the orders of angstrom) wherein cubic crystal structures, such as those for Si and GaAs, being equal in all three dimensions are referred to as '*a*'. PPCs are comprised of different layers of semiconductor materials with different bandgap energies. Lattice constant matching of these materials is critical for epitaxial growth. Epitaxy is a

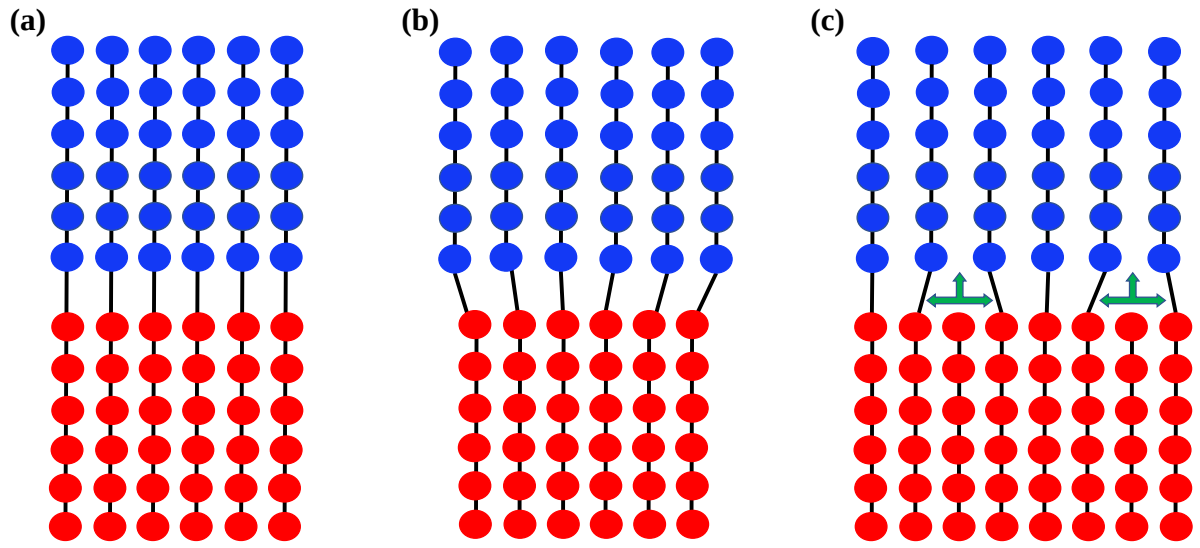

Figure 2.3: Schematics of interfaces between the substrate (red dots) and deposited material (blue dots) with different lattice misfits: (a) unstrained, (b) strained, (b) strained with dislocations.

deposition technique that grows a crystalline film on a substrate with matching crystallinity. This requires both deposited and substrate materials to be structurally compatible or, in other words, be lattice-matched to avoid strain build-up. The lattice constant difference, or misfit, f between two interfaces can be expressed using Eq. 2.2.

$$f = \frac{a_{substrate} - a_{layer}}{a_{substrate}} \tag{2.2}$$

Depending on f, the degree of strain is varied (Fig. 2.3). Typically lattice misfits greater than 2% result in dislocations (Fig. 2.3 (c)). Even high-quality strained layers with less than 1% misfit are stable up to a specific thickness. Beyond this critical thickness, strain relaxation occurs introducing defects and dislocations between the two interfaces. Due to lattice mismatch, these defects and dislocations degrade the device performance.

The optical properties used for the modeled PPCs in this work were measured experimentally for samples grown by molecular beam epitaxy (MBE). In MBE, under high to ultra-high vacuum conditions (10^{-8} to 10^{-11} torr), the source material is heated up to the level of evaporation.

Evaporated particles are beamed toward the crystalline substrate through a narrow opening to form the epi-layers. MBE results in slower throughput than other epitaxial growth techniques, but it enables a precise control of the layer thickness, doping concentration, and alloy composition, making it a powerful epitaxial growth tool for research applications [66].

2.1.3 Quaternary alloy

The deposition of material where a fraction of the constituent atoms are substituted with those of another species is known as alloying. An example is the alloy of AlAs and GaAs: replacing some of the gallium atoms in the crystal lattice with aluminum atoms creates the alloy $Al_xGa_{1-x}As$, where x is the mole fraction of aluminum. Alloying varies the bandgap, band structure, and hence electrical and optical properties of the resulting material. This allows us to create ternary and quaternary semiconductor compounds with desired properties for specific applications. The range of compositions of the general quaternary $Al_xGa_yIn_{1-x-y}As$ can produce lattice constants as large as that of InAs (x=y=0):6.0583Å or as small as that of GaAs (x+y≈1):5.6533 Å (see Fig 2.4). Compositions that correspond to lattice constants equal to the substrate layer, commonly InP, are the most popular ones [67].

Quaternary alloys of type $A_xB_yC_{1-x-y}D$ with three group III elements and one group V element, can be described as the weighted interpolation of ternary alloy constituents by Eq. 2.3. Note that P stands for parameter and 1-x-y was substituted by z for the sake of simplicity.

$$P(A_xB_yC_zD) = \frac{xyP(A_{1-u}B_uD) + yzP(B_{1-v}C_vD) + xzP(A_{1-w}C_wD)}{xy + yz + xz} \qquad (2.3)$$

where u, v and w are the mole fraction of each ternary alloy constituent and are defined as:

$$u = (1-x+y)/2 \qquad v = (1-y+z)/2 \qquad w = (1-x+z)/2$$

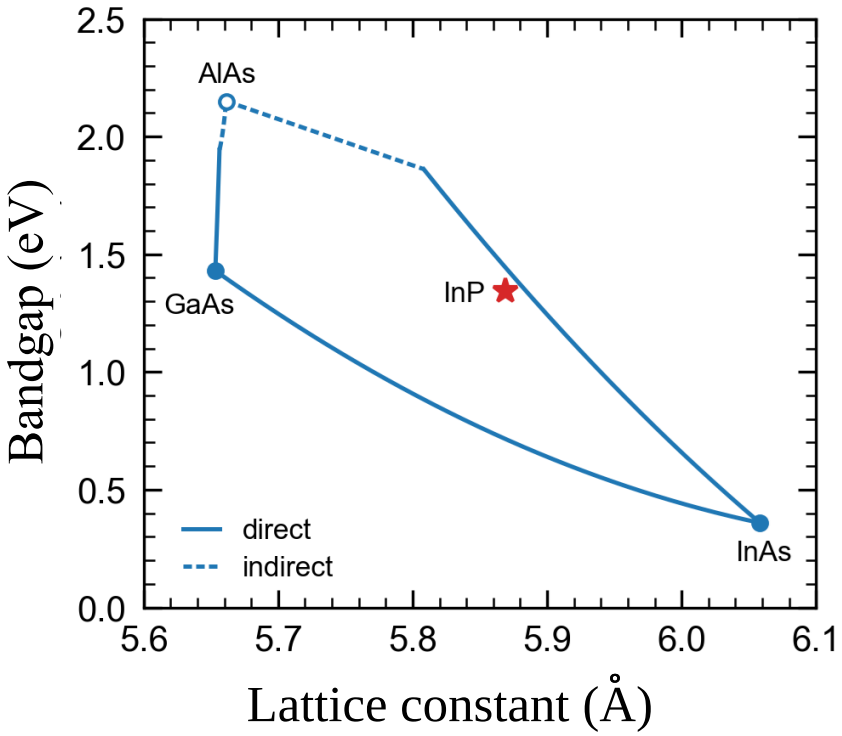

Figure 2.4: Bandgap versus lattice constant for binaries making up InAlGaAs. InP is indicated by red star.

2.1.4 Effective mass

The electron motion in a crystal with a periodic structure is different from electron motion in a vacuum. Electron motion within a crystal still obeys Newton's second law, but electron mass is replaced with its effective mass (m^*). Effective mass is a parameter that describes the transport of carriers (electrons and holes) under applied forces such as external electric field:

$$m^* = \hbar^2 \frac{\partial^2 E}{\partial k^2} \tag{2.4}$$

The effective mass depends on the concavity of the valence and conduction bands. Therefore, it has different values for electrons and holes in different semiconductors.

2.1.5 Carrier concentration

In intrinsic semiconductors, the number of electrons and holes are equal and are called intrinsic carrier numbers (n=p=n_i). In extrinsic semiconductors, the balance of electron and hole population within a semiconductor is disturbed by added p or n-type dopants. In extrinsic materials, changing the carriers' concentration alters the semiconductor properties. So, knowing carrier concentration in a semiconductor is essential to determine the semiconductor characteristics such as conductivity (or resistivity), current density, mobility and carrier generation, and recombination processes. One can obtain carrier concentration using the Fermi Dirac distribution function. This function gives the probability occupation of an electron state at a certain energy level at a temperature T:

$$f(E) = \frac{1}{1 + e^{(E-E_f)/k_B T}} \tag{2.5}$$

where k_B is the Boltzmann's constant and E_f is the Fermi level. The Fermi level represents the energy level where the state occupation probability is 50%. At absolute zero (T=0 K), the Fermi level positions in the middle of the bandgap (Fig. 2.5 (a)) in intrinsic semiconductors. In n and p

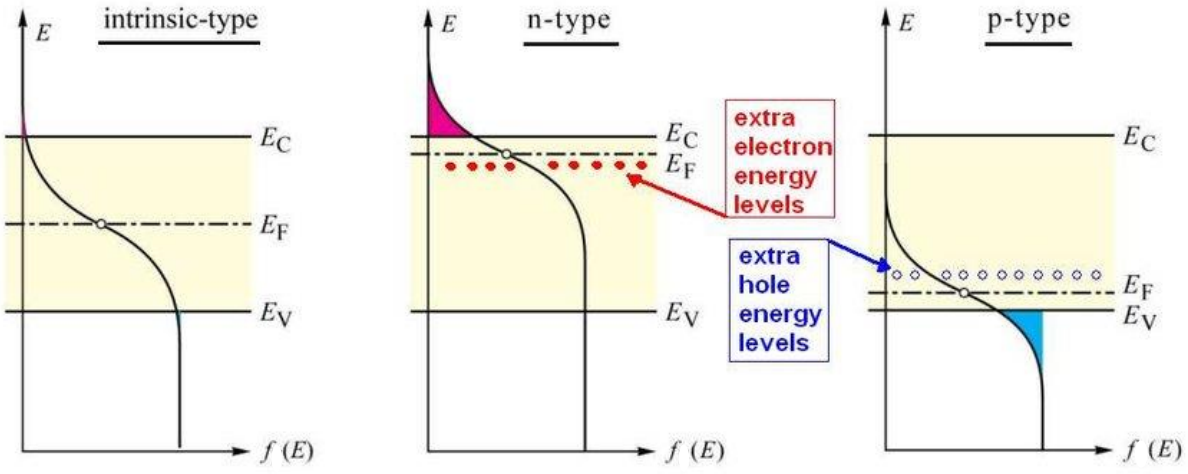

Figure 2.5: Carrier distribution function and Fermi level position in (a) intrinsic-type, (b) n-type and (c) p-type semiconductors. Adapted from [68].

type cases, it shifts towards E_c and E_v, respectively (Fig. 2.5 (b-c)). Fig. 2.5. illustrates the Fermi Dirac function and corresponding Fermi levels for intrinsic and extrinsic doped materials.

2.1.6 Generation, recombination, photon recycling

Generation

Electrons in the valence band can hop to the conduction band if they gain energy equal to or greater than the bandgap energy of the semiconductor. This energy can be absorbed in the form of light or heat. Moving an electron to the conduction band leaves a vacant position (hole) in the valence band. This process is called carrier or electron-hole pair generation; it enables excess carrier generation in the semiconductor and perturbs the equilibrium carrier concentration by:

$$n = n_0 + \Delta n \quad and \quad p = p_0 + \Delta p \qquad (2.5 \ \& \ 2.6)$$

where n_0 and p_0 are electrons and holes concentration in the equilibrium and Δn and Δp are excess electrons and holes. Fig. 2.6 shows two types of direct (band-to-band) and indirect (trap assisted) carrier generations.

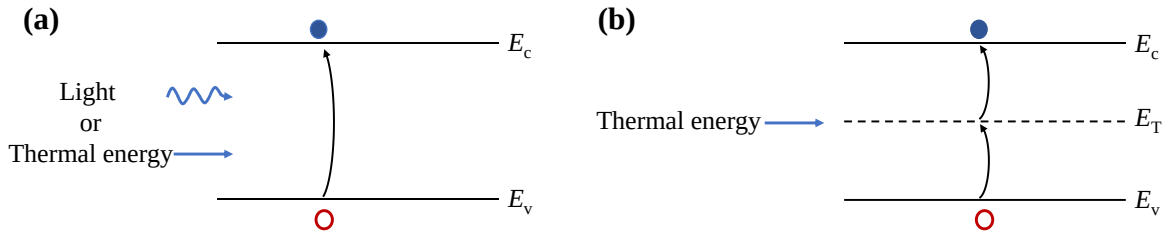

Figure 2.6: Different generation mechanisms: (a) band-to-band generation, (b) trap-assisted generation.

Recombination

The generated electron-hole (*e*-*h*) pairs can recombine and be destroyed through the recombination process. Depending on the semiconductor properties such as doping, defects, and being direct or indirect, several types of recombination can occur. In the following, we will discuss three main recombination mechanisms included in the simulations that were performed. The average time it

takes for generated excess carriers to recombine is defined as carrier lifetime or recombination lifetime (τ). The performance of photovoltaic cells strongly depends on this parameter.

Radiative recombination

Radiative recombination, is a process where electrons in the conduction band lose energy, move directly to the valence band, and recombine with holes. This recombination is illustrated in Fig. 2.7 (a). As shown in this figure, it is a direct and radiative process that leads to photon emission by releasing the excess energy of recombination.

Shockley-Read-Hall (SRH) recombination

Shockley-Read-Hall (SRH), also referred to as trap-assisted recombination, takes place through the trap energy levels (E_T), also known as recombination centers located across the bandgap region, which has been introduced due to lattice defects or atom impurities. A carrier is captured in a trap site, can be recombined with the opposite carrier already available in the trap site, or alternatively released through thermal activation and recombine in the valence or conduction band. The process is depicted in Fig. 2.7 (b). As shown in the figure, SRH recombination is an indirect and non-radiative mechanism. In this process, thermal energy is produced in the form of lattice vibration or phonon release.

Auger recombination

In Auger recombination, the band to band or trap assisted recombinations are accompanied with collisions with electrons. During this process, the recombination released energy transferred to the third carrier by collision and excites it to the higher energy state. Subsequently, the excited carrier relaxes back and releases energy in the form of lattice vibration (phonons). This process is known as thermalization. Fig. 2.7 (c) illustrates this mechanism; Auger recombination process involves

three particles and carrier concentration plays an important role in it. The higher the concentration rate, the higher collisions.

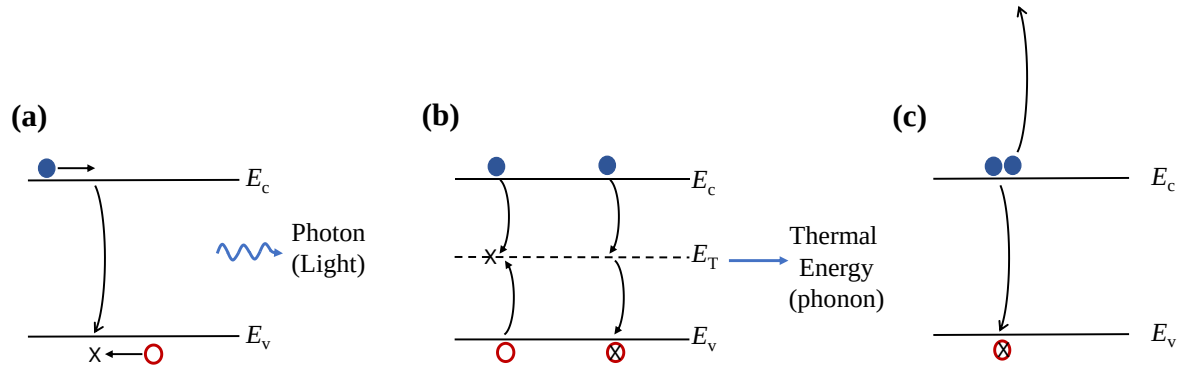

Figure 2.7: Different recombination mechanisms: (a) band-to-band or radiative recombination (b) Shockley-Read-Hall or Trap-assisted recombination (c) Auger recombination.

Surface recombination

Atoms in the surfaces and interfaces in general are prone to broken bonds. These dangling bonds introduce surface states in the bandgap that act as recombination traps. The surface recombination is specified by surface recombination velocity (S) in cm/sec and is strongly related to the surface trap density (N_s) in 1/cm^2 by

$$S = v_{th}\sigma N_s \tag{2.7}$$

where v_{th} is the thermal velocity in cm/sec and σ is the capture cross-section in cm^2.

Photon recycling

Some of the generated photons during radiative recombination exit the device and radiate into free space. The remaining photons are reabsorbed by the semiconductor itself and generate *e-h* pairs. This process is called photon recycling and leads to a beneficial impact on device performance such as V_{oc} enhancement [69]. This process is more pronounced in materials where radiative recombination is dominant and could be amplified by using BRs to cause internal reflection and

avoid photons exiting the active layer. This results in the reduction of radiative recombination and increases the photon density.

2.1.7 p-n junctions

p-n junctions are the heart of optoelectrical devices, including photovoltaic cells. When p- and n-doped semiconductors are joined together, carrier concentration difference in their interface results in diffusion current. Electrons (holes) in the n-side (p-side) diffuse toward the p-side (n-side) leaving positive (negative) ions behind. The oppositely charged ions near the junction create an internal electric field that acts as a barrier and opposes further carrier diffusion. This field forces electrons and holes to move (drift current) in the opposite direction to the diffusion current. The electric potential associated with this internal electric field is known as built-in potential (V_{bi}) and is related to the doping concentrations by:

$$V_{\mathrm{bi}} = \frac{k_{\mathrm{B}}T}{q} \ln\left(\frac{N_{\mathrm{A}}N_{\mathrm{D}}}{n_{\mathrm{i}}^2}\right) \tag{2.8}$$

where k_{B} is the Boltzmann's constant, T is absolute temperature (298 K), q is the elementary charge, N_{A} and N_{D} are the carrier concentration in p- and n-doped semiconductors, respectively [70].

The volume within the junction that is depleted from free carriers is defined as the depletion region and its width (w) at V=0 is given by:

$$w = \sqrt{\frac{2\varepsilon V_{bi}}{q}\left(\frac{N_A N_D}{N_A + N_D}\right)} \tag{2.9}$$

where ε is the dielectric permittivity of the semiconductor. The electrons and holes flow continue until they reach the equilibrium condition. In other words, equilibrium reaches when the minority

carriers flow due to the electric field and majority carriers flow due to diffusion cancels out each other.

Fig. 2.8. illustrates the energy band diagrams of p- and n-type semiconductors separately and in equilibrium after being brought together. E_F is constant and the E_c and E_v bend.

From this figure, the V_{bi} can be expressed as:

$$V_{bi} = q(\Phi_p - \Phi_n) \tag{2.9}$$

where Φ_n and Φ_p are the work function of electrons and holes, respectively. Work function is the minimum energy required for an electron to be removed from the surface of a solid to infinitely far away.

The V_{bi} and hence w can be manipulated by applying external voltage. By applying positive voltage V_F (forward bias) across the p-n junction, the potential voltage across the depletion region reduces to (V_{bi}-V_F). If negative voltage V_R (reverse bias) is applied, the voltage drop across the depletion region increases to (V_{bi}+V_R) [71].

2.2 Photovoltaics

Photovoltaic devices convert the optical power (light) to electric power (current and voltage) using the photovoltaic effect. Based on quantum theory, light is made up of packets of energy, so-called photons. When photovoltaic devices are illuminated by light whose photon energy (E_{ph}) is equal to or greater than their semiconductor material bandgap ($E_{ph}=h\upsilon \geq E_g$), electrons can elevate from E_v to E_c and leave behind holes, leading to *e-h* generation. In the next step, the light-generated carriers require to separate quickly (before recombination) and collect at contacts to contribute to the current generation. In the following, we will describe the photo-generated carrier separation

and collection mechanism in photovoltaic devices as well as terminologies associated with them in detail.

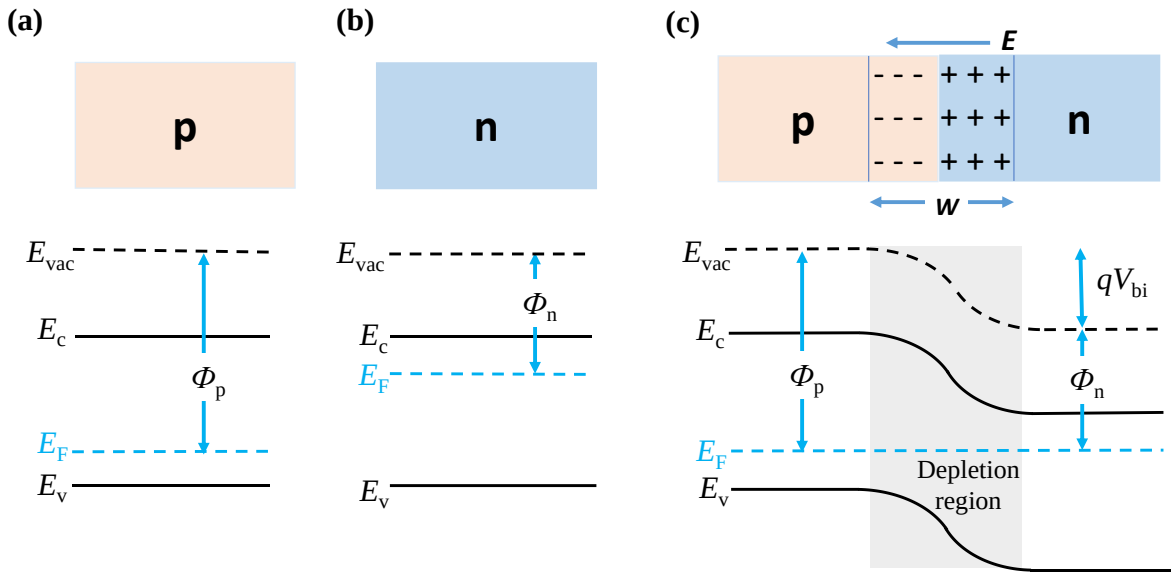

Figure 2.8: Energy-band diagram of (a) p-type (b) n-type (c) p-n junction in equilibrium.

The average length a carrier travels before recombination is called the diffusion length, $L_{p,n}$, and is related to the carrier lifetime $\tau_{p,n}$ by:

$$L_{p,n} = \sqrt{D\tau_{p,n}} \tag{2.11}$$

where D is the diffusion coefficient or diffusivity and equals to:

$$D = \frac{\mu k_B T}{q} \tag{2.12}$$

where μ is the carrier mobility.

The p-n junction plays an important role in the separation of light-generated carriers before they recombine and annihilate. Those carriers generated within depletion region are swept away by existing V_{bi} force in that region. (Fig. 2.9 (a)). If carrier generation takes place outside the depletion region, there is a high probability that only the minority carriers generated within the

minority carrier diffusion length of the depletion region (Fig. 2.9. (b)) will diffuse to the depletion region and be separated by the built-in electric field.

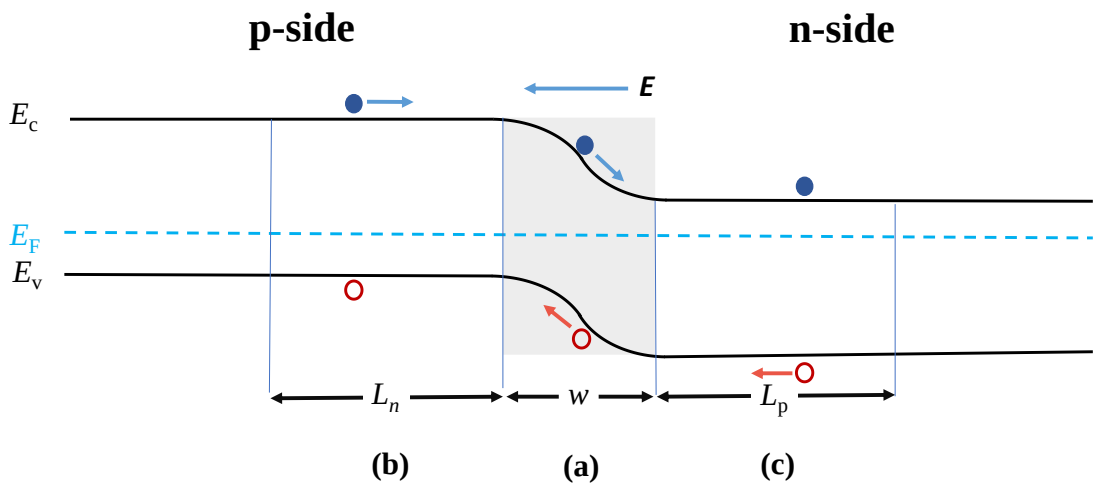

Figure 2.9: Light generated electron-hole pairs (a) within the depletion region (w) and (b-c) within the minority carrier diffusion lengths (L_n and L_p) at either side of the junction separated by the internal electric field (E).

From Fig. 2.9, the photocurrent is due to minority carriers and is in reverse bais (because electrons flow toward the cathode (n-side) and the holes flow to the anode (p-side)). Since it exists without any externally applied voltage, it is referred to as short circuit current density (J_{sc}), and its value is highly dependent on the intensity of the illuminated light. For convenience, same as other resources, we consider the positive sign for photocurrent from now on in this thesis.

In the dark, PV device behavior is basically like a diode, and the associated current density, known as J_{dark}, is given by an ideal diode equation:

$$J_{dark} = J_0 \left[\exp\left(\frac{qV}{k_B T}\right) - 1\right] \tag{2.13}$$

where J_0 is the dark saturation current. The total current in PV device is the sum of J_{dark} and J_{sc}:

$$J = J_{sc} - J_0 \left[\exp\left(\frac{qV}{k_B T}\right) - 1\right] \tag{2.14}$$

By applying forward bias, the dark current same as an ideal diode would start to increase, and at one point canceling out J_{sc} would lead to net-zero total currents. The voltage that corresponds to zero total currents, is referred to as open-circuit voltage (V_{oc}), and is equal to:

$$V_{oc} = \frac{k_B T}{q} ln\left(\frac{J_{sc}}{J_0} + 1\right) \tag{2.15}$$

J-V curve and key operating parameters of a typical PV cell are illustrated in Fig. 2.9. In the design of PV cells, giving the highest power to the loads entails PV cell operation at the maximum power point (P_m). The voltage and current corresponding to this point are denoted as V_m and J_m, respectively. The fill factor (*FF*) is given by:

$$FF = \frac{J_m V_m}{J_{sc} V_{oc}} \tag{2.16}$$

is a measure of the squareness of the *J-V* curve. (Shown as the square area in Fig. 2.10). *FF* describes how close or far the PV cell performance is compared to an ideal PV cell with the same J_{sc} and V_{oc}. The ratio of maximum output power to the input (incident light) power is defined as power conversion efficiency and calculated as:

$$PCE(\eta) = \frac{P_m}{P_i} = \frac{J_m V_m}{P_i} = FF \frac{J_{sc} V_{oc}}{P_{in}} \tag{2.17}$$

The importance of *FF* is more evident from this equation. Two PV cells with same J_{sc} and V_{oc}, but different *FF*, will have different efficiencies.

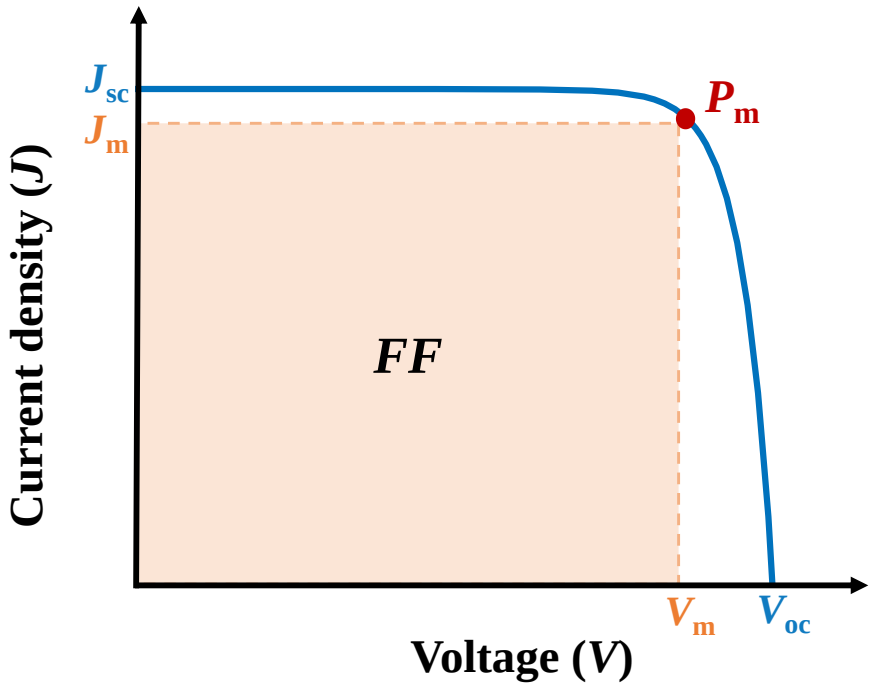

Figure 2.10: Current density-voltage (*J*-*V*) curve for a typical PV cell under illumination.

Chapter

3 DESIGN

The design of PPCs involves material and structure specifications for efficient photon absorption and carrier collection in order to reach the maximum efficiency. This chapter provides an explanation of material selection and describes the PPC structure with an integrated BR.

3.1 Material selection

In designing PPCs, the selection of the material for satisfying the target bandgap requirement is one of the main considerations. The material bandgap should lie below the target illumination photon energy. Minimizing the difference between the band edge and the incoming photon energy (0.946 eV, 1310 nm) reduces the thermalization loss, however, it also reduces the absorption coefficient. On the other hand, device layers should all be lattice-matched to the substrate (InP) to reduce the strain-induced defects that degrade cell performance by acting as recombination centers. We balanced the tradeoff between the thermalization losses and absorption coefficient while satisfying the lattice matching requirement by using the quaternary alloy $In_{0.532}Al_{0.097}Ga_{0.371}As$ with a bandgap of 0.88 eV for the absorber material [72] (Fig. 3.1). Assuming Beer-Lambert absorption using a measured absorption coefficient of 7424 cm^{-1} [72] this material requires about 5.3-µm thickness to absorb 98% of the incident light at 1310 nm (Fig .3.2). See PhD thesis of Meghan Beattie [20] for further discussion of the material selection.

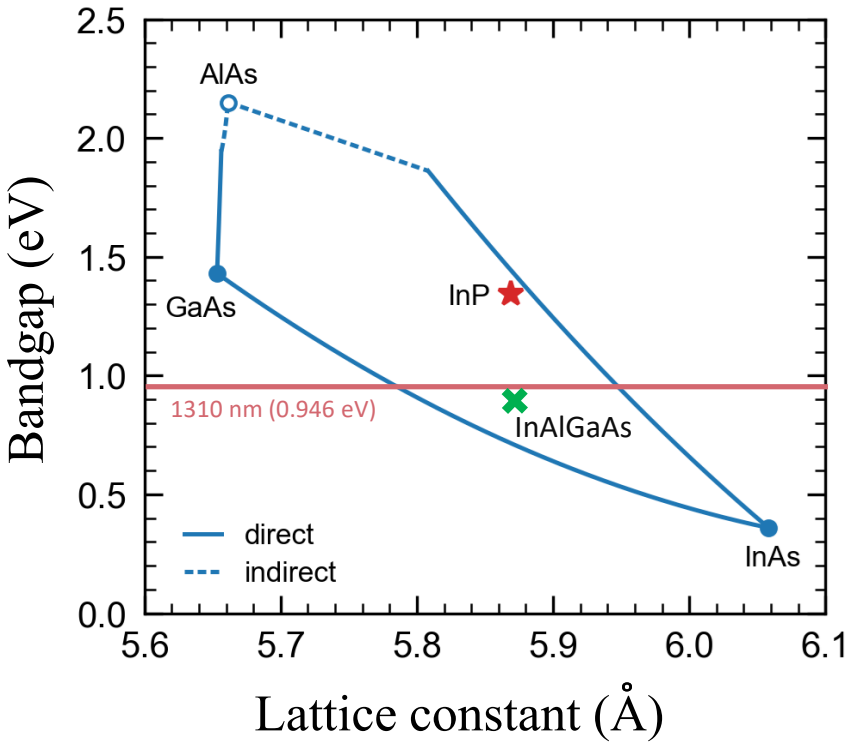

Figure 3.1: Bandgap versus lattice constant for binaries making up InAlGaAs. InAlGaAs with compositions that is InP lattice matched and satisfies bandgap requirements is indicated by green cross.

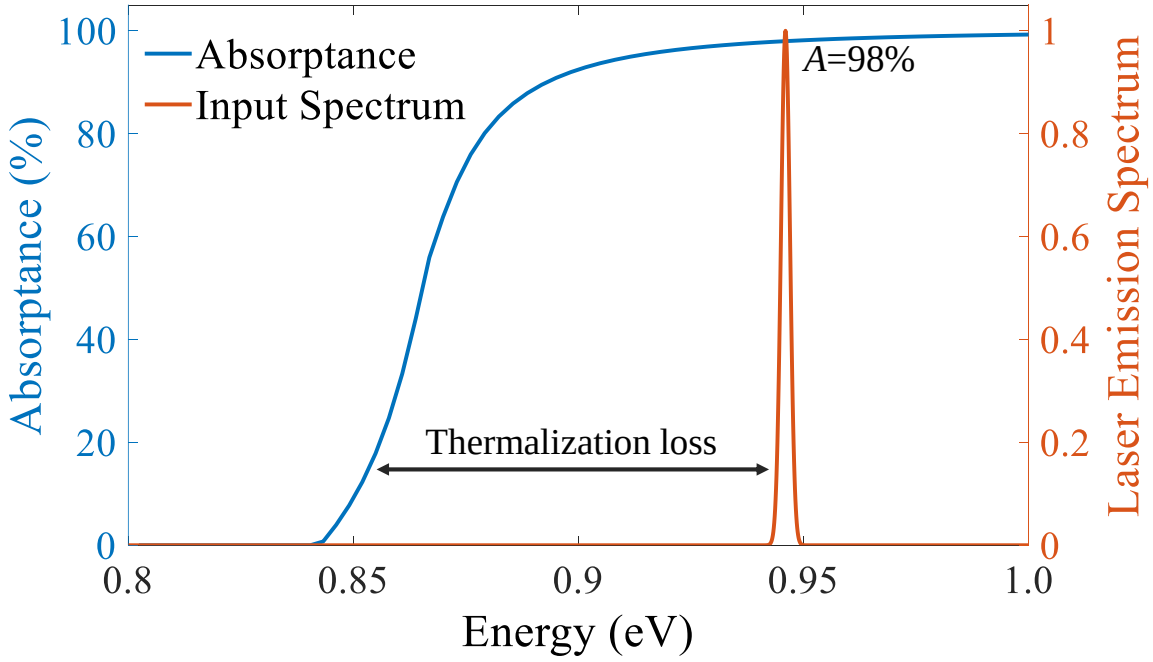

Fig 3.2: Device absorptance (blue lines) and normalized incident laser light (redline) versus photon energy. Based on Lambert's law, the 98% absorbance (*A*) of the incident light at 1310 nm wavelength, requires 5.27μm thickness of this material.

3.2 PPC structure

To achieve optimum operation and reduce the impact of surface recombination, transparent layers with high doping concentrations are deposited at the front and back side of the main absorber layer of a PV cell. These layers limit the reach of minority carriers to the surfaces and are referred to as front and back surface field (FSF and BSF) layers [73]. For longer wavelengths, absorption occurs at higher depths, closer to the back of cell. The interface between the heavily doped BSF and lightly doped base forms a field that acts as a low recombination velocity surface and improves the PV cell efficiency [63]. For our designs, the bulk region of the PPC (base) is selected to be p-type, as electrons, which acts as minority carriers, have longer lifetimes relative to holes in the intended $In_{0.532}Al_{0.097}Ga_{0.371}As$ quaternary.

The modeled PPCs consist of single pn junction absorber layers with bandgap of 0.88 eV, surrounded by wide bandgap, transparent FSF and BSF layers. Gold, which is highly reflective at the target wavelength, serves as both the back contact and the BR. The front contact grid is formed with help of two layers that are not included in the optical simulations: an InAlAs etch stop and an InGaAs cap layer [74]. Design parameters for modeled PPCs are listed in Table 3.1.

Table 3.1: Composition, bandgap, doping, complex refractive index @ 1310 nm, and thickness of epitaxial layers of modeled PPCs.

Layer	Material	Band Gap (eV)	Doping (x 10^{18} cm^{-3})	n_r	k	Thickness (nm)
Cap	n-$In_{0.526}Ga_{0.474}As$	0.74	5	3.64	0.22	100
Etch stop	n- $In_{0.3}Al_{0.7}As$	1.93	2	3.35	0	10
FSF	n- $In_{0.527}Al_{0.356}Ga_{0.117}As$	1.29	5	3.24	0	varied
Emitter	n- $In_{0.532}Al_{0.097}Ga_{0.371}As$	0.88	1	3.48	0.077	100
Base	p- $In_{0.532}Al_{0.097}Ga_{0.371}As$	0.88	0.02	3.48	0.077	varied
BSF	p- $In_{0.527}Al_{0.356}Ga_{0.117}As$	1.29	5	3.24	0	50

Minimizing reflection losses and increasing the optical path length are two critical requirements for high absorption. For monochromatic PPCs, it can be satisfied by aligning BR-induced resonances at the wavelength of interest. While this thesis focuses on numerical simulation, BR integration could be realized, for example, by inverted epitaxial growth on the InP substrate. Following epitaxy, the BR could be deposited by blanket metallization or periodic nano-texturing via nanoimprinting (see [75], for example) on the BSF layer (Fig 3.3 (a)). The sample would then be bonded to a mechanical handle, and the InP substrate would be removed through

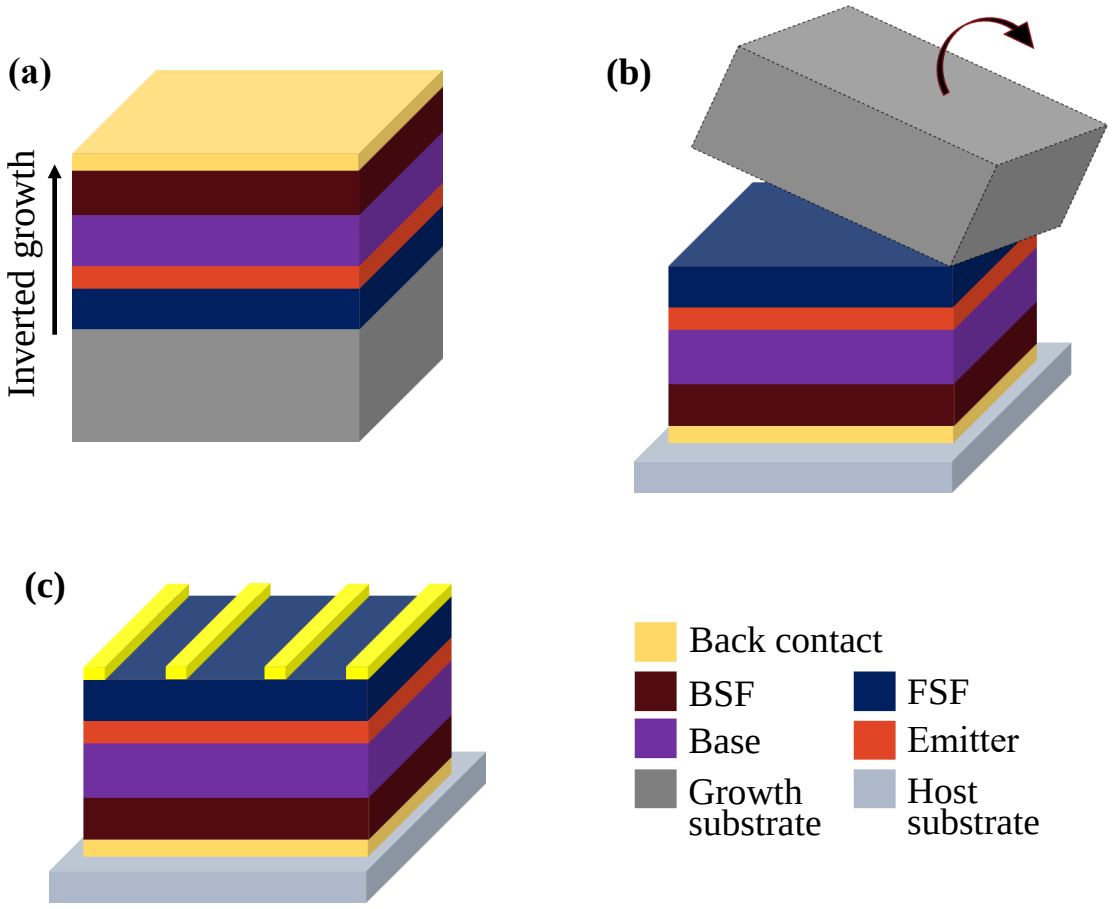

Figure 3.3: Fabrication process of light trapping with back reflector: (a) inverted epitaxial growth, (b) bonding to host substrate and removal of growth substrate, (c) top grid fabrication.

chemical etching or epitaxial liftoff. (Fig 3.3 (b)), and finally the metal would be deposited on top of the device to act as ohmic contacts (Fig 3.3 (c)).

Fig. 3.4 illustrates the epitaxial structure and BR designs proposed to enable ultra- thin PPCs using flat, cubic and pyramidal textures in this thesis. For PPCs with integrated BRs, the first design consideration is to tune the BR induced resonance peak in the absorptance spectrum (or resonance dip in the reflectance spectrum) to coincide with the target wavelength. Variations in the refractive index and geometrical parameters result in a resonance shift due to interference effects. In this study, modeled PPCs are optimized to enable the highest absorption with target operation centered at 1310 nm wavelength by varying the base and FSF layers thickness and geometry of nanotexture BRs including height *h*, width *w*, and spacing *s* for the cubic BR (Fig. 3.4 (b)), and height *h* and base width *w* for the pyramidal BR (Fig. 3.4 (c)). Emitter and BSF layer thickness and material compositions are kept fixed. Optimization space parameters are depicted in Fig. 3.4. The nanostructures were designed to be symmetric in the *x* and *y* dimensions to avoid polarization dependence. I also simulated conventional optically thick PPCs on InP substrates to use as a baseline to compare the light harvesting capability and power conversion efficiencies of ultra-thin PPCs. Should these designs be fabricated, they would employ a standard upright layer growth sequence and use a 100 nm buffer layer above the substrate with the same composition as the BSF to establish high-quality epitaxial growth.

Note that for all our models, texturing of the active layers was avoided; although it has been shown to boost optical absorption, it also degrades electrical performance due to enhanced surface recombination [45], [75].

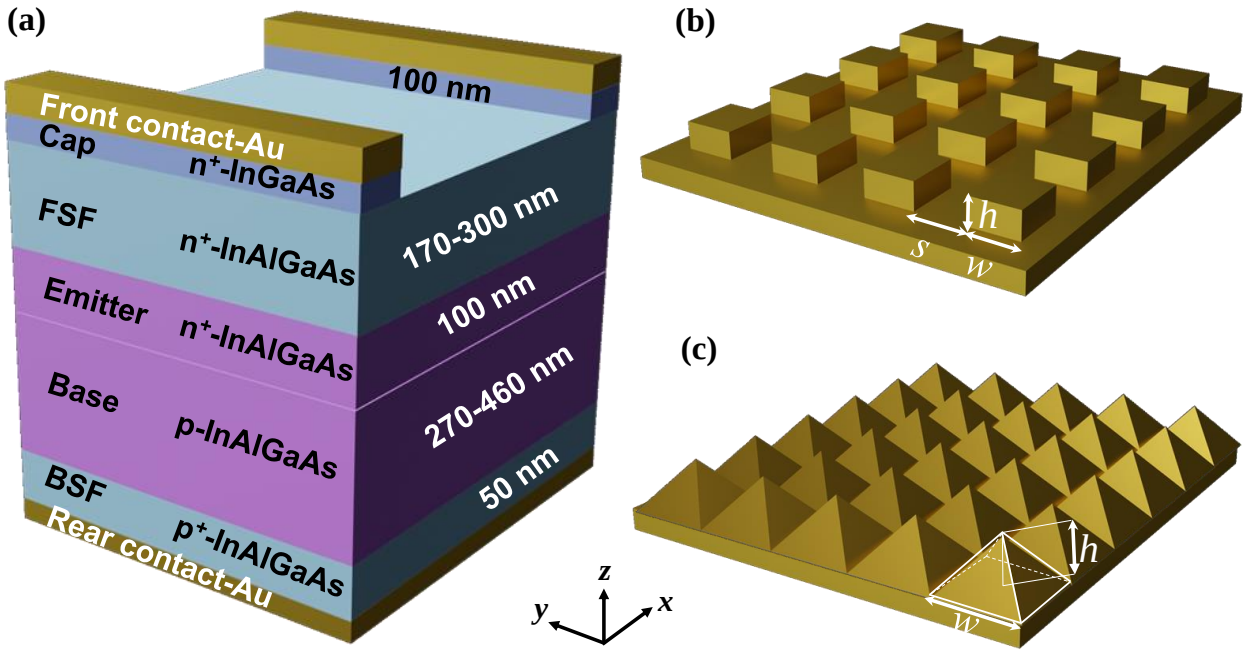

Figure 3.4: (a) Schematic structure of ultra-thin PPCs with flat back reflector. Layer thicknesses indicate the range over which each layer was optimized. Illustrations of (b) cubic back reflector with parameters for the height h, width w and spacing s indicated, and (c) pyramidal back reflector with height h and base width indicated.

Chapter

4 OPTOELECTRICAL SIMULATIONS

Photonic power converters (PPCs) are composed of semiconductor materials that use the photovoltaic effect to convert optical energy from a laser into electrical current. Modeling a PPC thus needs both optical and electrical simulations. The optical simulation calculates the optical energy absorbed by the semiconductor material. It models the generation of electron-hole pairs by assuming each photon incident on the device generates one electron-hole. The electrical simulation then determines how many of these photo-generated electron-hole pairs get collected at the electrical contacts and contribute to the output electrical power [76]. By combining these two simulations we can determine the photovoltaic efficiency of the PPC. Optical modeling of PPCs

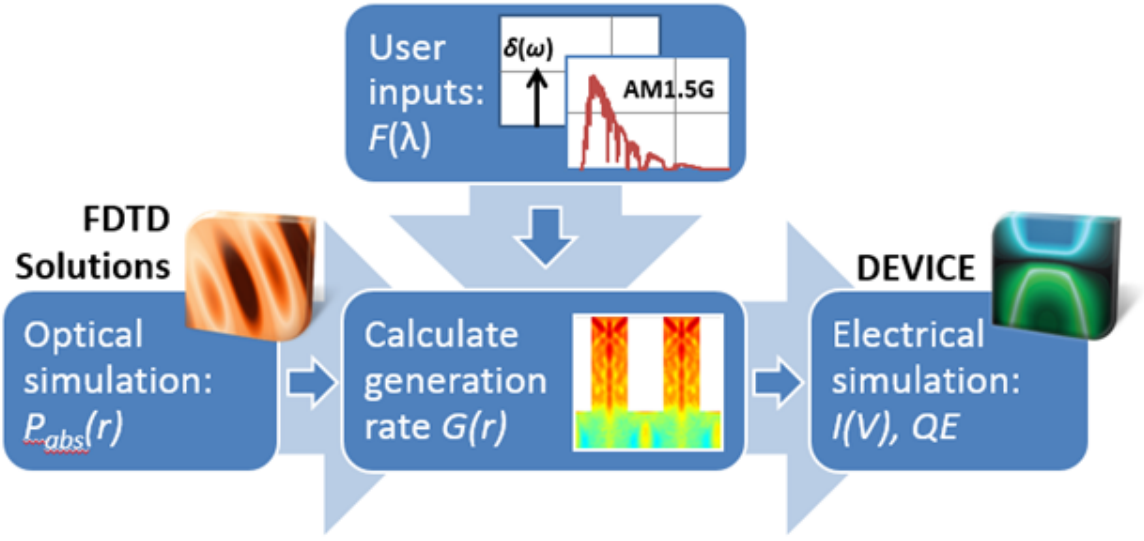

Figure 4.1: Lumerical opto-electrical simulation flow. Adapted from [77].

was performed using FDTD solution commercial software by Lumerical. This software uses the finite difference time domain (FDTD) method coupled with particle swarm optimization (PSO). Electrical simulations were conducted using DEVICE (Charge transport solver) by Lumerical, which employs finite element Poisson/drift-diffusion method [77]. This Chapter first provides an introduction to the above mentioned methods and then describes the opto-electrical simulation flow in further detail, as shown in Fig. 4.1.

4.1 Methods

4.1.1 FDTD method

Without a doubt, Maxwell's equations are one of the greatest achievements of the 19th century [78]. In the past, Maxwell's equations could only be solved for a single frequency, while nowadays they can be solved for a broad range of frequencies due to improved computational resources.

In 1966, Yee [79] introduced the direct time-domain method for solving Maxwell's curl equations, which is known as the FDTD method. This method has been further developed since then and has been applied in various fields of science and technology. The FDTD method is based on the approximation of derivatives of Maxwell's curl equations assuming non-magnetic materials.

$$\frac{\partial \vec{E}}{\partial t} = \frac{1}{\varepsilon_0 \varepsilon_r} \nabla \times \vec{H} \tag{4.1}$$

$$\frac{\partial \vec{H}}{\partial t} = -\frac{1}{\mu_0} \nabla \times \vec{E} \tag{4.2}$$

where $\vec{E}$ is the electric field, $\vec{H}$ is the magnetic field, ε_r is the relative permittivity, and ε_0 and μ_0 are the vacuum permittivity and permeability, respectively. In this method, the simulated structure

is divided into rectilinear grids and time steps are used for electromagnetic propagation calculations.

In order to understand the mathematics behind the FDTD method, we need to write Maxwell's equations in cartesian coordinates. For the sake of simplicity, we investigate only for one out of six field components:

$$-\frac{\mu_0 \partial H_x}{\partial t} = \frac{\partial E_z}{\partial y} - \frac{\partial E_y}{\partial z} \tag{4.3}$$

The integral form of this equation can be written as:

$$-\frac{\partial}{\partial t}\iint_{\Delta S} \mu_0 H_x dS = \oint_{\Delta l} E.dl \tag{4.4}$$

From Eq. 4.4 we can deduce that the curl of electric field is directly related to the time derivative of magnetic flux through a surface (ΔS) that is enclosed by a length Δl. The Yee cell can be fully described by writing all six sets of Maxwell's equations, which approximate each

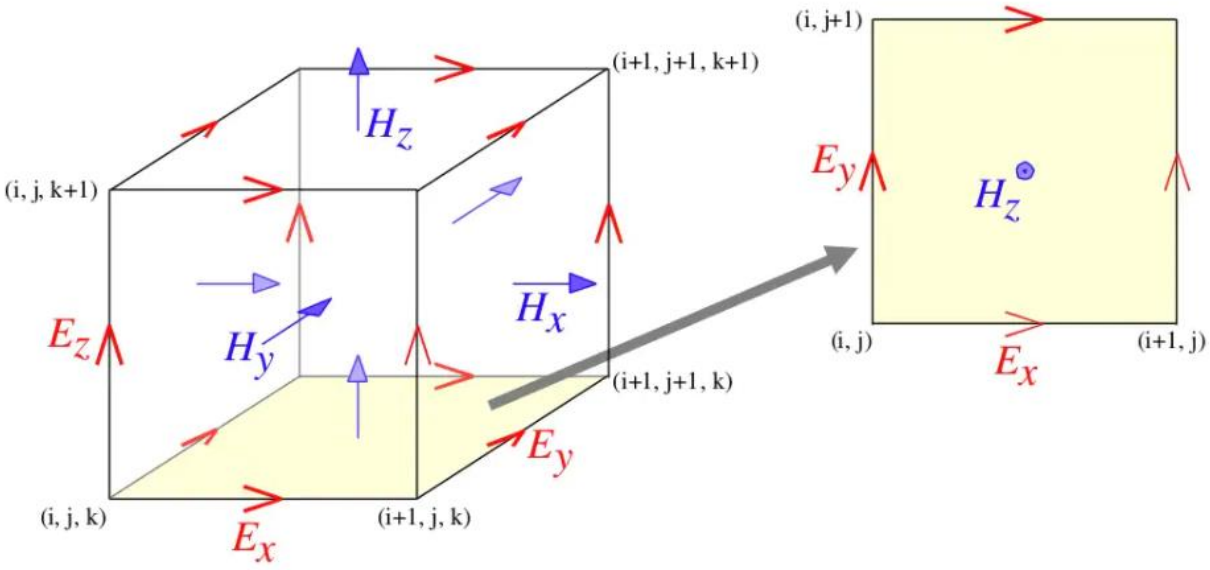

Figure 4.2: Fields on a grid in the Yee cell. Adapted from [80].

surface of the cell as shown in Fig. 4.2. Note that in the Yee cell, the electric and magnetic fields always are assigned to the edge and face center of cube, respectively [80], [81].

For finite-difference approximations of the derivatives, Yee applied central-difference expressions in four dimensions (three spatial and one time) that can be implemented into a program. Eq. 4.5, shows the central-difference expression for the time derivative:

$$\frac{\partial H(r,t)}{\partial t} \approx \frac{H\left(r, t+\frac{\Delta t}{2}\right) - H\left(r, t-\frac{\Delta t}{2}\right)}{\Delta t} \tag{4.5}$$

Using the central-difference formula twice we get:

$$\frac{\partial^2 H(r,t)}{\partial t^2} \approx \frac{\partial}{\partial t}\left[\frac{H\left(r, t+\frac{\Delta t}{2}\right) - H\left(r, t-\frac{\Delta t}{2}\right)}{\Delta t}\right]$$

$$\approx \frac{H(r,t+\Delta t) - 2H(r,t) + H(r,t-\Delta t)}{(\Delta t)^2} \tag{4.6}$$

FDTD is a mature method with a straightforward algorithm that is easy to implement with computer programs. Since FDTD is a time domain method, a wide range of frequencies calculations can be covered in a single simulation. With this method the optical properties of any 2D or 3D structures with complex geometries can be analyzed. It can be applied for different types of dielectrics, semiconductors, and metals with nonlinear and anisotropic properties. The main drawback of this method is that it is computationally expensive. Though finer grid sizes and smaller time steps add to the accuracy and reliability of simulations, they come at the cost of increased simulation times and memory requirements.

4.1.2 Drift-diffusion finite-element method

Electrical simulations were carried out using DEVICE, a charge transport simulator by Lumerical. This simulator uses finite element drift-diffusion method to investigate how many of the generated

electron-hole pairs collected at contacts and contributed to electrical current. To have a better understanding of the physics behind this method it is worth starting from the drift-diffusion equations:

$$J_n = qn\mu_n E + qD_n \nabla \mathrm{n} \tag{4.7}$$

$$J_p = qp\mu_p E - qD_p \nabla \mathrm{p} \tag{4.8}$$

where $J_{(n,p)}$ is the current density, q is the absolute value of the electron charge, n and p are the concentrations of the electrons and holes, $\mu_{(n,p)}$is the mobility, E is the electric field, $D_{n,p}$ is the diffusivity, and $\nabla \mathrm{n, p}$ is the carrier gradient.

The drift-diffusion equations have two terms. The first is the drift term, representing the current that is induced by an applied electric field. The second diffuse term represents the current that is introduced by the carrier density gradient. Solving this equation for electrical simulations requires that the electric field be known. The electric field can be obtained from Poisson's equation:

$$-\nabla.(\varepsilon \nabla \vartheta) = q\rho \tag{4.9}$$

where ε is the dielectric permittivity, ϑ is the electrostatic potential, and ρ is the total charge density. Lumerical solves the drift-diffusion and Poisson equations self-consistently on an unstructured finite element mesh (Fig. 4.3) to model carrier transport and currents inside the semiconductor device that originated from the applied electric field and carrier gradients.

The continuity equations are used to model the recombination and generation processes in the device:

$$\frac{\partial n}{\partial t} = \frac{1}{q}\nabla.J_n - R_n \tag{4.10}$$

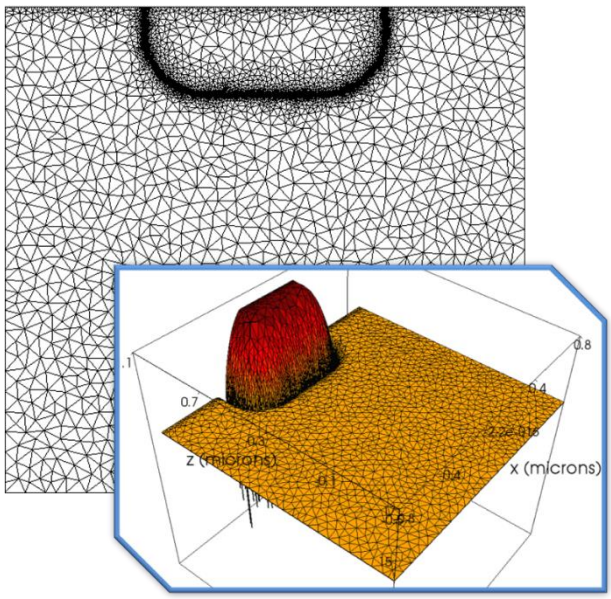

Figure 4.3: Unstructured, finite-element meshing used for charge transport solver in Lumerical. Adapted from [77].

$$\frac{\partial p}{\partial t} = -\frac{1}{q}\nabla . J_p - R_p \tag{4.11}$$

where $R_{n,p}$ are the recombination rate.

4.1.3 Particle swarm algorithm

When optimizing only one parameter, one may find optimal results by sweeping or manual variation of parameters. However, the optimization of multiple parameters is nontrivial. Optimization algorithms are powerful tools that can be used for these multidimensional optimizations. In this thesis, the PSO method has been used to optimize all parameters in the simulations simultaneously. The PSO method is a built-in tool in the Lumerical software. Here we describe this algorithm and its mathematics.

PSO was proposed for the first time in 1995 by Kennedy and Eberhart [82]. This method was developed from observation of the group behavior of birds and fish, where their collective movement is dependent on the individuals and communication between individual members of the

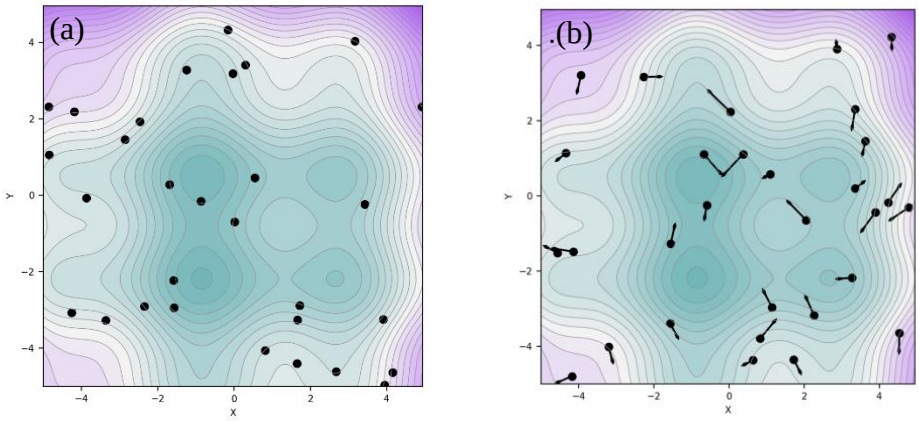

Figure 4.4: Particles randomly distributed in the solution space (a) particles position (b) particles position and velocity. Adapted from [83].

colony. In the PSO model, each parameter that requires optimization to achieve a global extreme is called a particle. Particles are distributed randomly in the solution space where they need to move to reach the optimum target (Fig. 4.4). In this method, each particle calculates a figure of merit of the optimization from its own position, which is described by either a number or a vector. All particles share this figure of merit with each particle in the group, and each particle compares their own (personal) information with the swarm (global) information. Both current and previous information is taken into account before each particle decides on a movement direction One stage of the algorithm is defined by a single movement of all particles. This process repeats several times, until the optimum result is obtained.[83]

The movement of particles in the solution space can be expressed using the following mathematical expression:

$$v_{t+1}^{i} = wv_{t}^{i} + c_1 r_1 \left(x_{pbest}^{i} - x_{t}^{i}\right) + c_2 r_2 (x_{gbest} - x_{t}^{i}) \tag{4.12}$$

where the new updated position of any particle is defined as:

$$x_{t+1}^{i} = x_{t}^{i} + v_{t+1}^{i} \tag{4.13}$$

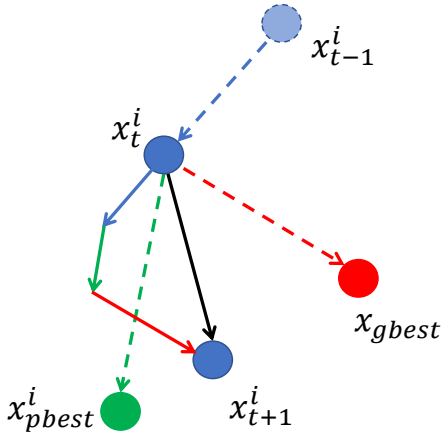

Figure 4.5: Iteration scheme of the particles. (Blue line: influence of the current velocity, green line: influence of particle memory, red line: influence of the swarm).

This expression consists of the set of parameters that influence the movement or velocity (v) of particles: (x_t^i), (v_t^i), (x_{pbest}) and (x_{gbest}) are the initial or current position of a particle, initial or current velocity of a particle, best position of an individual particle and best position ever achieved by swarm members as a group, respectively. The subscript index *p* is used to define personal, or individual particle terms, and *g* is used for group, or global, terms. In this equation the weight of the acceleration changes randomly at each iteration by inertial weight w, and by personal or global factors ($c_{1,2}$) and ($r_{1,2}$), where ($r_{1,2}$) is a random number between 0 and 1. Fig. 4.5 shows each term of this expression in the form of a vector, where w, $c_1 r_1$ and $c_2 r_2$ are considered coefficients with values less than 1 [84].

Fig. 4.6 gives a visual representation of how particles converge at a different number of iterations in this algorithm, for *t*=10, *t*=30 and *t*=90. The higher the number of iterations, the better the convergence and of course the higher the memory requirement. So, the number of iterations should be selected carefully to get optimum results.

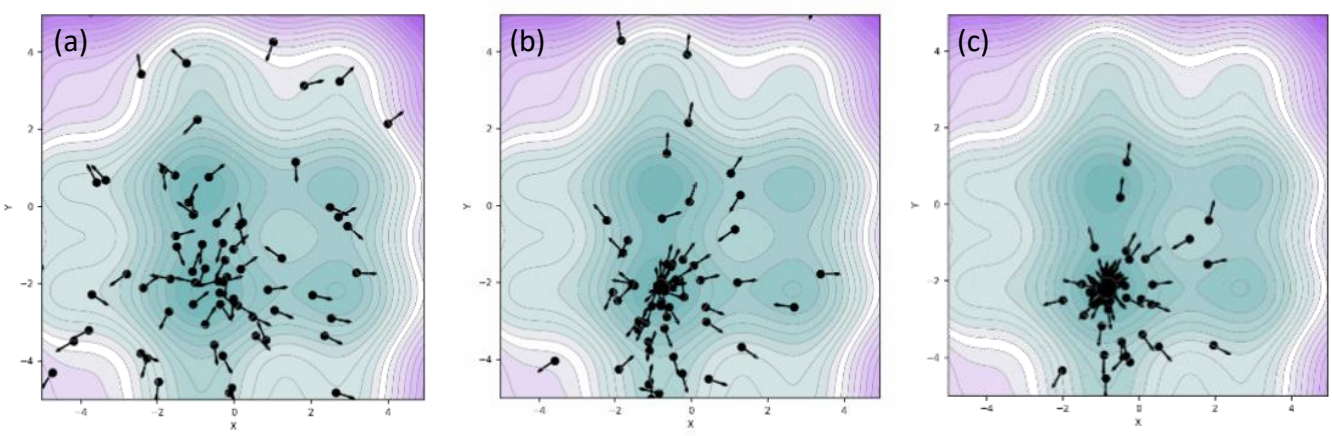

Figure 4.6: Effect of iteration count (t) on convergence (a) *t*=10, (b) *t*=30 and (c) *t*=90. Adapted from [83].

Fig. 4.7 shows the convergence at an iteration count of 33 for different inertial weights. In Lumerical, values of w and $c_{1,2}$ are set to default values that have demonstrated the best convergence for many test optimizations of photonic device modeling.

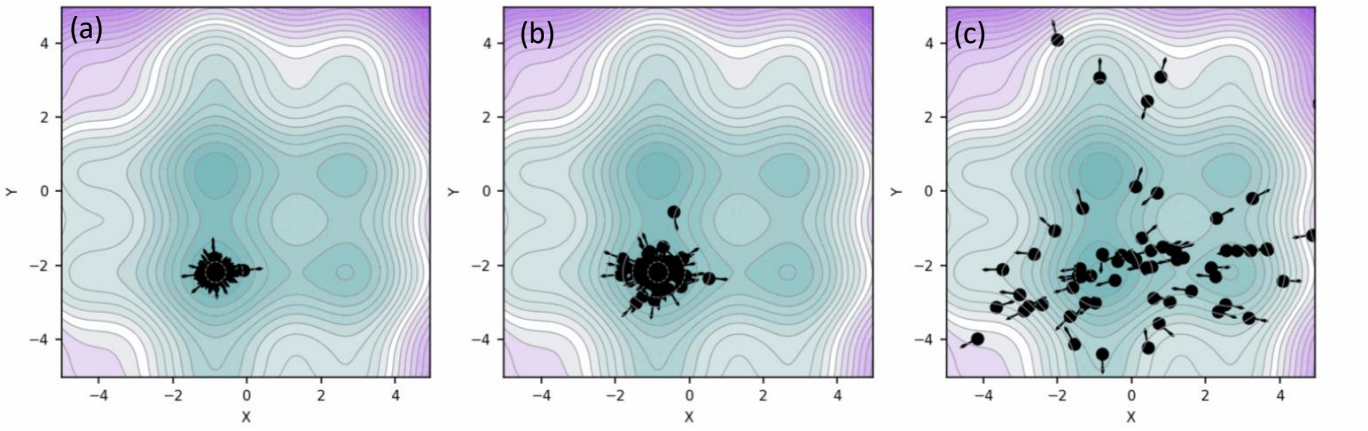

Figure 4.7: Effect of inertial weight (*w*) on convergence (a): *w*=0.1, (b) *w*=0.8 and (c) *w*=1, adapted from [83].

PSO is a straightforward and powerful method with a simple algorithm that can be easily implemented through computer programs. Compared to other intelligence algorithms such as the genetic algorithm or artificial bee colony, it converges faster and doesn't require differentiable optimization functions. The main drawback of this optimization method is for solving problems with more than one optimal set of parameters. In this case, there is a probability that PSO will

provide solutions for one of the local optimums rather than the global one [84]. Due to the large design space of optimization parameters in this thesis, a number of considerations were applied to be sure that optimizations result in global extrema and are reliable for comparison purposes. More details on this subject are discussed in the optimization section.

4.2 Opto-electrical simulations

4.2.1 Optical modeling

Optical simulations of PPC devices were performed in the Lumerical FDTD Solutions software using the FDTD method. The quaternary alloys were modeled with wavelength dependent refractive index parameters that were extracted experimentally by ellipsometry measurements of samples with the same composition grown by molecular beam epitaxy [35]. For data fitting in FDTD, the fit tolerance and max coefficients are set to 0.01 and 20, respectively. The real and imaginary wavelength dependent refractive indices (n_r, k) of the material data (red circles) and fitting in the FDTD model (blue line) are illustrated in Fig. 4.8. The optical properties of gold (back reflector) and InP (substrate) are taken from the Palik handbook [85].

The modeled structures were illuminated by a normally incident, x-polarized uniform light centered at 1310 nm with a linewidth of 10 nm, intensity of 100 mW/cm^2, and device temperature of 25°C. We performed 2D simulations for flat designs and 3D simulations for textured designs over a single unit cell. Periodic and perfectly matched layer (PML) boundary conditions were applied for the lateral (x and y) and growth (z) directions, respectively. For 3D simulations, since both the incident light and nanostructures were symmetric with respect to the center of the simulation region in x and y directions, symmetric and antisymmetric boundary conditions also were implemented to reduce computational requirements by reducing simulations to one-quarter of the original simulation. Figures 4.9 and 4.10 give an example of this reduction in the x direction.

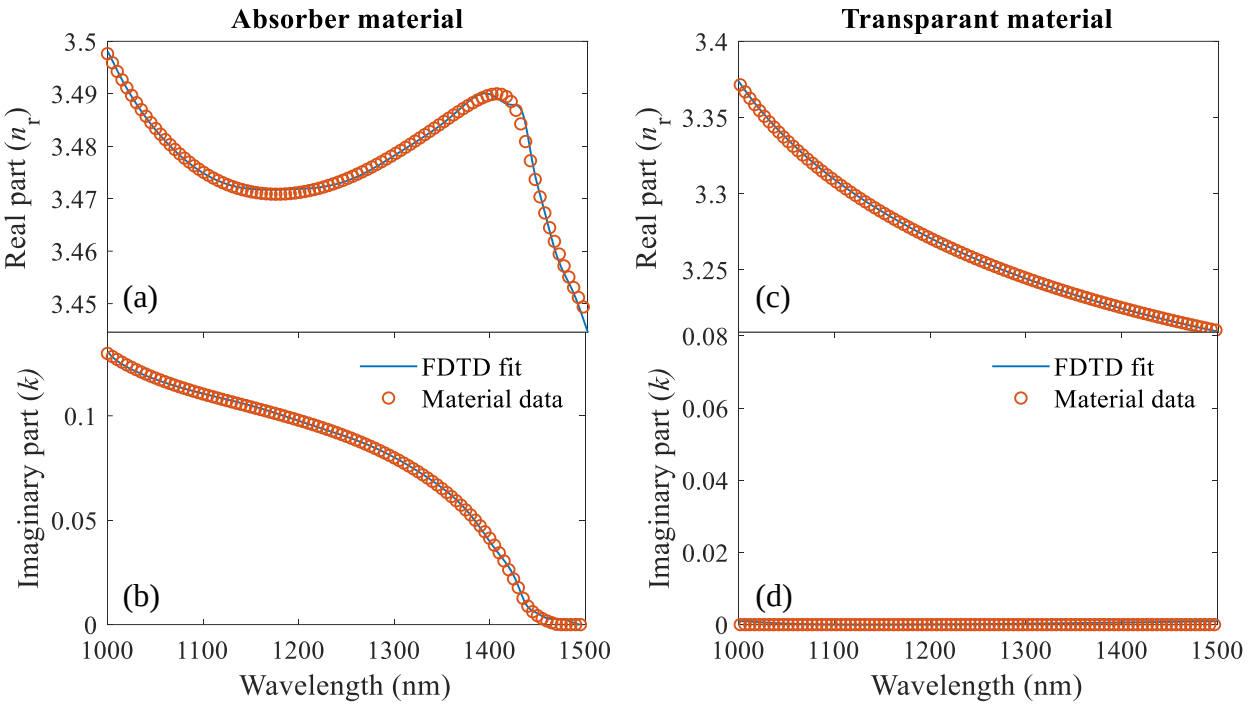

Figure 4.8: Real (nr) and imaginary (k) parts of the refractive index of quaternary alloys of absorber layer (a-b), transparent layer (c-d). Red circles are data that extracted from ellipsometry measurements and blue line is FDTD model fitting

Pyramids are modeled using a staircase approximation: replacing the pyramid by a series of stacked squares, each diminishing in size [86]. To avoid the design dependence on (*x* or *y*) polarized light, pyramid dimensions were kept equal in the *x* and *y* directions.

As explained in section 4.1, FDTD is a Yee cell (mesh pitch) based method. While selecting finer mesh sizes results in more accurate results, it also increases the simulation time and memory requirement due to solving larger number of Maxwell's equations. Therefore, it is essential to obtain a balance between simulation accuracy with an acceptable level of error and computational resources. To determine if the FDTD mesh is fine enough, convergence testing has been performed. In addition, for more accurate and precise numerical simulation results, finer override mesh regions were added to the thin layers and metal nanotextures. Fig. 4.9 shows an example of

an interface between the nanotexture and BSF layer with an automatic graded mesh that is not fine enough to simulate the metal nanotexture areas. The effect of using a fine override mesh is shown in Fig. 4.10, where it is visible that there are enough mesh lines to resolve each square in the staircase modeled pyramid.

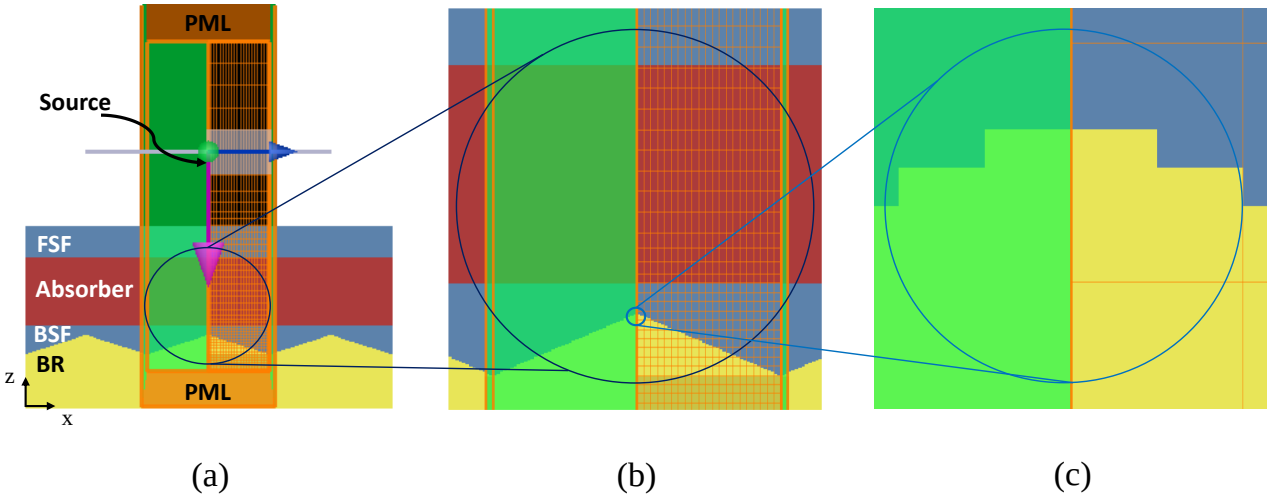

Figure 4.9: (a) Cross-section of a unit cell PPC with pyramidal nanotexture BR with automatic meshing. (b) Enlarged view of the circle area in (a), automatic mesh adjusts mesh refinement with finer meshing in the nanotextured area. (c) Enlarged view of the circle area in (b), the mesh size is not fine enough to distinguish each stack of staircase modeled pyramids. The green region indicates simulation area reduced to half in x direction, due to symmetric boundary conditions in *x*.

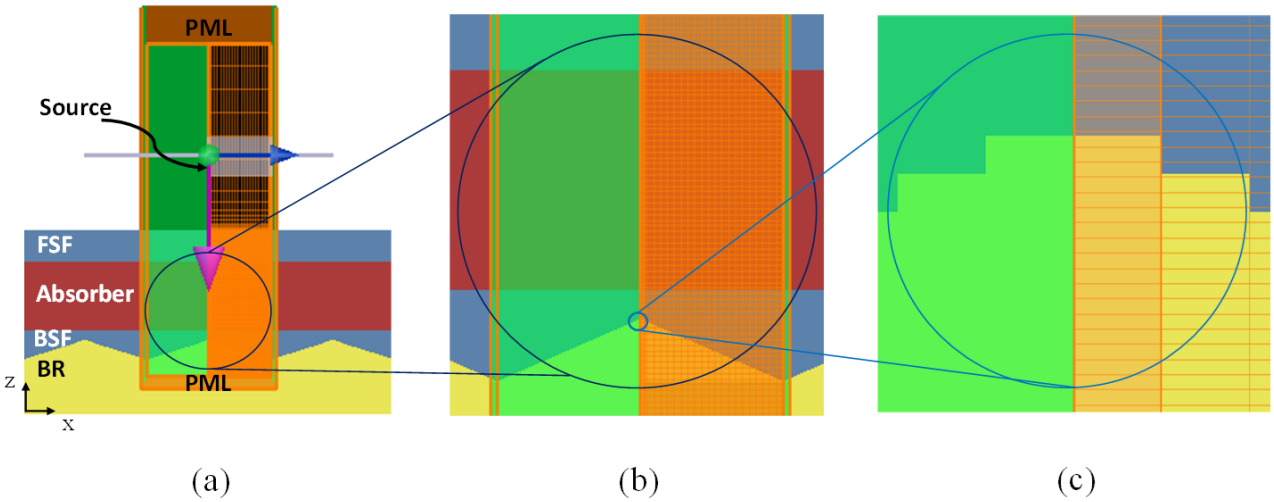

Figure 4.10: (a) Cross-section of a unit cell PPC with pyramidal nanotexture BR with override meshing. (b) Enlarged view of the circle area in (a). (c) Enlarged view of the circle area in (b), the mesh size is now fine enough to distinguish each stack of staircase modeled pyramids. The green region indicates simulation area reduced to half in x direction, due to symmetric boundary conditions in *x*.

Fig. 4.11 shows the convergence test results for absorptance as a function of the mesh size in the *z* direction. According to convergence test results, there are smaller changes in the absorptance when the mesh size is below 2 nm. For this work mesh size of 2 nm was selected. For a device with pyramidal nanotexture BR, a convergence test was performed to select the optimal thickness of the stacked squares for the staircase approximation. As shown in Fig. 4.12 the absorptance varies the least for squares smaller than 4 nm. We thus selected thickness of 2.5 nm which converges within ±0.3% for our simulations.

The PPC's generation rate *G* was calculated assuming that each absorbed photon generates an electron-hole pair. The total generation rate was calculated by integrating over the linewidth of the laser source as:

$$G(r) = \int P_{\text{abs}}(\lambda, r)\frac{\lambda}{hc}d\lambda \tag{4.14}$$

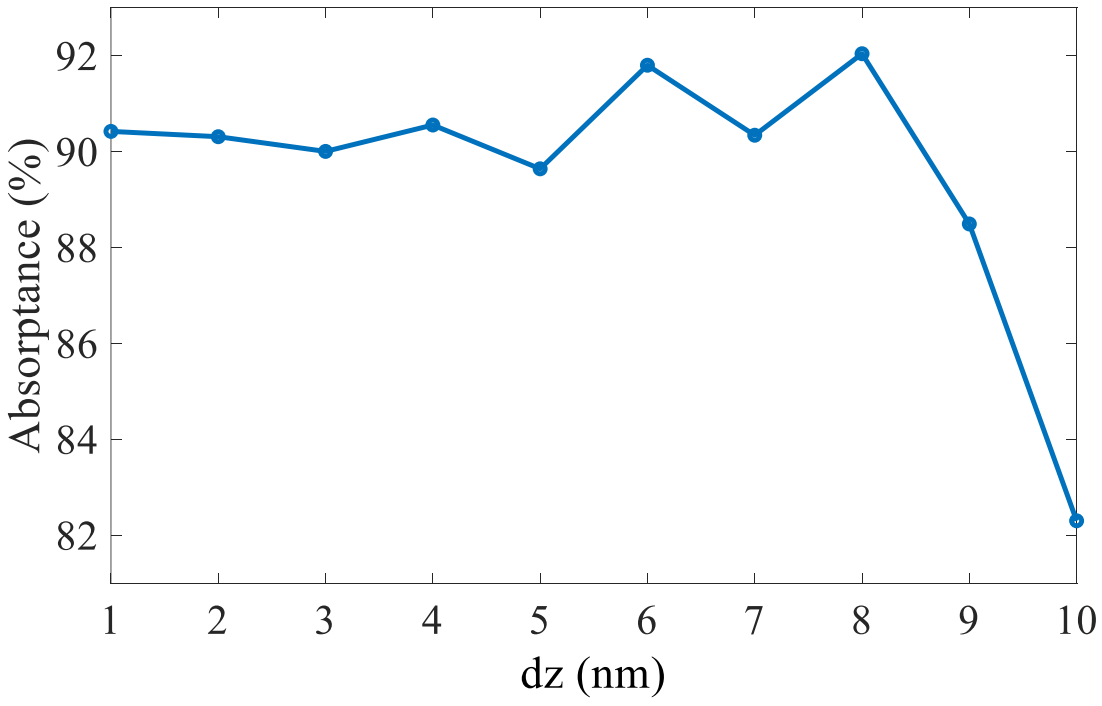

Figure 4.11: Convergence test results for absorptance versus mesh size in z direction.

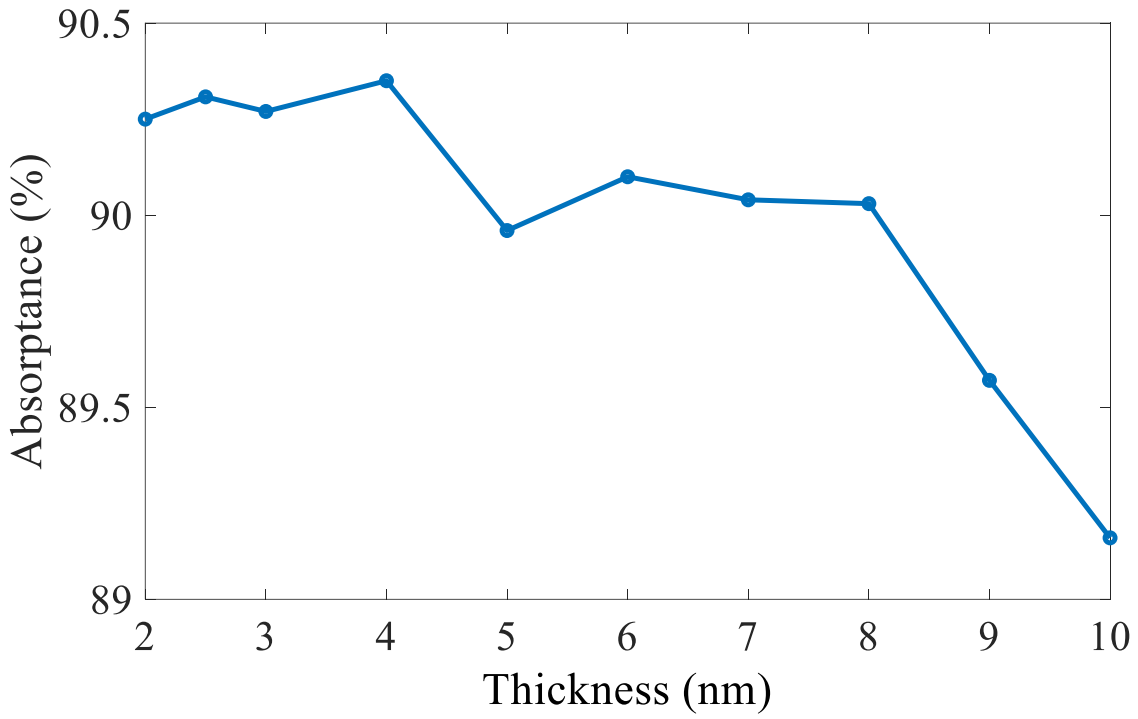

Figure 4.12: Convergence test results for absorptance versus thickness of the stacked squares in the staircase approximation of pyramidal nanotextures.

where P_{abs} is the absorbed power per volume per wavelength λ and position r, $\hbar$ is Planck's constant, and c is the speed of light in vacuum. The best case scenario is that all photoexcited carriers are collected at the contacts without any recombination loss and contribute to current generation, which defines the ideal photocurrent density as:

$$J_{\text{ph}} = q \int G(r)\ dr \tag{4.15}$$

where q is the elementary charge.

Since power absorption is a function of position and wavelength, it is proportional to the extinction coefficient and intensity of the applied electric field. For optical simulations field and permittivity data were extracted from a frequency domain power monitor and an index monitor, respectively. I used the analysis object tool from Lumerical for this purpose. This tool allows you to import raw data from the monitors and calculate the absorbed power and photocurrent density.

4.2.2. Electrical modeling

Electrical simulations were performed in CHARGE by Lumerical, at a device temperature of 300 K. The model included bulk recombination losses, radiative, SRH, and Auger; 5% gridline shading losses; and ideal ohmic contacts with no contact resistance. See Appendix for bulk recombination modeling in Lumerical.

The generation rate *G* obtained from the optical simulations was used as input for the electrical simulations. All material parameters for $In_xAl_yGa_{1-x-y}As$ excluding the SRH carrier lifetime and bandgap were determined by interpolation between the three ternary constituents: GaInAs, AlInAs, and AlGaAs [70], SRH carrier lifetime depends significantly on the material and growth quality and can vary from microseconds to picoseconds. For these simulations we selected 100 ns to represent a high-quality material. The bandgap is set to the experimentally determined value of 0.88 eV [20].

4.2.2.1 Interpolation

Interpolation of the quaternary material of the absorber and transparent layers were done using Eq. 2.3. For the absorber material with composition of $Al_{0.097}Ga_{0.371}In_{0.532}As$, we have:

A=Al B=Ga C=In D=As

x=0.097 *y*=0.371 *z*=0.532

u =0.637 *v* =0.5805 *w* =0.7175

Replacing *x*, *y*, *z*, *u*, *v*, and *w* for the absorber layer material:

$$P(Al_{0.097}Ga_{0.371}In_{0.532}As) =$$

$$\frac{0.0356(Al_{0.363}Ga_{0.637}As) + \mathbf{0.1973}(\boldsymbol{Ga_{0.4195}In_{0.5805}As}) + 0.0516(Al_{0.283}In_{0.717}As)}{0.285} \quad (4.16)$$

The bold term in Eq. 4.16 indicates the dominant constituent. The electrical properties of the ternary alloys and the results of their interpolation for $Al_{0.097}Ga_{0.371}In_{0.532}As$ using Eq. 4.16 are listed in Table.4.1. All parameters excluding those with references in Table 4.1 were obtained from Lumerical's built-in material library. Lumerical has variety of ternary alloys, and the parameters for a desired mole fraction can be determined as shown in Fig. 4.13.

The work function was the only parameter that was not available in the Lumerical material library. It was calculated using a linear interpolation for the given alloy mole fraction. For example, for $Al_xGa_{1-x}As$ we plotted the work function according to the mole fraction limits x= 0 and x=1, which corresponds to InAs and AlAs binaries with work functions of 4.83 and 4.97 eV, respectively. By plotting the work function as a function of Al mole fraction as shown in Fig. 4.14, the work function for desired mole fraction of Al (x=0.36) was found to be 4.88 eV

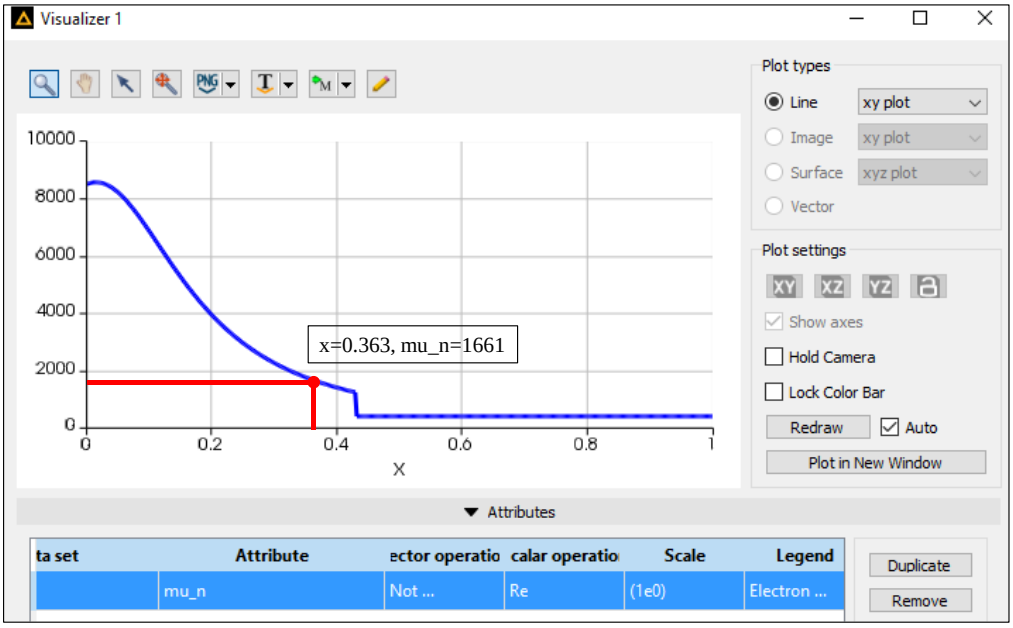

Figure 4.13: Defining electron mobility of ternary alloy of $Al_{0.36}Ga_{0.64}As$ for mole fraction of (x=0.36) using Lumerical material library.

Table 4.1: Electrical parameters of the absorber layer at T=300 K.

Parameter	Unit	Symbol	$Al_{0.36}Ga_{0.64}As$	$Ga_{0.42}In_{0.58}As$	$Al_{0.28}In_{0.72}As$	Interpolated $Al_{0.097}Ga_{0.371}In_{0.532}As$
Permittivity	$\varepsilon_s/\varepsilon_0$	E_{psr}	12.0747	13.768	13.1236	13.437
Effective mass	-	m^*_n	0.097 m_e[1]	0.0364 m_e	0.057 m_e	0.0478 m_e
		m^*_p	0.627 m_e	0.4447 m_e	0.51603 m_e	0.4806 m_e
Mobility	cm^2/Vs	μ_n	1661	14868	866	14806
		μ_p	167	492	175	340
Radiative recombination coefficient	cm^3/s	B	7.2e-10	3.14e-10	2e-11	3.1e-10
Auger recombination coefficient	cm^6/s	C_n	>0.7e-31 [89]	7e-29 [89] 8.1e-29 [90]	1e-30	4.9e-29
	cm^6/s	C_p	>6.1e-31 [89]	7e-29 [89] 8.1e-29 [90]	1e-30	4.9e-29
Work function	eV	Φ	4.88	4.99	5.07	4.99

[1] m_e is the rest mass of an electron (9.11×10^{-31} kg)

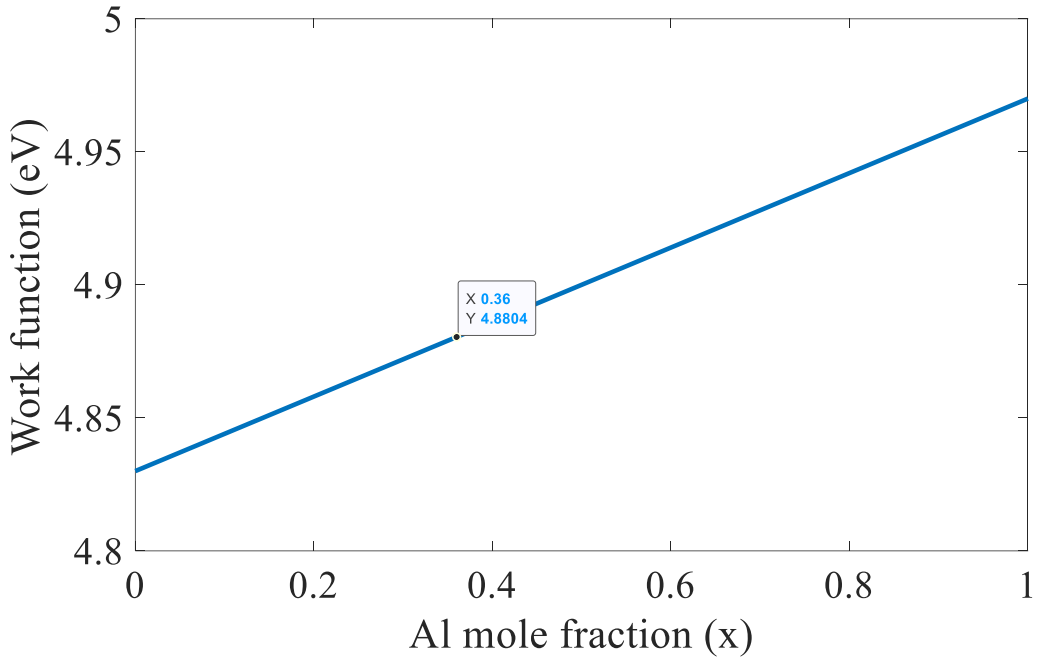

Figure 4.14: Determining the work function for desired mole fraction (x=0.36) of ternary alloy of $Al_xGa_{1-x}As$ using interpolation.

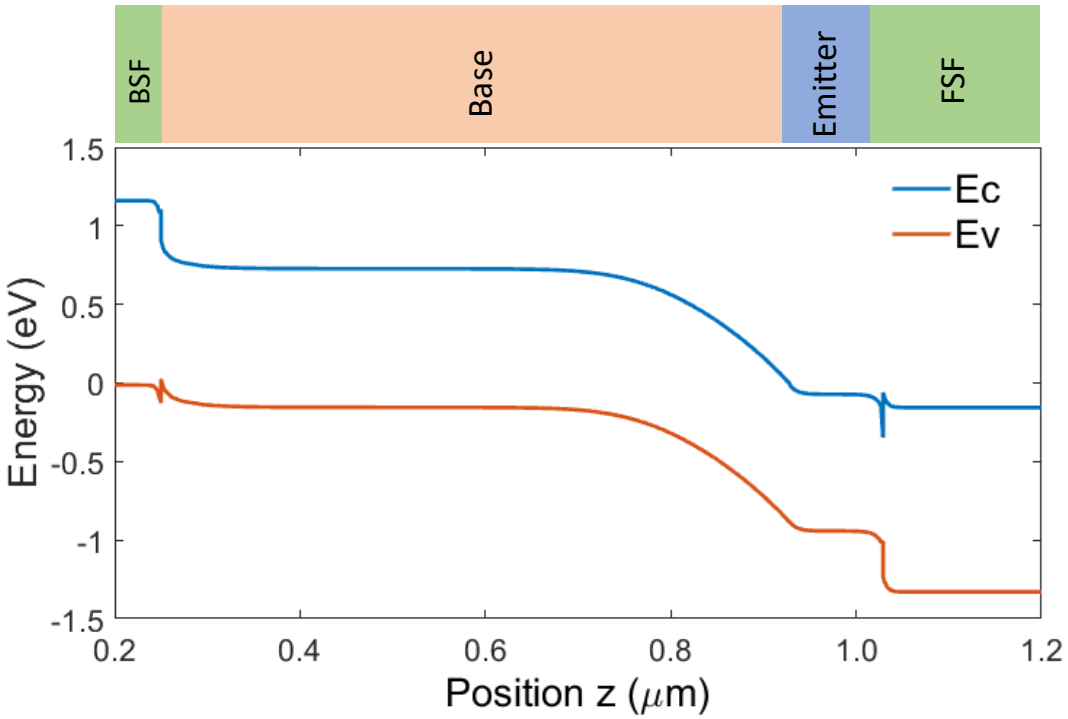

Figure 4.15: Band diagram of the structure comprised of layers shown in Table 4.1.

The device performance is evaluated in terms of current voltage behavior parameters such as PCE, J_{sc}, V_{oc}, and *FF*. Fig. 4.15 shows the band structure of the modeled PPC based on parameters shown in Table 4.1. The wider bandgaps of the FSF and BSF and offsets compared to those of the base and emitter block minority carrier movement and therefore suppress surface recombination losses.

4.2.3 Accuracy of the opto-electrical modeling

To demonstrate the accuracy of the simulation, I compared the model performance to a fabricated device with a 4100 nm absorber layer thickness, corresponding to 95% absorptance. Experimental measurements were performed by Dr. Meghan Beattie. As shown in Fig. 4.16, the model represents experimentally measured reflectance spectra very well. In order to fit the simulated *I-V* curve to the experimental measurements, a few adjustments in the material modeling were needed. Reducing the SRH electron and hole lifetimes to 1 and 0.1 ns, respectively, better matched the experimental J_{sc}, but there was still ~4mV mismatch between simulated and measured V_{oc}. In a heavily doped material, high impurity atoms can result in bandgap shrinking through creation of impurity bands [91]. To fix this ~4mV mismatch, bandgap narrowing effects were added to the simulations. The impact of bandgap narrowing was approximated in the simulations using Lumerical's built-in Slotboom model [92]:

$$\Delta E_G = -V_1 \left[ln\left(\frac{N_D^+ + N_A^-}{N_0}\right) + \sqrt{ln^2\left(\frac{N_D^+ + N_A^-}{N_0}\right) + C} \right] \tag{4.17}$$

where V_1, N_0 and C are fitting coefficients that were set to 0.0055, 4×10^{15} and 0.5, respectively, to reach the measured V_{oc}.

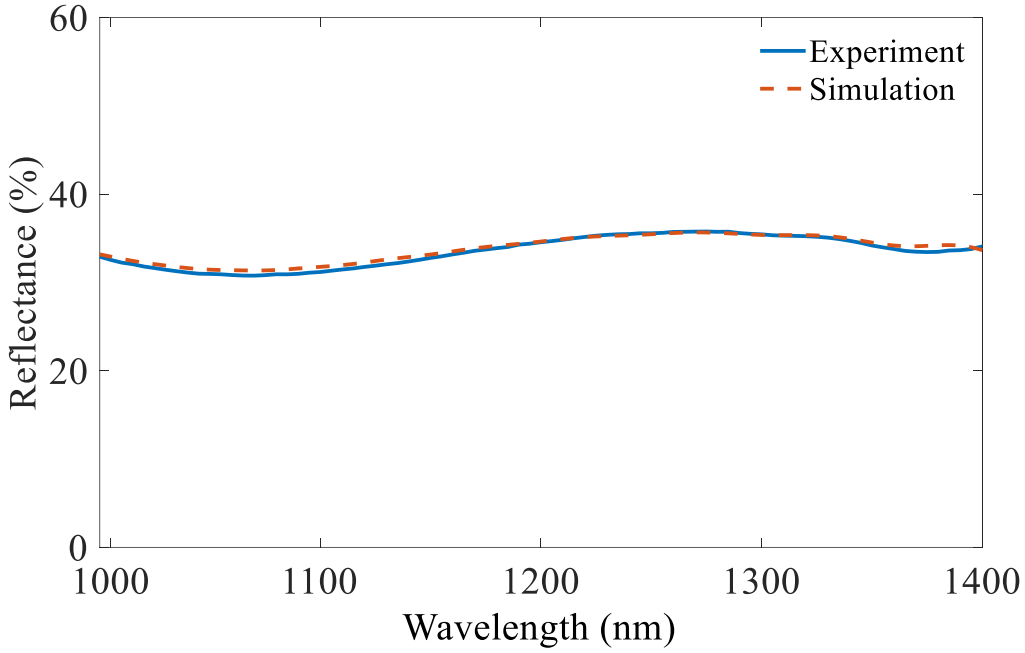

Figure 4.16: Experimentally measured and simulated reflectance spectra for a thick PPC with 4100 nm absorber layer thickness under 1310 nm illumination with intensity of 100 mW/cm^2 at T=300K.

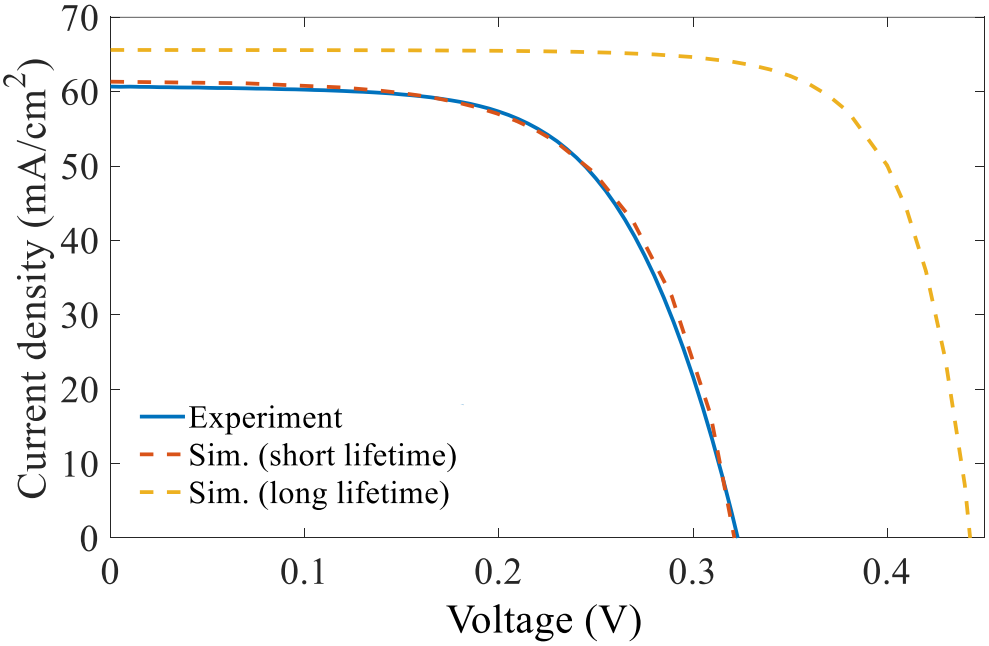

Figure 4.17: Experimentally measured and simulated I-V curve for a thick PPC with 4100 nm absorber layer thickness under 1310 nm illumination with intensity of 100 mW/cm^2 at T=300 K.

The lower efficiency of the fabricated device originates from 30% reflection loss, 8% grid line

shading, and shorter carrier lifetimes. To highlight the effect of material quality on the PPC's performance, simulations with longer SRH carrier lifetimes of 10 ns for both electron and holes were included in the simulations and are depicted in Fig. 4.17 using a yellow dashed line.

4.2.4 Computational time

One of the main considerations in simulations is to improve the accuracy of the modelling while minimizing the computational cost. Both optical and electrical simulations in this thesis are performed using one of the computational resources in SUNLAB with the properties that are listed in Table 4.2.

Table 4.2: Computation resource properties for opto-electrical simulations

CPU	Intel Xeon E5-2620 v3
Cores	6
Hyperthreads	12
RAM	32 GB
SSD	240 GB
HDD	1 TB+ 1TB
Graphics	AMD Radeon HD 5450

Simulation times varied depending on the dimension and bandwidth of simulations as well as thickness of the modeled structures.

The optical simulations for a 2D model took 7 and 20 minutes, corresponding to narrowband (1310±5 nm) and broadband (1000-1400 nm) simulations, respectively. For the optical 3D simulations that were carried out for the thin models, the narrowband and broadband simulations took 2 and 15 minutes, respectively.

The electrical simulations for the 2D structures took approximately 30 minutes, while 3D structures took approximately 2 hours. The number of voltage sweep points used to generate the *I-V* curves had a significant impact on the electrical simulation times.

The optimizations, which were highly dependent on the number of parameters in the design space and the simulation bandwidth, varied from 3 to 10 hours on average. Running 2D sweeps were the most time-consuming simulations, with 15 to 20 hours depending on the number of sweep steps. These 2D sweeps were used to create the absorptance maps that are presented in Chapter 6.

Chapter

5 RESULTS AND DISCUSSION

The opto-electrical simulation results for a thin and ultra-thin PPCs with three types of flat, nanotextured pyramidal and nanotextured cubic BRs are discussed in this chapter. Irradiant light intensity effect on designs performance and potential solutions for improvement of conversion efficiency improvement are also provided in this chapter.

5.1. Thin PPC with flat BR

I embarked simulations for a thin PPC by modeling a pre-existing sample in the lab with the same composition as my design. This sample had an absorber thickness of 842 nm and was grown with the purpose of current-matched bottom segment in a 2 junction PPC design. Due to strong Fabry-Perot resonances induced by the BR, the first design consideration was to tune the resonance peak in the absorption spectrum (or resonance dip in the reflection spectrum) to coincide with the target wavelength. Variations in refractive index and layer thicknesses result in a resonance shift due to interference effects. Since the material was already selected and could not be changed, by varying the thickness of the absorber (sum of base and emitter) and FSF layer, I tried to tune the resonance dip in the reflection spectra at 1310 nm. Table 5.1 lists a some of the selected combinations. As can be seen in this table different combination of FSF and absorber layer (designs C and D) align resonances at 1310 nm but with slightly different absorptance and reflectance losses. So,

employment of optimization tools was necessary to find the combination that satisfies both resonance alignment and absorptance maximization.

Table 5.1: Summary of the variations of the layers thickness to align the resonance in the reflectance spectrum at 1310 nm for a thin PPC with flat BR.

	Absorber thickness (nm)	FSF thickness (nm)	Resonance Wavelength (nm)	Absorptance (%) @ 1310 nm	Reflectance (%) @ 1310 nm
A	842	400	1190 1380	38	62
B	810	380	1325	95.2	0.04
C	775	400	1310	94.3	0.03
D	750	430	1310	94.8	0.007

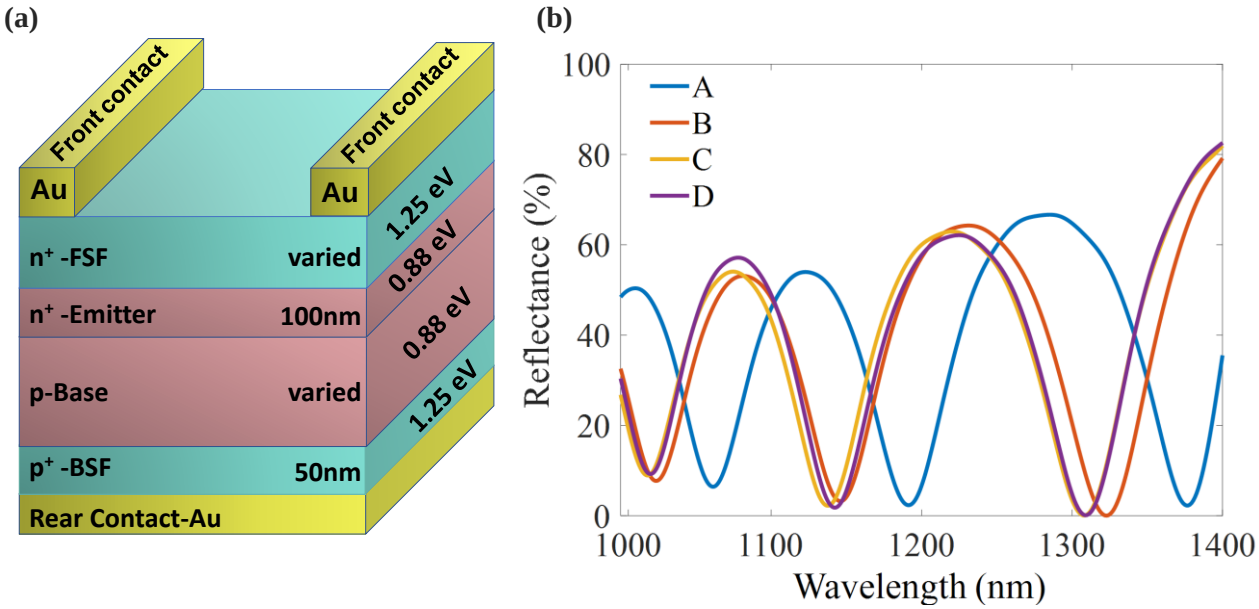

Figure 5.1: (a) 3D view of the thin PPC with flat BR, figure is not drawn to scale. (b) Resonances shift in reflection spectrum for thin PPC with flat back reflector for three different combinations of absorber and FSF layer thicknesses.

To highlight the light trapping effect of BR I compared performance of a thin PPC with absorber thickness of 770 nm to a conventional PPC with the same composition and layer thickness on the InP substrate without BR. In the following, I bring the results of this comparison that I presented as a poster presentation at *Numerical Simulation of Optoelectronic Devices (NUSOD) 2019* [93].

For this first simulations, experimental material properties were different than those indicated in chapter 4. Bandgap, absorption coefficient, and SRH carrier lifetime were 0.864 eV, $8.27\times10^{3}\,cm^{-1}$ and of 10e-6, respectively. Also in this first simulations a 100 nm Sio_2 ARC was incorporated. The thin design with a BR is termed "inverted" due to its inverted layer growth sequence and the conventional design on a substrate is termed "upright" due to its upright layer growth sequence. For both the inverted and upright structures, the cross-section of the multilayer structure, electrical field versus depth, and the absorbed power profiles are shown in Fig. 5. 2. Note that for comparison purposes the substrate of upright design is not depicted, although it was included in the simulations. The optical simulations demonstrated up to two times enhancement of

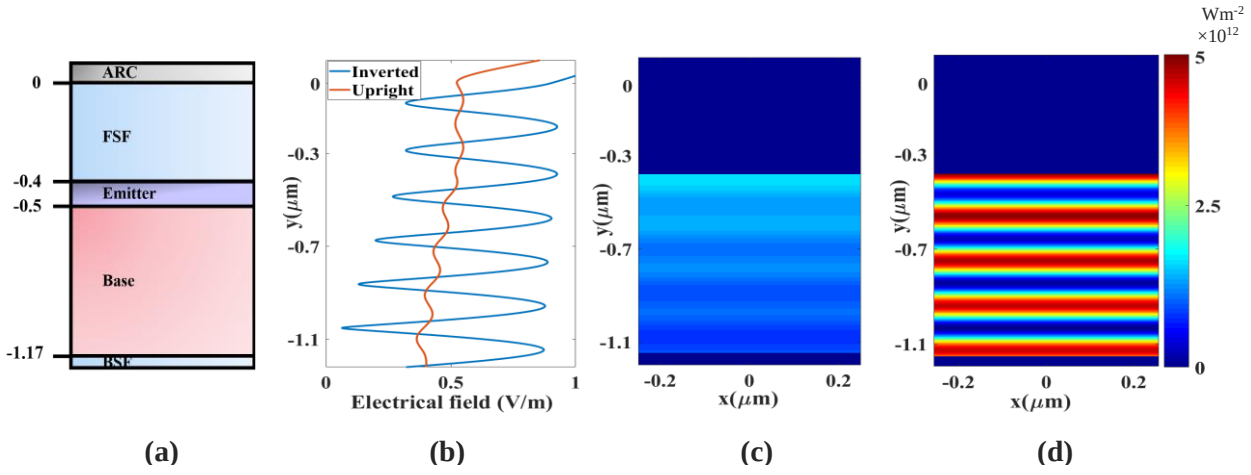

Figure 5.2: Optical simulations with FDTD method for the thin PPC with absorber thickness of 770 nm with and without BR: (a) Multilayer structure, (b) Electrical field versus position, (c) Absorbed power profile of upright design (note that substrate is not depicted), (d) Absorbed power profile of inverted design.

the photogenerated current for inverted structure as compared to the upright design. As shown in Fig. 5.2, as the light passes through the structure, the electrical field (b) and subsequently the absorbed power (c and d) is descending while accompanied with resonances. The mild resonances in the upright design arise from refractive index difference between active layer and the superstrate and substrate materials. However, for the inverted design, the BR provides strong Fabry-Perot effect and boosts the absorption within the thin absorption layer.

Table 5.2: Comparison of upright and inverted structure performance

	J_{sc} (mA/cm^2)	V_{oc} (V)	*FF*	Efficiency (%)
Upright	47.1	0.51	0.78	18.9
Inverted with BR	94.3	0.53	0.8	40.2

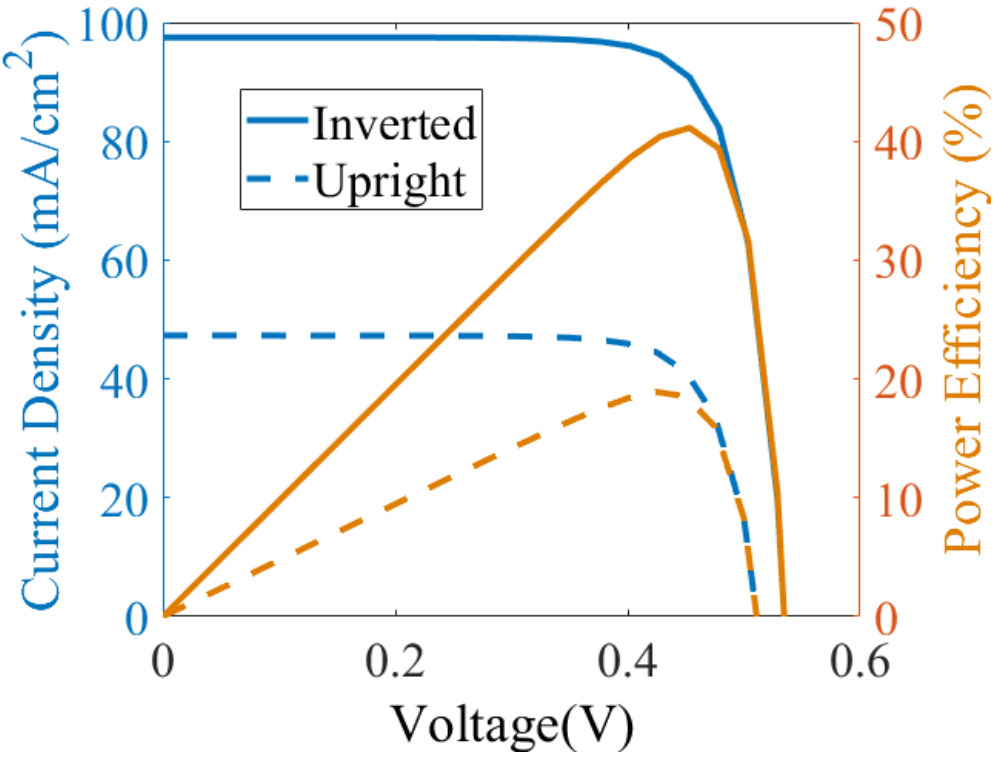

Figure 5.3: Comparison of current-voltage characteristics of the thin PPC with BR (Inverted) and without BR (Upright) under intensity of 100 mW/cm^2 at T=300 K.

Main performance parameters from electrical simulations for both structures are summarized in Table 5.2 and their *IV* characteristics are plotted in Fig 5.3. These results show improved efficiency by more than two times for the proposed structure with BR compared to the PPC without BR.

5.2. Thin PPC with pyramidal BR

Contrary to the solar cells where random texturing results in enhanced absorption [94], for monochromatic PPCs perfect absorption depends on the precise geometry of nano patterns. Thus, in addition to absorber and FSF layer thicknesses, the dimensions of pyramidal nanotextures including height, base width, and period of nano pyramids were also added to the design space parameters. Table. 5.3 presents couple of different combinations of design space parameters that results in adjustment of resonance dip in the reflection spectrum at 1310 nm. Comparing design, A and B shows how different design parameters can yield similar absorptance. Design C indicates how higher absorptance is attainable for the same active layer thickness as design B through variations of other design parameters.

Table 5.3: Summary of the variations of the design space parameters to align the resonance in the reflectance spectrum at 1310 nm for a thin PPC with a pyramidal nanotextured BR.

	Absorber (nm)	**FSF (nm)**	**Width (nm)**	**Height (nm)**	**Absorptance (%)**	**Reflectance (%)**
A	510	50	400	68	90.2	0.9
B	508	226	622	110	90.2	2
C	508	243	656	73	91.7	0.24

Fig. 5.4 (a) shows the 3D schematic of a PPC with a pyramidal nanotextured BR and Fig. 5.4 (b) illustrates the corresponding reflection spectrum for designs from Table.5.3. I presented the

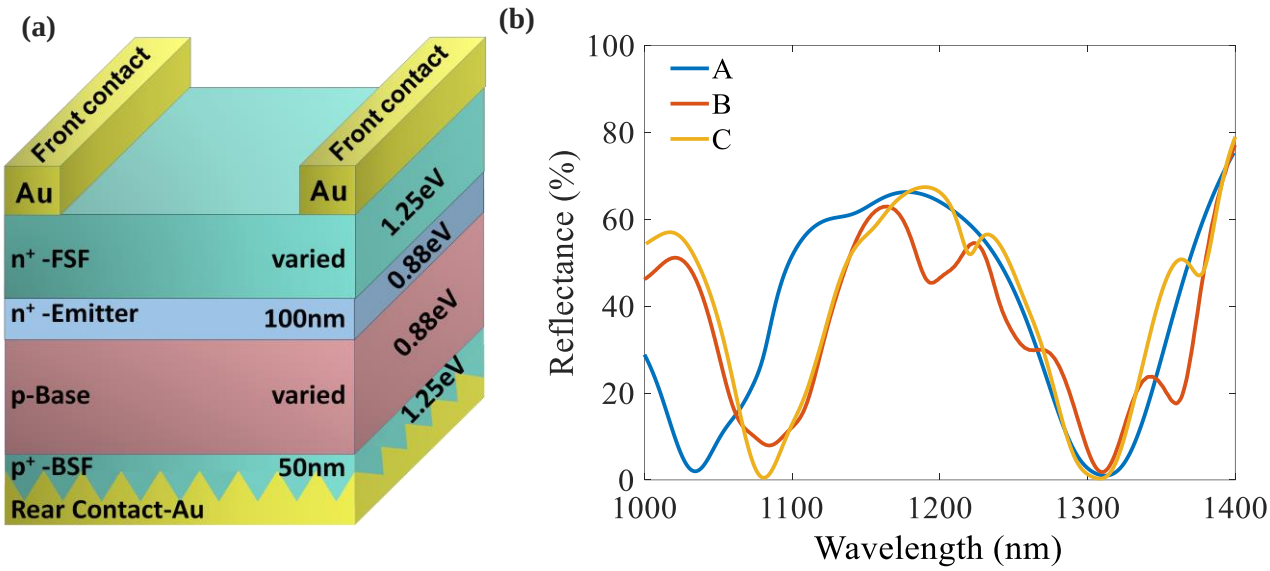

Figure 5.4: (a) 3D view of the thin PPC with pyramidal nanotextured back reflector, figure is not drawn to scale. (b) Reflection spectrum for different optimizations from Table 5.3.

results of pyramidal BR design and optoelectronic modeling at the *47th Photovoltaics Specialists' Conference* in 2020 and published them in the *Proceedings of the 47th Photovoltaics Specialists' Conference*. Portions of this proceeding are reproduced in this section with minor alterations for clarity [95]. In this work, I compared the performance of a thin PPC with pyramidal textured BR (TBR) and a thin PPC with flat BR (FBR) with approximately same absorptance. For both the

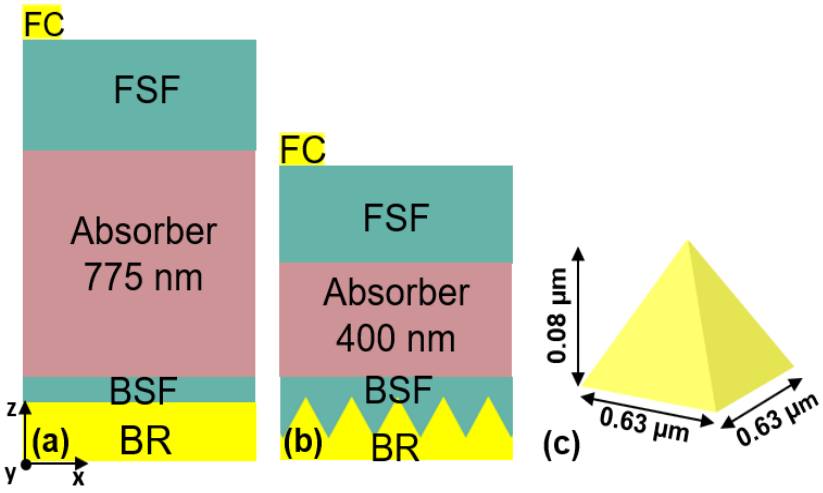

Figure 5.5: Schematic structure of PPCs with (a) flat and (b) textured back reflector. (c) Dimensions of the unit cell pyramid for the textured device. FC: Front contact. Figures are not drawn to scale.

FBR and TBR structures, the thicknesses of the absorber and FSF layers, as shown in Fig. 5.5 (a and b) are varied to align with the highest absorption resonances induced by the BR at 1310 nm. The base width and height of pyramids is adjusted to achieve near ideal absorption. The exact dimensions of the unit cell pyramid are shown in Fig. 5.5(c).

In order to demonstrate the role of the BR in amplifying absorptance via resonances, a conventional PPC on InP substrate and without a BR is also examined. This conventional PPC employs an absorber layer with a thickness of 4750 nm to absorb 98% of incident light at 1310 nm in a single pass. Since this design would employ a standard upright layer growth sequence, I refer it as the upright thick PPC design. Contrary to the thin PPCs proposed, an ARC is required to reduce the reflection loss of this upright device from about 30% to 7%. As can be seen in Fig. 5.6, for modeled devices with BR near zero reflection loss at 1310 nm is achieved without an ARC.

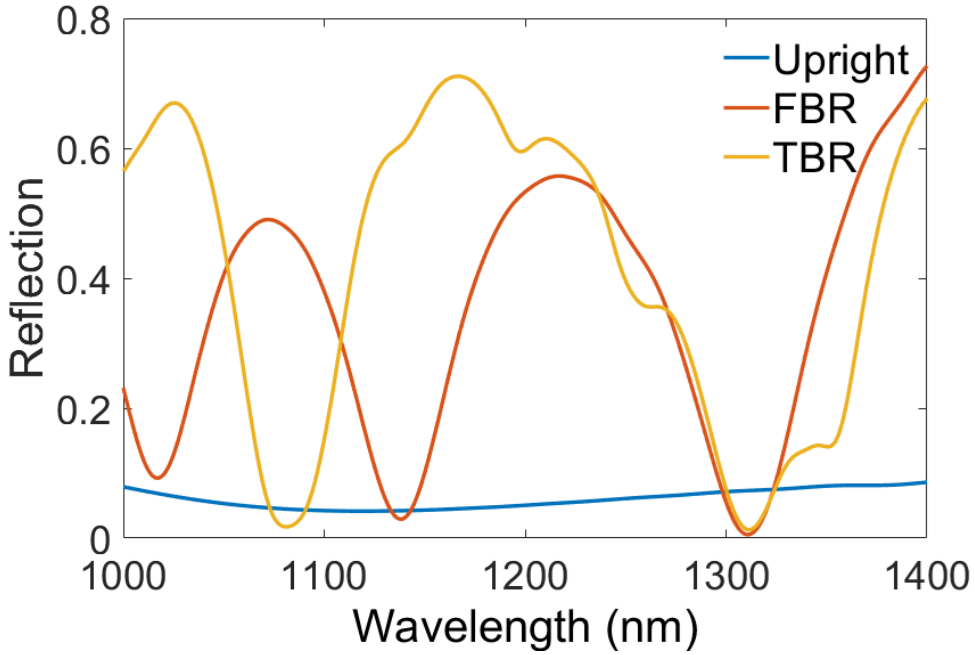

Figure 5.6: Full reflection spectra of Upright, FBR and TBR structures under normal incidence illumination. Due to resonances, near zero reflection loss for thin models are achieved at 1310 nm without an ARC.

I simulate the optical response of three structures: thick upright, FBR, and TBR, each under a plane wave illumination with center wavelength at 1310 nm, bandwidth 20 nm, intensity of 100 mW/cm^2, and device temperature of 25°C. Fig. 5.7 demonstrates how the BR boosts light trapping via strong Fabry-Perot resonances within the thin absorber layer in both FBR and TBR (b,c). As shown in Fig. 5.7(c), the TBR also induces guided mode resonances that further enhance absorption at the resonance wavelength.

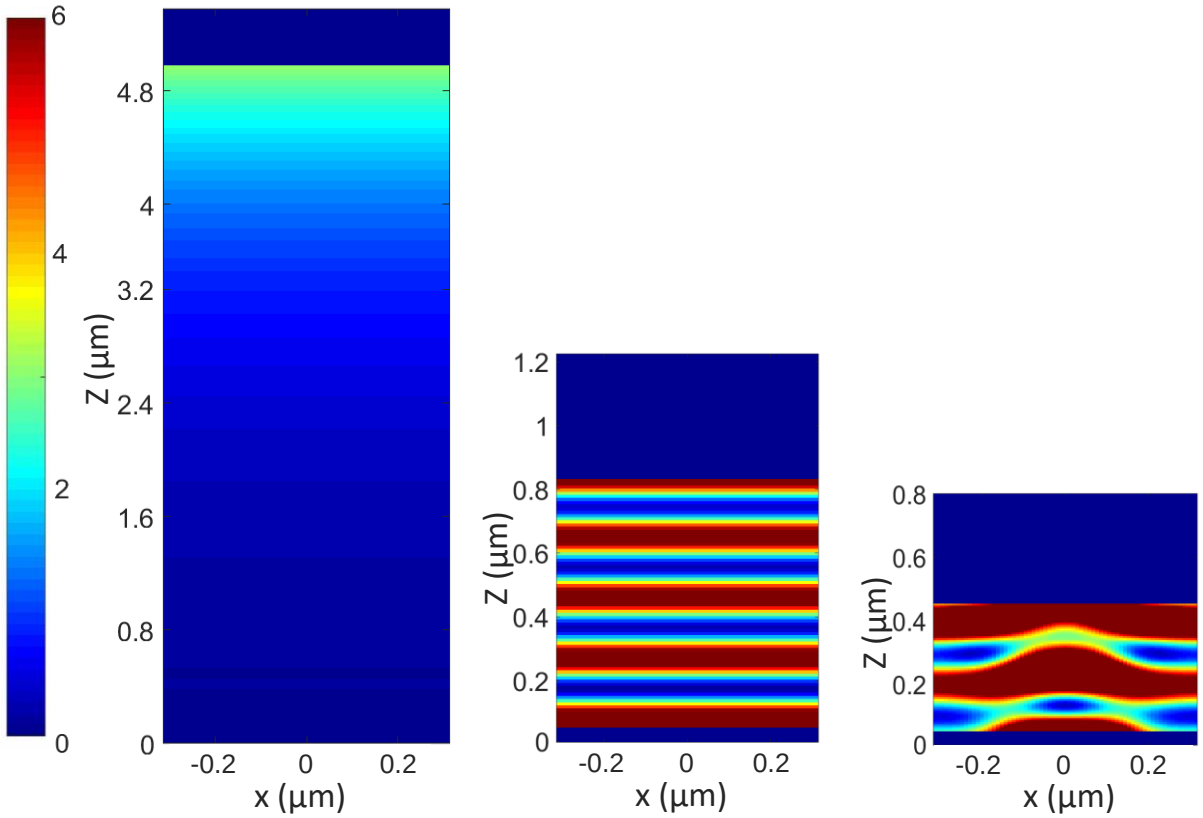

Figure 5.7: Optical simulations with FDTD method: Normalized cross- sectional absorbance profiles of (a) Thick upright, (b) FBR and (c) TBR structures.

I take the thick upright PPC as a baseline to which I compare the performance of the thin PPCs. The main performance parameters of these three structures are summarized in Table 5. 4. My results show approximately 6 times and 12 times thickness reduction for FBR and TBR devices,

Table 5.4: Performance comparison of different structures

Design Type	Absorber Thickness (nm)	J_{sc} (mA/cm^2)	2-pass J_{sc} (mA/cm^2)	V_{oc} (V)	*FF*	*PCE* (%)
Thick Upright	4750	93.8	-	0.55	0.81	42.3
Inverted with FBR	775	93.4	70	0.61	0.80	46.0
Inverted with TBR	400	92.9	49	0.62	0.79	46.1

respectively, relative to the thick upright structure, while maintaining J_{sc} within 1%. The thinner devices also benefit from an enhanced V_{oc} and hence efficiency. The higher V_{oc} in thin PPCs attributes to higher carrier concentration. Though V_{oc} in TBR is higher than FBR, but the slightly lower J_{sc} yielded in same efficiency for both devices. Simulations without front contact shading resulted in an efficiency of 48% for FBR and TBR devices which is about 9% enhancement in comparison with thick upright PPC. This high efficiency is caused by combined effects of strong light scattering and near-zero reflection loss. My results also reveal that J_{ph} of the FBR and TBR designs exceed the absorption expected from a simple double pass through the absorber layer by factor of 1.4 and 2 times, respectively. As expected, higher double pass absorption of the TBR verifies that pyramidal nanostructures have more light trapping capability than flat BRs.

5.3 Thin PPC with cubic BR

As with PPCs with pyramidal textured BRs, the thickness of the absorber and FSF layers as well as the width, height and period of nano cubes are required to be adjusted precisely to tune the resonance valley in the reflection spectrum to the desired wavelength and yield high absorption. Table. 5.5 shows some of the combinations of design space parameters for this model that resulted in resonances alignment at 1310 nm. Comparing A and B, we can see how different combinations of design parameters can result in the same absorptance. Also comparing B and C, we can see how

higher absorptance can be obtained for the same active layer thickness through variation of other design space parameters. The reflection spectrum of these designs is shown in Fig. 5.8 (b).

Table 5.5: Summary of the variations of the design space parameters to align the resonance in the reflectance spectrum at 1310 nm for a thin PPC with a pyramidal nanotextured BR.

	Absorber (nm)	FSF (nm)	Width (nm)	Space (nm)	Height (nm)	Absorptance (%)	Reflectance (%)
A	527	100	312	673	162	90	0.98
B	522	275	130	800	197	90	1.01
C	522	380	170	900	97	91.5	0.67

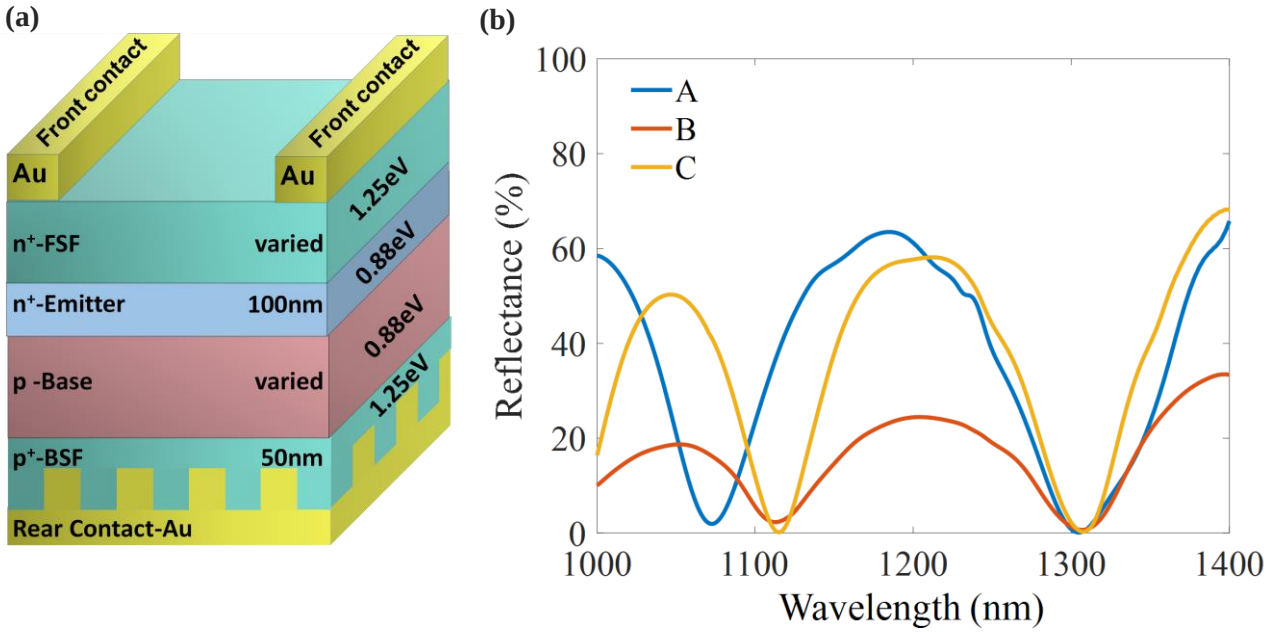

Figure 5.8: (a) 3D view of the thin PPC with cubic nanotextured back reflector (CBR), figure is not drawn to scale. (b) Reflection spectrum for different designs from Table 5.5.

I presented optoelectrical simulation results of light trapping in thin PPCs using cubic and pyramidal BRs at the *Photonics West 2021* conference [96]. Bandgap, absorption coefficient, and SRH carrier lifetime for these simulations were 0.87 eV, $5.3\times10^{3}\,cm^{-1}$, and 10e-6, respectively. For a unit cell of both modeled devices, the cross-sectional layer structure with corresponding

thicknesses and power absorption profiles are illustrated in Fig. 5.9 (a-d). Note that the power absorption profile color bar scale is different between the cubic BR and pyramidal BR. The dimensions of the nanotextures are depicted in Fig. 5.9 (e-f). Fig. 5.9 (f) shows that the nano pyramids dimensions are not equal in *x* and *y* directions, which makes these results dependent on the polarization of the incident light. As in previous sections, I used a convectional thick PPC with high (98%) absorptance as a baseline to evaluate the efficiency enhancement in thin PPCs. For fair comparison with thin PPCs, the reflection loss of the conventional PPC was reduced to near zero by incorporating a double layer ARC.

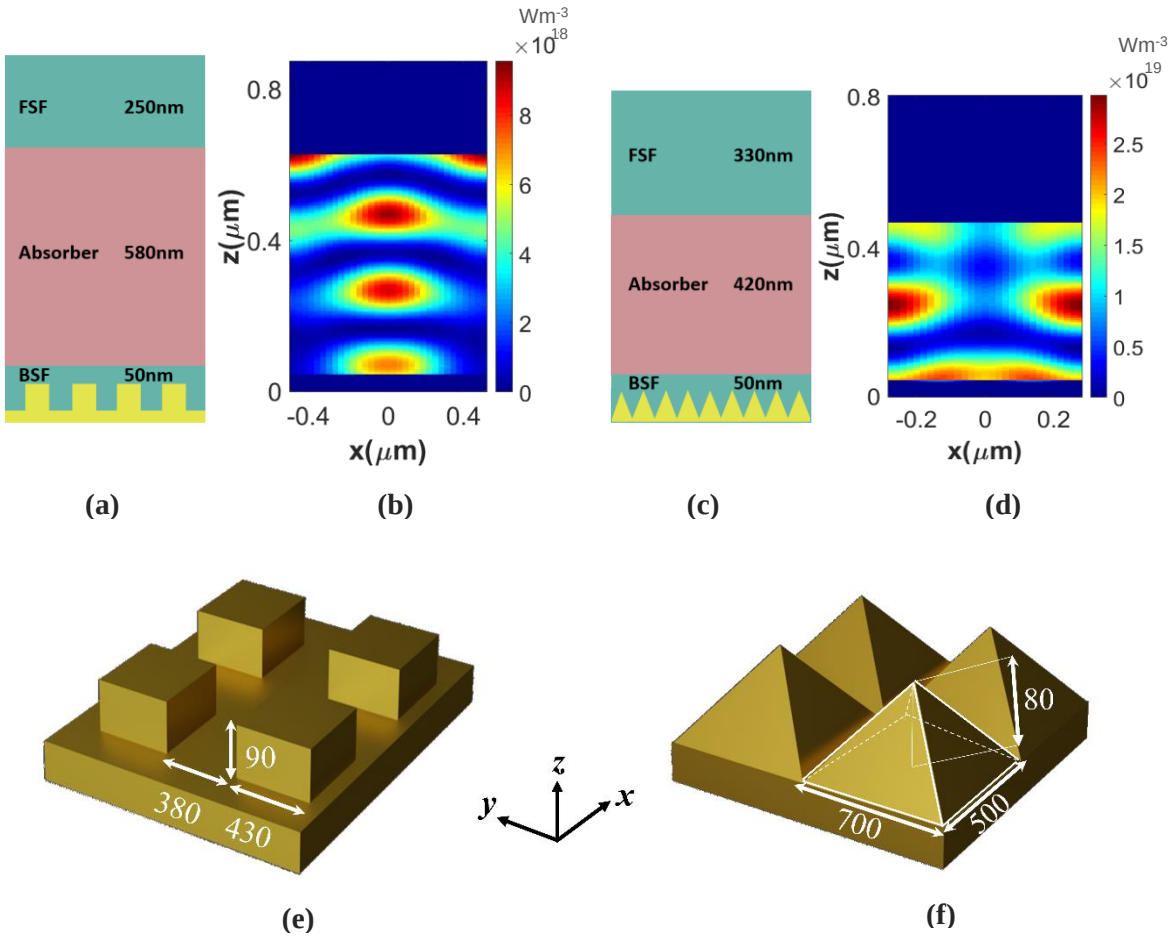

Figure 5.9: (a) Cross-sectional view, (b) absorption profile of the thin PPC with cubic BR. Note that color bars scale is different for two designs. (c) Cross-sectional view, (d) absorption profile of the thin PPC with cubic BR. (e-f) Dimensions (in nanometer) of the cubic and pyramidal nanotextures (not scaled).

The main performance parameters of these three structures are summarized in Table 5.6 and are illustrated in Fig. 5.10. These simulations demonstrated that 9- and 12-times thinner absorbing layers for cubic and pyramidal BR structures, respectively, can realize ~94% of the short-circuit

Table 5.6: Performance comparison of different structures

Design Type	Absorber Thickness (nm)	J_{sc} (mA/cm^2)	V_{oc} (V)	*FF* (%)	*PCE* (%)
Conventional	5170	97.86	0.51	80.4	40.5
Cubic BR	580	91.5	0.62	80	45.3
Pyramidal BR	420	90.2	0.64	79.4	45.7

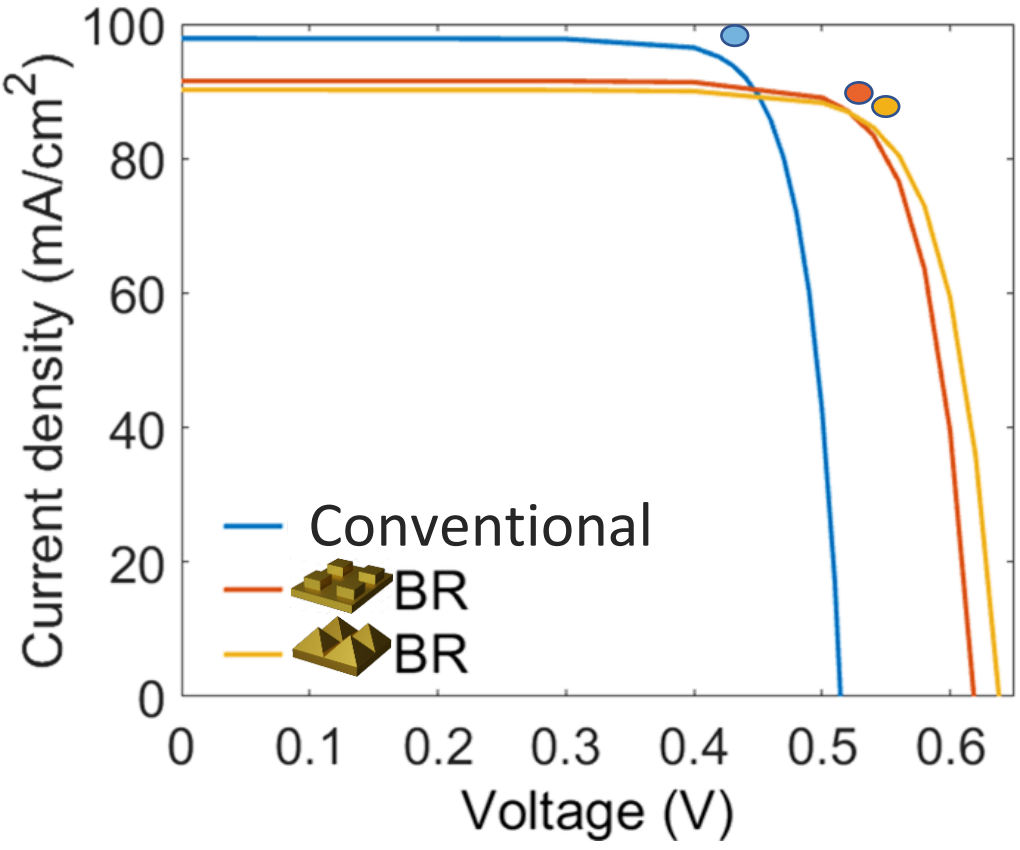

Figure 5.10: Current-voltage characteristics of the thin PPCs with cubic and pyramidal BR, and thick conventional PPC under intensity of 100 mW/cm^2 at T=300 K. Maximum power points are indicated by the colored circles.

current of the baseline thick structure while preserving fill factor within 1%. These designs also improve open-circuit voltage by 18-20% relative to the conventional PPC, resulting in a PCE increase of 12-13% (rel.).

5.4 Optimization

Until this point, my design approach was based on varying one parameter of the design space while keeping the rest fixed to find a combination that both satisfied resonance alignment at 1310 nm and minimized reflection losses. As showed in Tables 5.1, 5.3 and 5.5, multiple combination of design space parameters yields to resonance alignment at target wavelength but with different reflectance loss and absorptance. So, optimization tools are required to find the optimum combination that results in high absorptance while minimizing the absorber layer thickness. These optimizations can be carried out in two ways. The first approach involves reducing the absorber layer thickness, for example by making it 10 times thinner than for a conventional PPC with a high absorptance. Then, optimization can be performed at this fixed layer thickness to harvest as many photons as possible. The second approach is based on selecting a target absorptance and then performing a design optimization that finds the thinnest absorber layer possible. In this work, I selected the latter approach. Design optimization sought to minimize the absorber layer thickness while obtaining a target absorptance of 90%, corresponding to a J_{ph} of ~95 mA/cm^2. Fabry-Perot resonances were aligned to the target wavelength by tuning the optical cavity design, minimizing reflectance, and maximizing absorptance. Structure optimization varied the absorber and FSF layer thicknesses for the flat BR design. For the nanotextured BR designs, their geometrical parameters were added to the design space, consisting of the height *h*, width *w*, and spacing *s* for the cubic BR, and height *h* and base width *w* for the pyramidal BR. To avoid polarization dependence for normal incidence, nanostructure dimensions were kept equal in the *x* and *y* directions. In all cases,

the BSF layer thickness was fixed at 50 nm. These parameter spaces were investigated via a particle swarm algorithm, using photocurrent J_{ph} as the figure of merit. The following section is the reproduction of the optimization results with additional details that I published in *Optics Express* 2022 [97].

5.4.1. Conventional thick PPCs

To highlight the effect of a BR, I simulated two optically thick PPCs on InP substrates to use as baselines to compare the light harvesting capability and power conversion efficiencies of ultra-thin PPCs. One of the thick PPCs was simulated with high absorptance of 98% and the other with an absorptance of 90%, the same as for the optimized ultra-thin devices. I refer to these designs as "Ref 98%" and "Ref 90%", respectively. Based on the Beer-Lambert absorption law, the required absorber thicknesses for Ref 98% and Ref 90% are 5270 nm and 3100 nm, respectively.

Without an antireflection coating, Ref 98% and Ref 90% thick designs would suffer from ~30% and ~21% reflection loss, respectively. Fair comparison with ultrathin designs, which benefit from near zero reflection loss, requires minimizing the reflection loss in thick models. For Ref 98%, incorporating a single layer ARC in simulations and applying PSO reduces reflection loss to 6.47%, as shown in Fig. 5.11 (a). Next, by varying the thicknesses of the single layer SiO_2 ARC and FSF layer, reflection losses decreased to 3.45%, as shown in Fig. 5.11 (b). Finally,

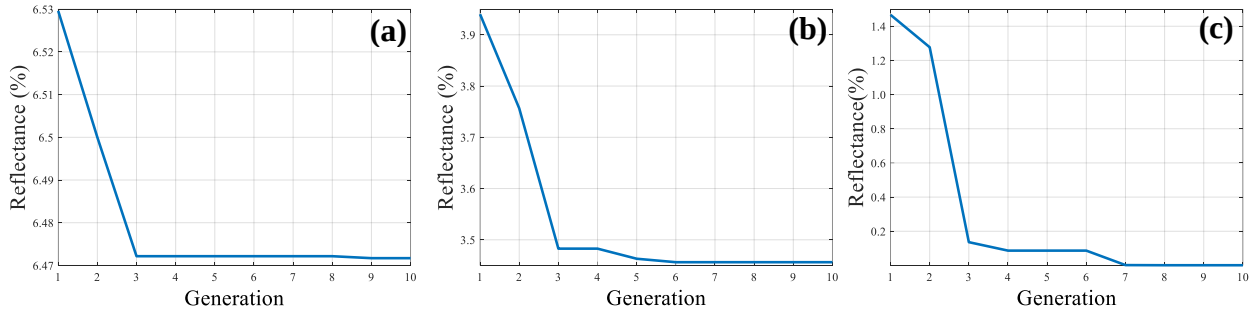

Figure 5.11: Minimization of reflection loss using particle swarm optimization (PSO). (a) Variation of ARC, (b) Variation of ARC and FSF layer, and (c) Variation of DLARC and FSF.

Fig. 5.11 (c) shows that by incorporating a double layer of SiO_2/TiO_2 ARC [98] and varying the thickness of the FSF layer, the lowest reflection loss of 0.03% was obtained. The refractive index of different layers at 1310 nm are as follows: Emitter and Base: 3.48, BSF and FSF: 3.24, SiO_2:

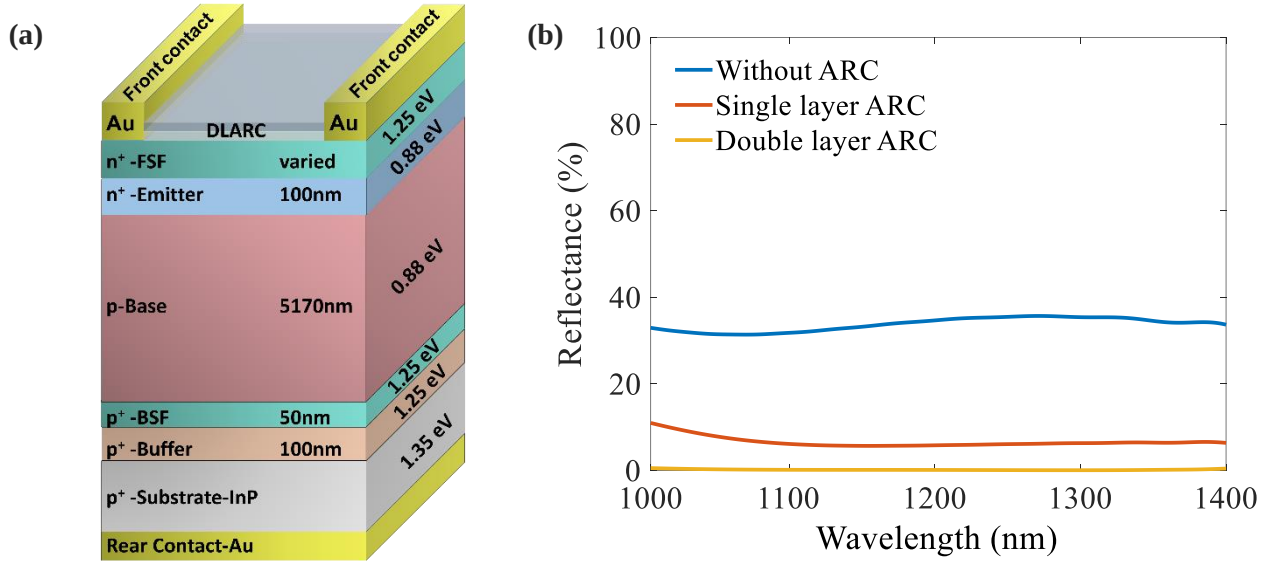

Figure 5.12: (a) 3D view of the conventional PPC with high absorption (98%), figure is not drawn to scale. (b) Reflection curve: without ARC (blue line), with single layer ARC (red line), and with double layer ARC (yellow line).

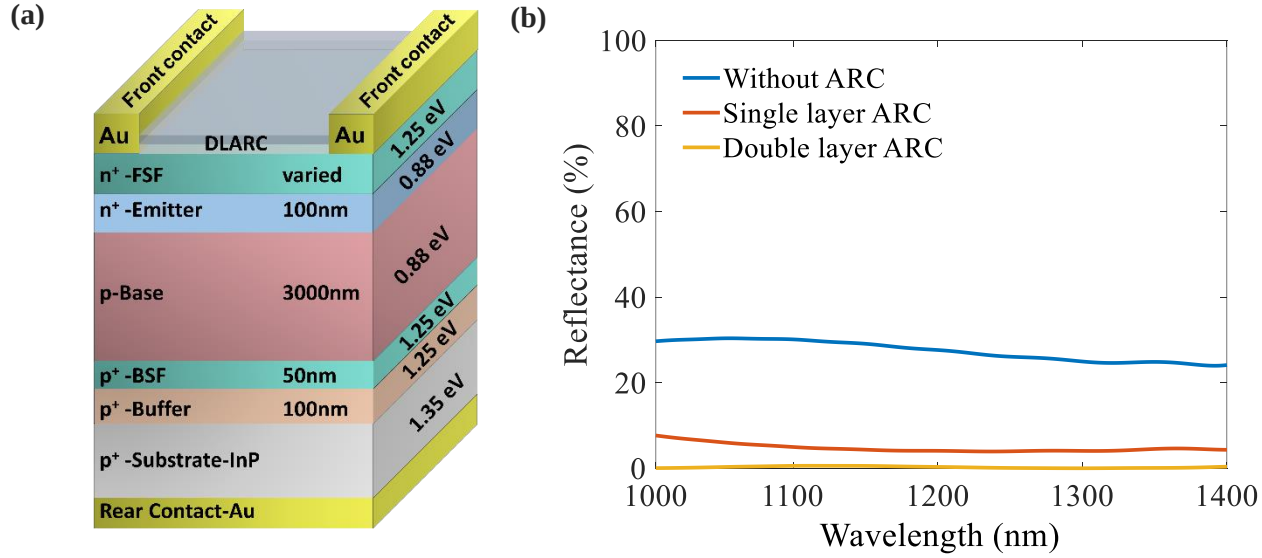

Figure 5.13: (a) 3D view of the conventional PPC with same absorption (90%) as ultra-thin PPCs, figure is not drawn to scale. (b) Reflection curve: without ARC (blue line), with single layer ARC (red line) and with double layer ARC (yellow line).

2.01, and TiO_2: 2.46. A 3D view of the Ref 98% design and reflection spectrum with and without incorporating ARC are shown in Fig. 5.12 (a) and (b), respectively.

Fig. 5.13 (a) shows the 3D view of the Ref 90% design. The same optimization approach was carried out to reduce the reflection loss of Ref 90% to 0.01% at 1310 nm as can be seen in Fig. 5.13 (b).

For these optically thick designs, the J_{ph} values obtained from simulations were about 0.02 mA/cm^2 lower than analytical calculations according to:

$$J_{ph,th} = \frac{qAP}{E_{ph}} \tag{5.1}$$

where $J_{ph,th}$ is the theoretical photocurrent, A is the absorptance, P is the input power, and E_{ph} is the energy of the incident photon.

5.4.2 Ultra-thin PPCs

Table 5.7 reports the optimized design parameters for 90% absorptance with corresponding primary optical losses, including parasitic absorption in the rear mirror and reflectance. For BR designs, a near-zero reflection loss was obtained without incorporating an ARC. Reflection spectra for all five designs from Table 5.7 are shown in Fig. 5.14.

The cross-sectional absorbed power profiles and corresponding J_{ph} values are depicted in Fig. 5.15 for all five structures: Ref 98%, Ref 90%, flat, cubic, and pyramidal BRs. For the thick reference PPCs, shown in Fig. 5.15 (a-b), most of the light absorption occurs near the front surface and decreases as less light penetrates deeper into the absorbing layer, as expected. However, for the ultra-thin planar structure in Fig. 5.2 (c) and nanotextured structures in Fig. 5.15 (d-e), the back mirrors create strong Fabry-Perot resonances in the absorptance profiles. Additionally, the nanotexture back mirrors also induce guided mode resonances that further enhance light trapping

at the resonance wavelength.

Table 5.7: Optimized parameters of PPCs with corresponding absorptance and optical losses at 1310 nm.

	Ref 98%	Ref 90%	Flat	Cubic	Pyramidal
ARC 2 (nm)	180	206	-	-	-
ARC 1 (nm)	94	122	-	-	-
FSF (nm)	214	299	240	300	170
Absorber (nm)	5270	3100	557	410	371
***w* (nm)**	-	-	-	290	653
***s* (nm)**	-	-	-	430	-
***h* (nm)**	-	-	-	93	108
Absorptance (%)	97.97	89.99	90.32	90.57	90.31
Reflectance (%)	0.03	0.01	2.38	0.01	0.04
Back reflector loss (%)	-	-	7.30	9.42	9.65

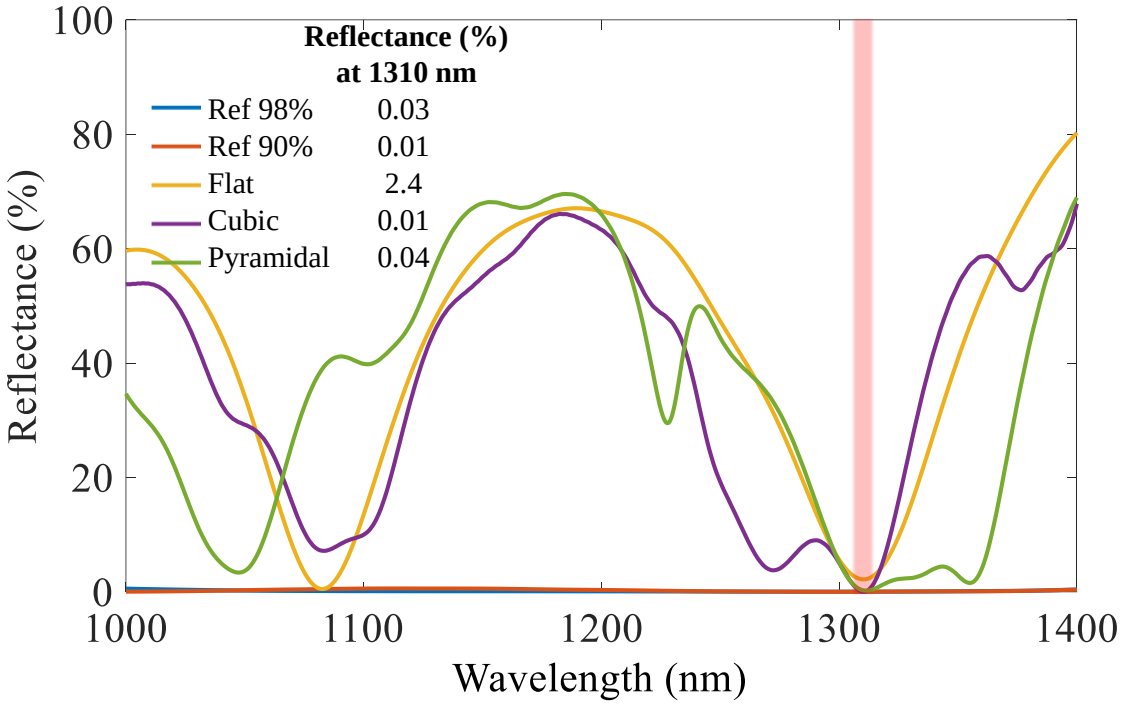

Figure 5.14: Reflection spectrum versus wavelength for all five optimized PPC designs, including optically thick (Ref 98%, Ref 90%) and ultra-thin (flat, cubic, and pyramidal back-reflectors). These designs were optimized for near zero reflection loss at 1310 nm wavelength. The laser spectrum centered at 1310 nm is indicated by the vertical line.

The 625-nm thick InP substrates of the reference designs are not fully depicted in Fig. 5.15, although they were included in the simulations. The J_{ph} values are close to 95 mA/cm^2 for the flat, cubic and pyramidal BR designs, indicating that they each absorb approximately 90% of the incident light despite reducing absorber layer thickness by 5.6, 7.6, and 8.4 times, respectively, relative to the Ref 90% structure. Compared to Ref 98%, flat, cubic and pyramidal structures achieve 9.5-, 12.5- and 14.2-fold reductions in the absorber layer thickness.

The light-trapping ability of a thin structure can be quantified by comparing it to the Beer-Lambert absorption through a material with twice its thickness. This emulates the expected

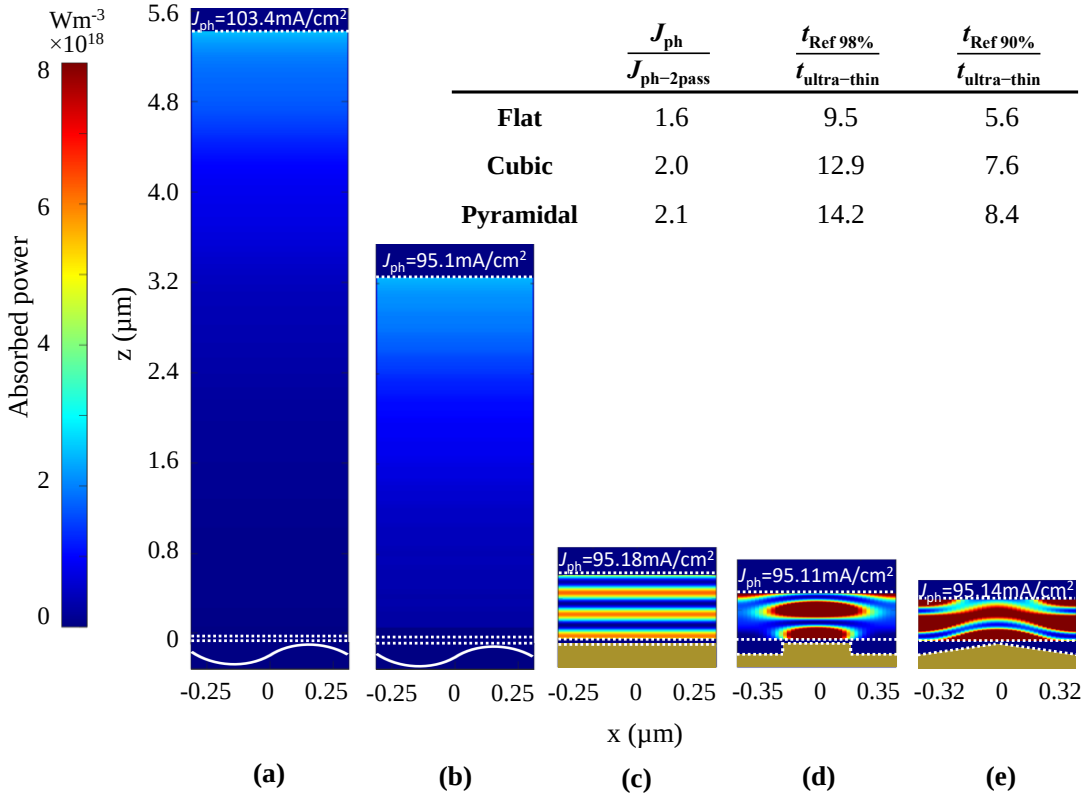

	$\frac{J_{ph}}{J_{ph-2pass}}$	$\frac{t_{Ref\ 98\%}}{t_{ultra-thin}}$	$\frac{t_{Ref\ 90\%}}{t_{ultra-thin}}$
Flat	1.6	9.5	5.6
Cubic	2.0	12.9	7.6
Pyramidal	2.1	14.2	8.4

Figure 5.15: Cross-sectional absorbed power profiles at y = 0 of each optimized PPC design: (a) Ref 98%, (b) Ref 90%, (c) flat, (d) cubic, and (e) pyramidal BRs. Inset table compares light trapping capability and thickness reduction of proposed PPCs (t: absorber thickness). Note that the x scales differ for each (d) and (e) compared to (a-c). The dotted white lines indicate material interfaces. The FSF and BSF, above and below the absorber, are transparent to the incident light. Only a small portion of the substrate is shown in (a) and (b), as indicated by the wavy lines.

absorption by two passes through the structure, assuming a perfect BR and no additional reflections or scattering. This two-pass photocurrent, $J_{ph\text{-}2pass}$, is calculated by Eq. 5.1 with A set as the Beer-Lambert absorptance for twice the absorber thickness of the corresponding design. In the ultra-thin designs, the optical cavity and guided-mode resonances result in simulated photocurrents that are enhanced by factors of 1.6, 2.0, and 2.1 for the flat, cubic, and pyramidal BRs, respectively, when compared to the two-pass case. The pyramidal BR design has the most significant reduction in absorber thickness, demonstrating its greater light scattering and trapping capability compared to planar and cubic nanotextured BRs.

The designs proposed here were optimized to minimize the absorber layer thickness while retaining 90% absorptance. However, alternative designs can also achieve nearly 90% absorptance slightly thicker absorber layers of 30-50 nm by using a different combination of design parameters such as FSF thickness and/or nanotexture dimensions [99], [100]. Allowing for slightly thicker absorber layers can thus broaden the design freedom significantly.

The reflectance spectra and resonance linewidths differ significantly between thin PPC designs (Fig. 5.14). For optical power transmission applications, resonances with wider linewidths are desired, as the operating wavelength of a laser can deviate due to manufacturing tolerances or temperature fluctuations [101], and performance can be affected by other conditions such as the illumination angle. Although Fig. 5.14 shows that we simulated near-zero reflection loss without incorporating an ARC, applying an ARC could increase the resonance linewidth and minimize reflection over a more extensive spectral range, therefore improving the stability and applicability of these devices. Such an ARC would also affect the optimum thickness of other layers due to interference effects and expand the design freedom.

Current-voltage characteristics and device efficiencies obtained from electrical simulations in Fig. 5.15 show that the ultra-thin designs with planar and textured BRs improve the V_{oc} by 12-14% and the PCE by 3-4% relative to the Ref 98% design. In comparison with the Ref 90% design, the optimized ultra-thin designs match the J_{sc}, boost the V_{oc} by 9-12%, and increase the PCE by 9-10% (relative). The higher efficiency in ultra-thin designs is caused by the increased open-circuit voltage, which is enabled by the strong light-trapping induced by the BRs.

The main parasitic optical loss for the ultra-thin PPCs is absorption in the back mirror [102], as shown in Table 5.7, which is worse for the textured structures that have more light trapping and thus more interaction between light and the back surface. The main electrical loss can be due to SRH carrier lifetime, which varies over orders of magnitude depending on the material quality. For example, for pyramidal nanotextured BR structures, an SRH lifetime in the InAlGaAs absorber

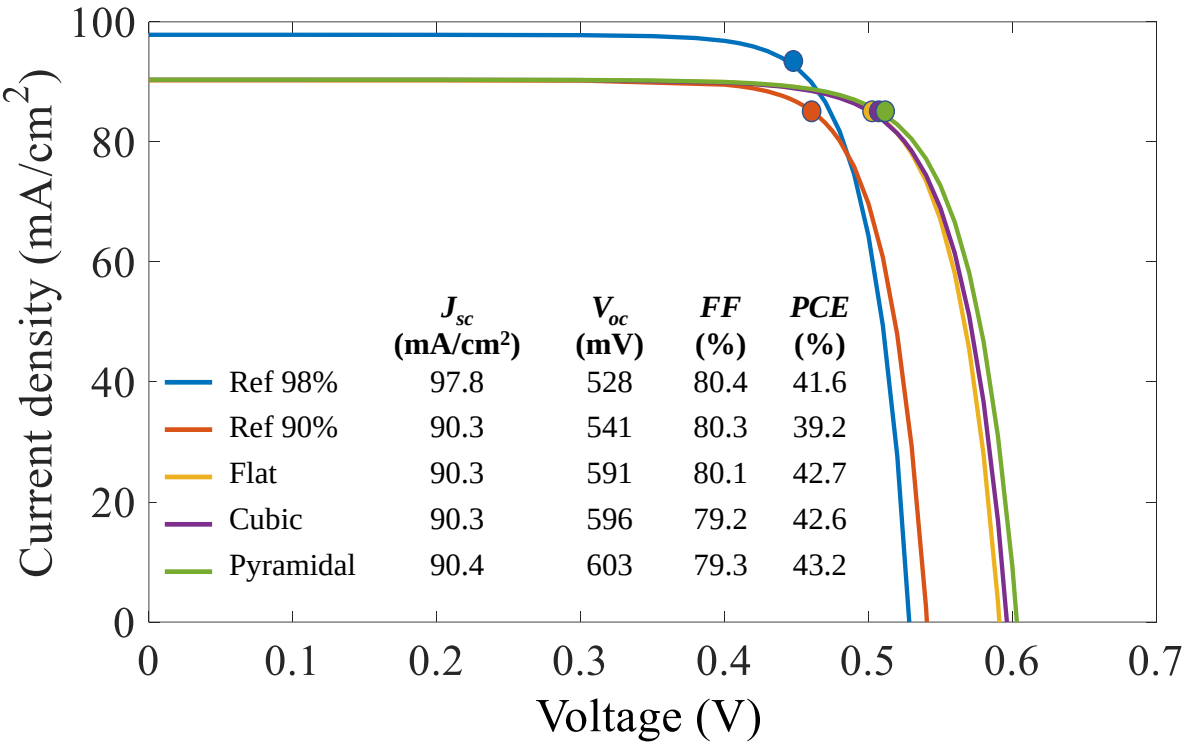

Figure 5.16: Current-voltage characteristics of the proposed PPCs under intensity of 100 mW/cm^2 at T=300K. Maximum power points are indicated by the colored circles.

layer of 10, 100, and 1000 ns results in efficiencies of 35%, 43.2%, and 46% [96], respectively. Real-world devices may include additional losses such as those from surface recombination and thermal effects such as heat from the laser illumination [103].

Further efficiency improvements could be achieved by shifting the absorber bandgap closer to the incident photon energy to reduce the thermalization loss [104], optimizing the front metallization [105], and employing higher quality material with longer carrier lifetimes. These simulations did not account for photon recycling effects, which would yield higher efficiencies in highly luminescent materials [26], [106].

5.5 Incident light intensity effect

The short circuit current, I_{sc}, depends linearly on the incident power density. However, by increasing the light intensity, the V_{oc} increases logarithmically according to Eq. 5.2:

$$V_{oc} = \frac{k_B T}{q} ln\left(\frac{X J_{sc}}{J_0} + 1\right) \tag{5.2}$$

where k_B is the Boltzmann's constant, T is absolute temperature, q is the elementary charge, X is the light intensity enhancement factor, J_{sc} is the short circuit current density, and J_0 is the dark saturation current density [70].

While J_{sc} linear enhancement under higher intensities does not improve efficiency as input power also increases linearly, logarithmic enhancement of V_{oc} provides an efficiency increase. I investigated the V_{oc}, *FF*, and PCE variations under higher intensities for all five models. As depicted in Fig. 5.17, as expected with increasing the light intensity, the V_{oc} increases for all five models. By increasing illumination intensity to 1 W/cm^2, the *FF* improves for all five models. The simulated efficiencies of the Ref 98%, Ref 90%, flat BR, cubic BR, and pyramidal BR designs increase to 47.1%, 44.3%, 49.1%, 49.3%, and 49.9%, respectively. At higher irradiances of 10

W/cm^2, the *FF* drops for thick models, which agrees with what was observed experimentally for optically thick PPCs [31]. Despite a decrease in the *FF*, the PCE of the Ref 98%, Ref 90%, flat BR, cubic BR and pyramidal BR designs rise to 50.5%, 47.6%, 55.1%, 55.7%, and 56.2%, respectively (Fig. 5.17). It is expected that under higher irradiance intensities, the efficiency would improve even further. However, there is a peak for efficiency, and after a particular intensity it begins to drop. Ohmic losses at higher intensities cause the *FF* to drop and consequently limit the PPC performance.

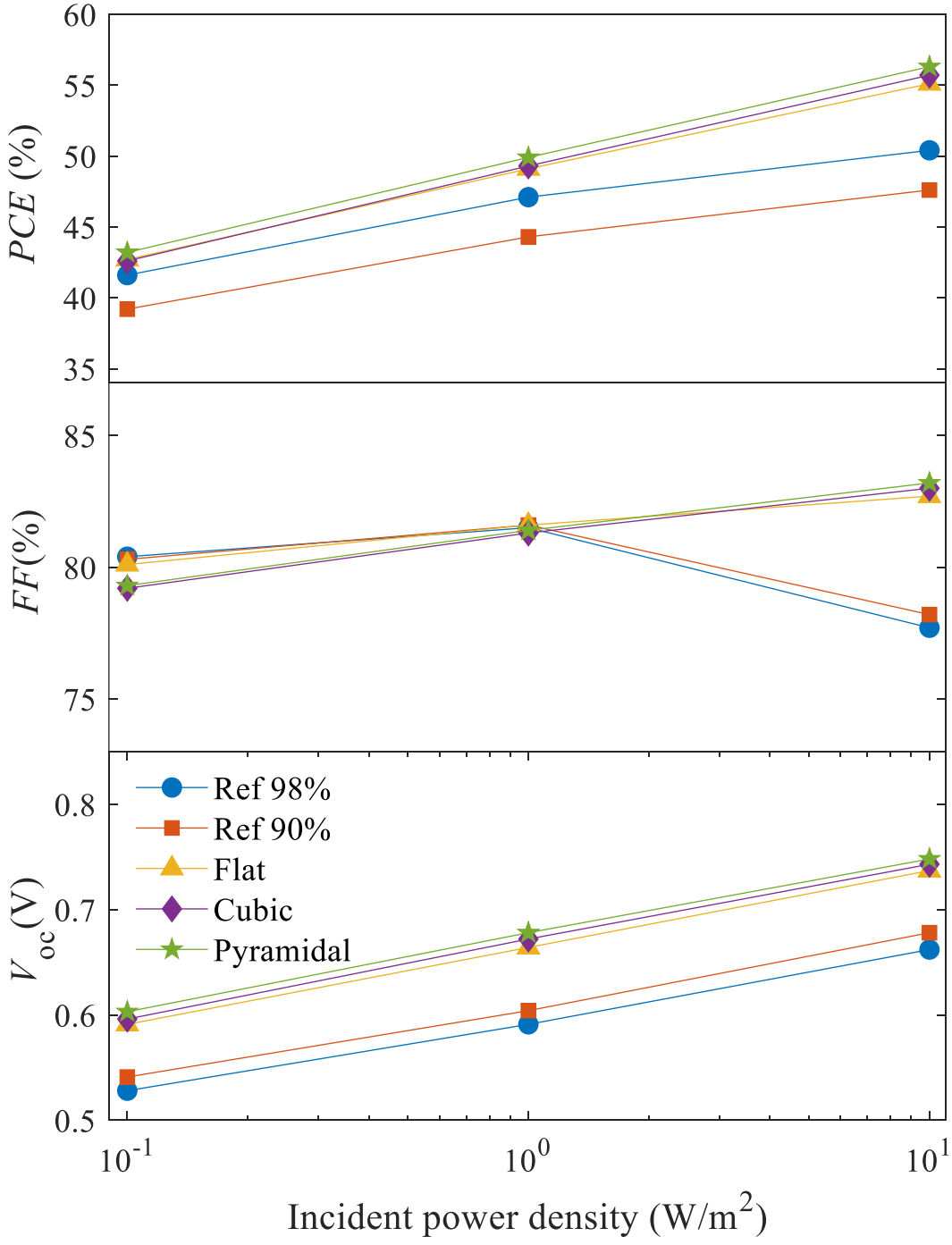

Figure 5.17: Comparison of V_{oc}, *FF* and PCE of five modeled PPCs under different intensities.

Chapter 6

OPTICAL DESIGN CONSIDERATIONS

In previous chapter, I showed through simulations that BR integration in thin and ultra-thin PPCs enables high light absorptance (by increasing the optical path length and minimizing reflection loss), while textured BRs exhibit superior light trapping capability than planar BRs due to guided mode resonances. In those designs, aligning BR-induced resonances at the wavelength of interest was crucial to achieve high absorptance. In this chapter, I use optical modeling to quantify the tolerance of optical absorptance to variation in the PPC's geometrical design parameters and wavelength of the incident light. I also proposed solutions for improving wavelength tolerance. I presented these results at *4th optical wireless power transmission conference 2022* [99], and *49th Photovoltaics Specialists Conference 2022* [100].

6.1 Tolerance study

Minimizing reflection losses and increasing the optical path length are two critical requirements for high absorption that can be satisfied by aligning BR-induced resonances at the wavelength of interest. However, resonance alignment may be compromised by: 1) deviation of a narrowband light source operational wavelength due to manufacturing imperfections and temperature fluctuations, 2) BR-induced resonance shift due to imperfect PPC fabrication processes, and 3) deviation of the incident light angle from normal incidence. While studies on thin broadband

photovoltaics with integrated BRs such as solar cells are mainly focused on increasing the resonance numbers for a broadband light spectrum [42], [107], in the case of monochromatic PPCs, a comprehensive tolerance and sensitivity study of the resonance alignment is required. In this section, I quantify the absorption's tolerance to variation in the PPC layer thicknesses and the incident light wavelength for PPCs with flat and textured BRs.

6.1.1 PPC with flat BR

Optical cavity formation between the BR and PPC layers leads to resonances in the absorptance (or reflectance) spectrum. The first design consideration is to tune the resonance peak in the absorption spectrum (or resonance dip in the reflection spectrum) to coincide with the target wavelength. Variations in refractive index and layer thicknesses result in a resonance shift due to interference effects. In this study, I investigated the sensitivity of the resonance peak to the absorber and FSF layer thicknesses, with fixed BSF layer thickness and material compositions, with target operation centered at a 1310 nm wavelength (Fig 6.1).

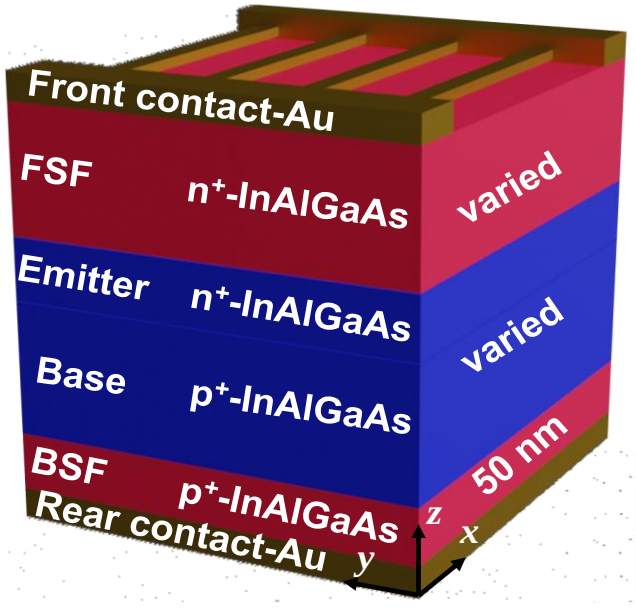

Figure 6.1: Schematic structure of modeled PPC with flat back reflector.

In optically thin designs, precise tuning of both absorber and FSF layer thicknesses is necessary to align the resonant peak of absorption with the operating wavelength. In Fig. 6.2, the 2D absorption map versus absorber and FSF thicknesses show that a ~90 nm variation in absorber layer thickness and ~100 nm change in FSF layer can shift the interference from constructive to destructive.

As shown in Fig. 6.2, multiple combinations of layer thicknesses result in high absorption, providing a degree of design freedom, but also illustrating that an increased absorber layer thickness does not universally guarantee increased absorption in these optically thin designs.

I selected four combinations of absorber and FSF thicknesses with approximately 92.8% absorption (designs within a ±0.3% range) at 1310 nm to compare their absorption spectra. Selected designs A through D with absorber and FSF layer thicknesses and corresponding absorption, reflection, and BR loss at 1310 nm are listed in Table 6.1. Parasitic absorptance in the BR for designs A and C with a 600 nm absorber layer is higher than for designs B and D with a

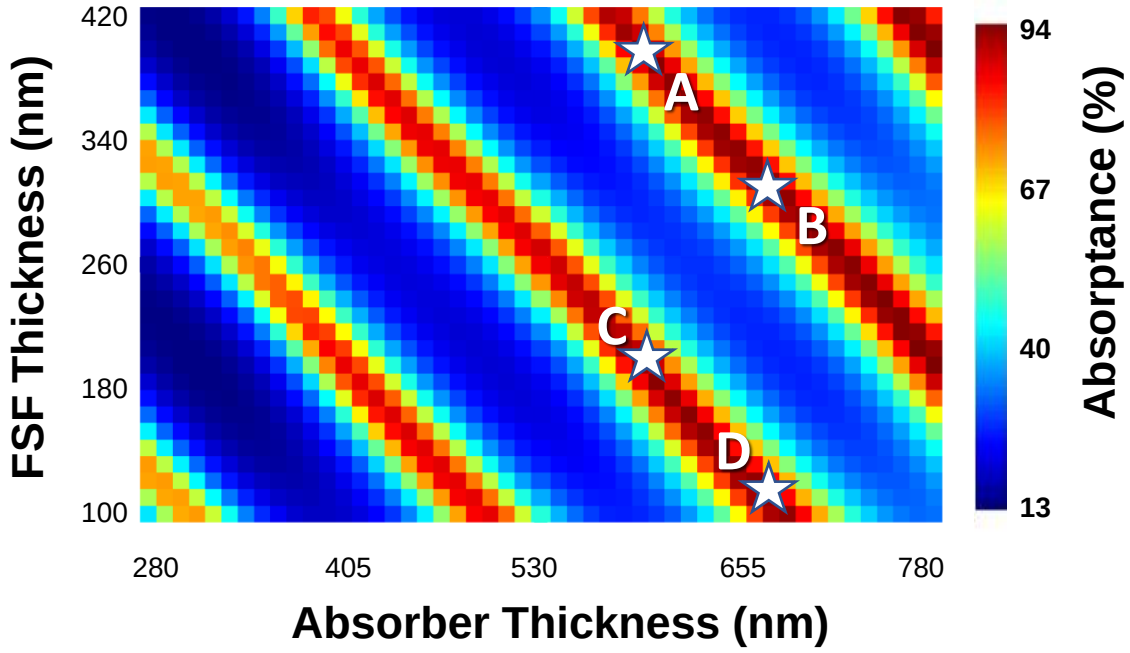

Figure 6.2: Absorption as a function of the absorber and FSF layers thickness for PPC with a planar BR.

665 nm absorber layer. This originates from the fact that thinner absorbers provide the same light absorption as thicker ones through more round trips at the resonance wavelength. Hence, more interaction with the back mirror yields more parasitic absorption.

Table 6.1: Layer thicknesses, absorption, and losses at 1310 nm for four designs with similar absorption for a thin PPC with flat BR.

	Design			
	A	**B**	**C**	**D**
Absorber (nm)	600	665	600	665
FSF (nm)	390	320	188	118
Absorption (%)	92.5	93.1	92.5	92.9
Reflection (%)	0.6	0.8	0.6	0.8
Back reflector loss (%)	6.9	6.1	6.9	6.3

Comparing the absorptance spectrum for all four designs over a spectral range of 1000-1400 nm in Fig. 6.3, we notice that the absorption spectra of designs A and C closely match the spectra for designs B and D, respectively. At 1310 nm, the resonance widths broaden from design A to D. Although for narrowband incident light within a 10 nm linewidth, absorptance is not affected significantly by resonance widths, wider resonances are more desirable due to operational laser wavelength deviations caused by fabrication variations and temperature fluctuations. For a better view of the resonance widths, the magnified resonance shapes for designs A and D are illustrated in Fig. 6.3 inset.

Table 6.2 reports the absorption of all four designs for 0-, 10-, and 20-nm deviations of the illuminated light from the design wavelength of 1310 nm. These results emphasize the importance

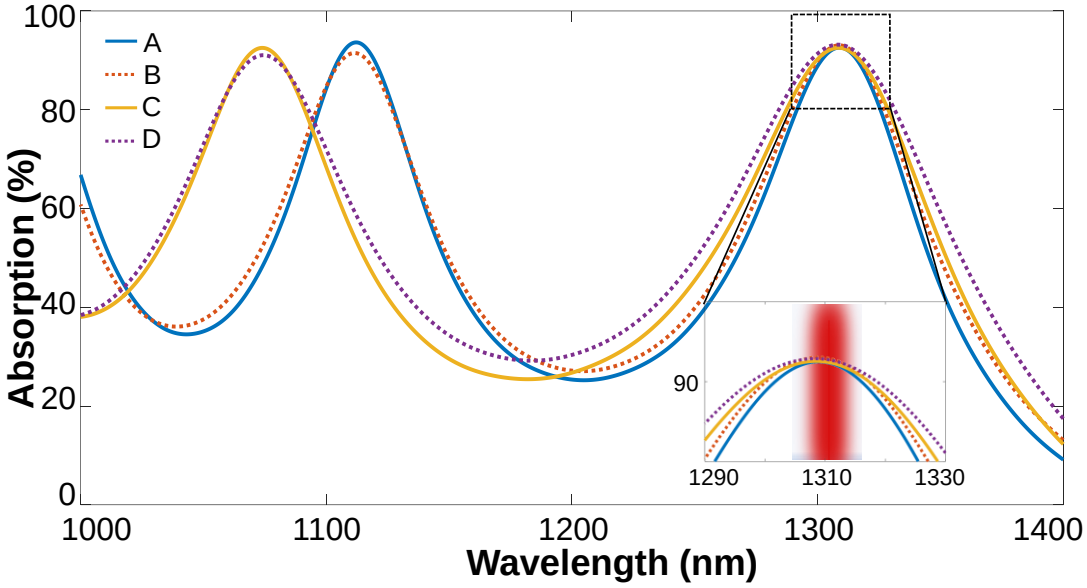

Figure 6.3: Absorption spectra of four different combinations of absorber and FSF layer thicknesses with approximately the same absorptance at 1310 nm. Zoomed spectra of A and D are illustrated in the inset with sample laser input at 1310 nm with a 10 nm linewidth.

of the resonance width and verify that resonances with wider widths are less sensitive to manufacturing tolerance and temperature instability.

Table 6.2: Absorption as a function of laser wavelength for a thin PPC with flat BR.

Deviation from 1310 nm	A	B	C	D
0 nm	92.5	93.1	92.5	92.9
-10 nm	88.8	89.9	90.52	91.4
-20 nm	79.0	81.2	83.9	85.8

6.1.2 PPC with textured BR

In the case of PPCs with pyramidal nanotexture BR, I investigated the sensitivity of the resonance peak to the absorber and FSF layer thicknesses, and the geometry of the nano pyramids including

their height *h*, and base width *w*, while the BSF layer thickness and material compositions were kept fixed. These parameters are described visually in Fig. 6.4.

Fig. 6.5 shows absorptance maps of the optimized PPC as a function of (a) absorber and FSF layer thickness, and (b) width and height of nanotextured BR pyramids. In each case, the remaining design parameters were fixed to the values specified with a cross mark on each map.

These results show that an inversion from constructive to destructive interference occurs with variations of 60-70 nm and 70-80 nm for the absorber and FSF layer thicknesses, respectively. For the BR design, a 50 nm variation of width or height can drop absorptance by >25%. We note that a thick absorber layer does not universally guarantee high absorption, and therefore the absorber and FSF layer thicknesses and nano pyramid dimensions must all be simultaneously and precisely tuned to produce a resonance peak at the desired wavelength.

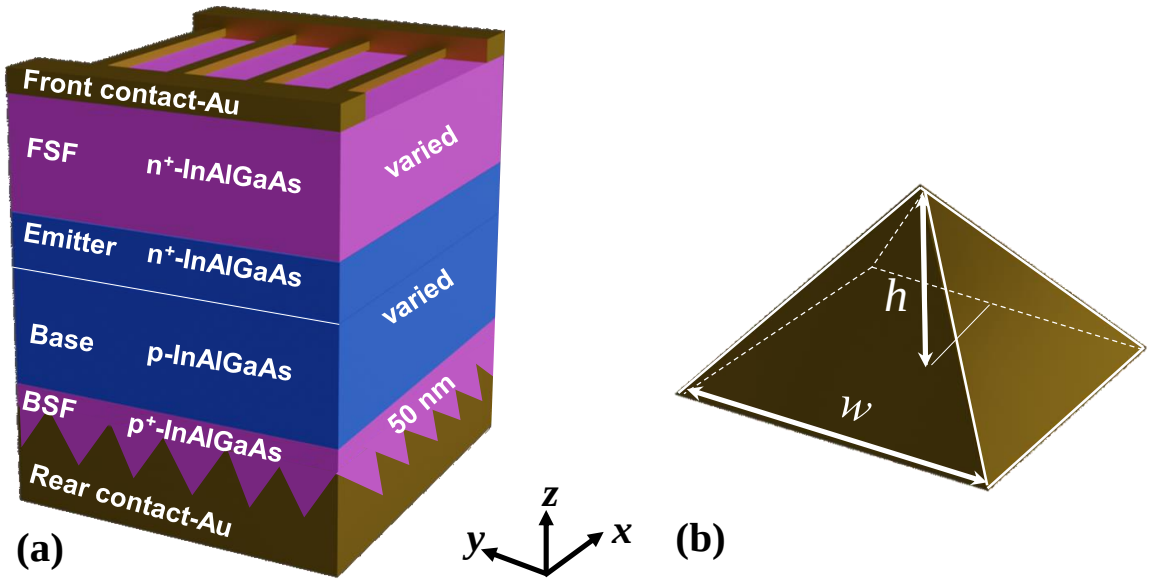

Figure 6.4: (a) Schematic structure of ultra-thin PPCs with pyramidal textured back reflector. (b) Dimensions of pyramidal back reflector with height *h* and base width *w* indicated.

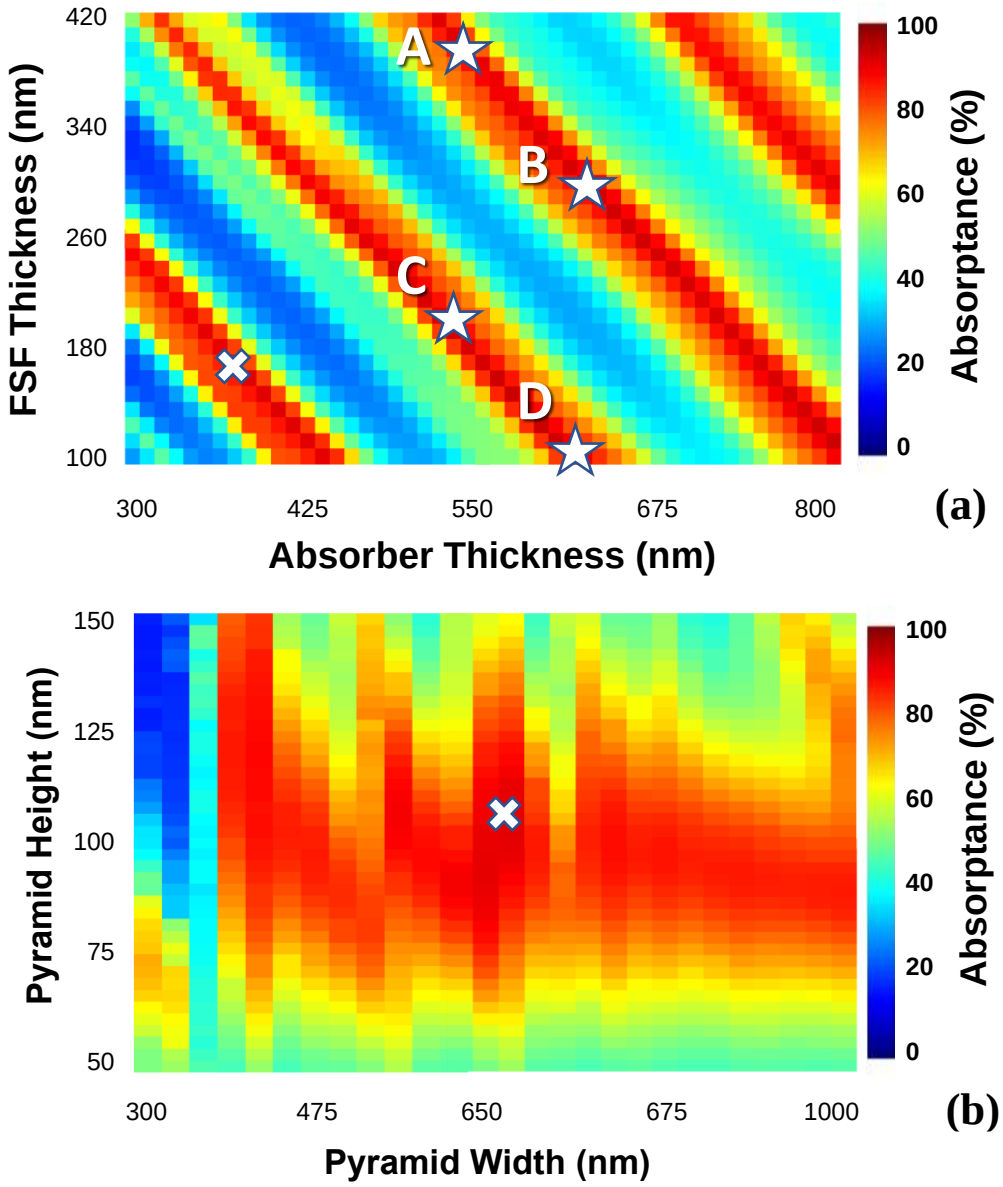

Figure 6.5: Absorptance as a function of: (a) absorber and FSF layers thicknesses; (b) height and width of the back reflector nanotextured square pyramids.

As evident from Fig. 6.4, multiple combinations of design space parameters result in high absorptance, enabling considerable design freedom. To compare differing high-absorptance designs, I investigated the absorptance spectra of four combinations of absorber and FSF layer thicknesses, each with an absorptance of 90.25±0.05% at 1310 nm. The absorptance, reflectance, and BR loss at 1310 nm for these selected designs A-D are listed in Table 6.3. Parasitic BR loss is

Table 6.3: Layer thickness and losses at 1310 nm, and Absorptance as a function of laser wavelength for four designs with similar total absorptance.

		Design			
		A	***B***	***C***	***D***
Absorber (nm)		540	610	540	610
FSF (nm)		398	314	175	100
Reflectance (%)		1.5	1.9	1.6	2.2
Back reflector loss (%)		8.3	7.9	8.1	7.5
Absorptance (%)	1310 nm	90.2	90.2	90.3	90.3
	1320 nm	85	86.4	86.7	85.3
	1330 nm	81	83	78.0	74.5
	1340 nm	84.2	83.8	68.4	63.6
	1350 nm	79.0	78.1	61.2	55.2

dependent upon the number of round trips at the resonance wavelength, yielding a greater interaction with the back mirror where scattering and absorption can occur. This effect is

demonstrated by comparing designs A and C with 540 nm thick absorbers to designs B and D with 610 nm thick absorbers, where the thinner designs result in higher BR loss.

The inset of Fig. 6.6 compares the absorptance spectra for all four designs over a spectral range of 1000-1400 nm. We notice that the absorptance spectra of design A closely matches the spectra for design B, exhibiting overlapping resonances around 1310 nm, and the spectra of design C matches design D. In the case of laser-illuminated PPCs, where spectral linewidth of the incident

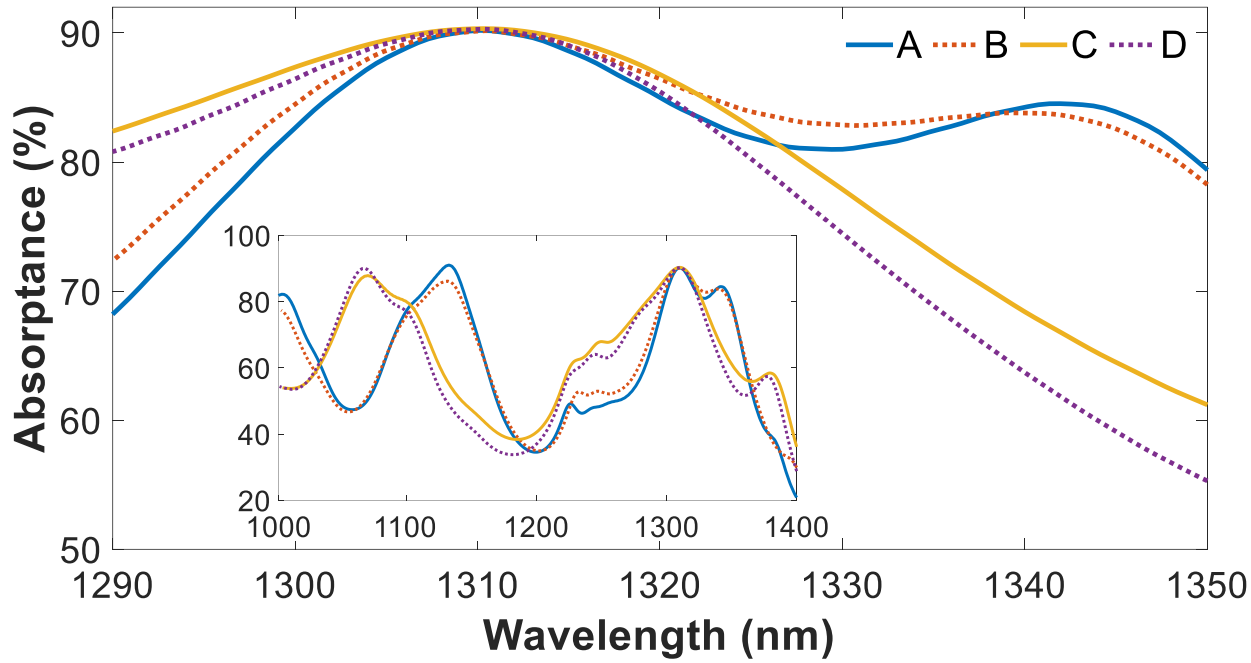

Figure 6.6: Absorptance spectra of four combinations of absorber and FSF layer thicknesses, yielding similar absorptance at 1310 nm but varying peak widths. Inset shows the absorptance spectra over a broadened wavelength range of 1000-1400 nm.

light is ~10 nm, these variations of the resonance widths can be negligible under ideal conditions. However, wider resonances are more tolerant to wavelength deviations due to laser fabrication variations and temperature instabilities [101], or deviation of incidence angle from the normal. Resonance shapes for designs A-D are shown in Fig. 6.6, demonstrating the variation in peak widths across designs.

Table 6.4 reports the absorptance of each design for wavelength deviations of 0 to +40 nm from the design wavelength of 1310 nm. Among these designs, A and B are more wavelength-tolerant with overlapping resonances near 1310 nm and absorptance drops of ~ 5.2-11.2% and 3.8-12.1% (abs.), respectively, for 10-40 nm wavelength deviations. Design D is least tolerant with 9.1-35.1% (abs.) absorptance drop under the same conditions.

6.2 Improving wavelength tolerance

In broadband photovoltaics (e.g. solar cells), it is common to add a single or double-layer ARC to minimize reflection losses across the broad solar spectrum. In the case of PPCs under narrow- band illumination, reflection can be minimized by aligning BR-induced resonances at the wavelength of interest without an ARC. For the ultra-thin PPC with pyramidal nanotextured BR shown in Section 6.1.2 (Fig. 6.4), I achieved near-zero reflection loss for a wavelength of 1310 nm without incorporating an ARC. I now investigate how adding an ARC layer can affect the wavelength tolerance for a thin PPC with a pyramidal nanotextured BR. The spectral reflectance of the optimized device from Section 6.1.2, which is taken as a baseline design, is shown as the blue dotted line in Fig. 6.7. By adding a single layer SiO_2 ARC, the optimization further minimizes the reflectance in the wavelengths around 1310 nm, as indicated by the solid blue line of Fig. 6.7. Due to high simulation times and memory requirements, both optimizations were performed over a single wavelength at 1310 nm. As shown in Fig. 6.7, the resulting reflectance spectra were not symmetric around 1310 nm, making these designs more tolerant to longer wavelength variations.

Table 6.4: Optimized parameters of pyramidal nanotextured PPCs with and without ARC.

Parameters thicknesses	**Optimization**			
	1310		***1310±20***	
ARC (nm)	0	101	0	143
FSF (nm)	170	155	143	140
Absorber (nm)	371	372	366	375
Width (nm)	653	652	456	648
Height (nm)	108	135	163	113

To form a more symmetrical and wider tolerance, I extended optimizations over a wider bandwidth of 1310 nm±20 nm both with and without ARC incorporation. The parameters of four optimized designs which are illustrated in Fig. 6.7, are listed in Table. 6.4. For a fair comparison of these optimizations, the absorber layer thickness was selected to be the same as the baseline design, (371 nm) ±10 nm for minimum and maximum limits.

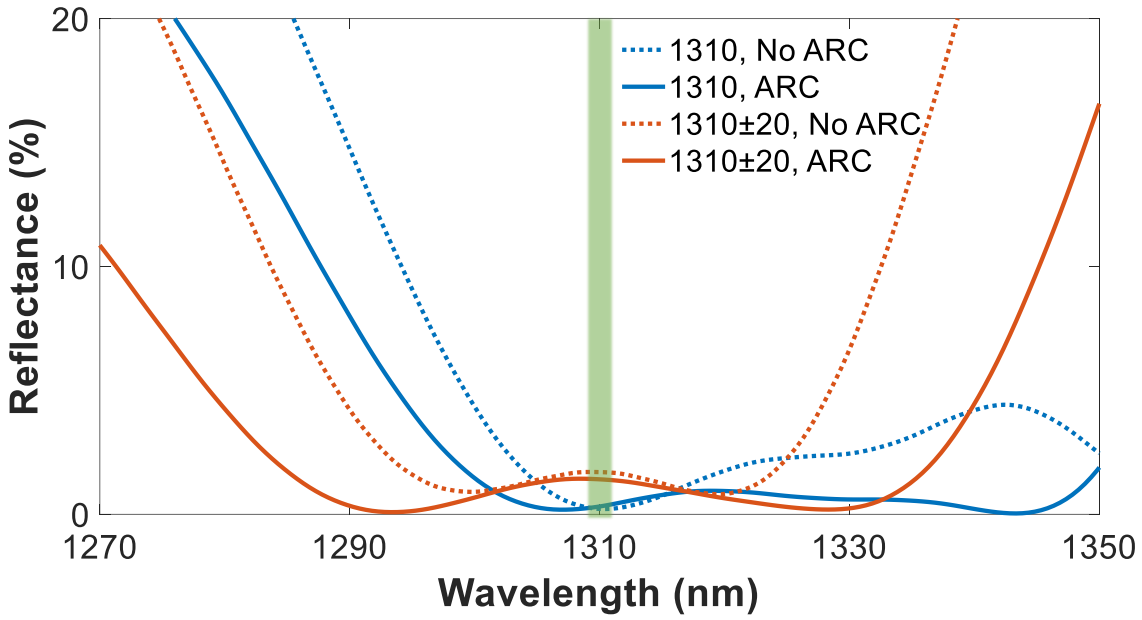

Figure 6.7: Reflectance spectra of optimized ultra-thin PPCs with and without ARC (solid and dashed lines) for single (1310 nm) and wide (over 1290 to 1330 nm) optimization (blue and red lines). The vertical green line indicates laser bandwidth.

Compared to the optimizations for the single wavelength, these results show reflectance spectra that are centered on the design wavelength, although at the cost of increased reflectance at 1310 nm. While the optimization without ARC, shown as the dashed red line in Fig. 6.7, does not exhibit satisfactory performance, the optimized design with ARC, represented as the solid red line, shows a relatively flat absorption across the optimized wavelength range.

6.3 Fabrication feasibility

Besides considerations such as the accuracy of the simulation results and tolerance study, the feasibility of fabrication is an important criterion that should be taken into account during the design process. Epitaxial growth of layers with different compositions with precise thickness (at the atomic level) can be realized using the MBE method [101]. As discussed in chapter 3, to fabricate a device with a BR, the structure should be grown epitaxially in a reverse sequence on the substrate. The BR is fabricated on the top layer of the inverted structure by depositing a layer of metal which also acts as the bottom contact in the final manufactured device. Next, the metal layer is bonded to a second substrate, which supports the device physically and allows us to remove the growth substrate inverting the structure. Implementation of nanotexture BRs can be realized using nanoimprint lithography as discussed in [75]. The nanoimprint lithography technique allows fabrication of patterned nanostructures on large scales with high precision and low cost [108]. Nanoimprinting lithography has been shown in recent years to enable the growth of various nanopatterns with sub-10 nm features and good critical control of side wall formation [103][109]. These show that it is a strong candidate for fabricating cubes with precise 90° corners and pyramids with exact desired angles. Combining nanoimprint lithography with plasma etching allows control of the sidewall angles with a precision of 1° [110], which is a crucial requirement in the fabrication of pyramidal nanotextures. Indeed, tuning the plasma chemistry and bias power of a plasma process, one can have control over the sidewall profiles of the nanotextures [111]. Patterning a sharp peak for the pyramidal structure is however challenging and may require the combination of additional, complementary techniques. Grayscale lithography [112] enables patterning a photoresist mask with a varying thicknesses, which could simply pattern transfer in the

semiconductor. Furthermore, advanced plasma etching techniques could leverage mask faceting [113] to create sloped sidewalls with a specific angle.

Chapter

7 SUMMARY AND OUTLOOK

7.1 Summary

In this work, I presented the design, simulation, and optimization of light management in highly efficient ultra-thin PPCs, comparing the simulated performance of flat, cubic, and pyramidal nanotextured BRs under 1310 nm narrow-band illumination. Due to strong Fabry-Perot and guided mode BR induced resonances, we attained near-zero reflection loss in the ultra-thin PPCs without using an ARC. Compared to conventional thick PPCs on a substrate, modeled ultra-thin PPCs with BRs demonstrated superior performance with larger V_{oc} and PCE. The best performance was exhibited by the device with a pyramidal nanotextured BR. Further design optimization, reduced thermalization loss, front metallization engineering, higher intensity laser illumination, and accounting for photon recycling could lead to simulated efficiencies over 50%.

The effects of variations in illumination wavelength and layer thicknesses on light absorption in thin PPCs with integrated BRs were studied using numerical simulations. Results show that thickness deviations of ~90 nm and ~100 nm for the absorber and FSF layers, respectively, cause a shift from constructive to destructive interference at the design wavelength. Multiple combinations of absorber and FSF layer thicknesses yield similar absorption at 1310 nm but with different absorption spectra and resonance widths. For the design with the narrowest resonance

width, absorption drops by 3.7-13.5% (abs.) for 10-20 nm deviations in the wavelength of the incident light, and by 1.5-7.1% (abs.) for the design with the broadest resonance width, under these conditions.

I explored design considerations for thin PPCs with pyramidal textured BRs using numerical simulations. The effect of variations in illumination wavelength and geometrical properties including layer thickness and nano pyramid dimensions were quantified. A 70 nm variation in device thickness can shift BR induced resonances from constructive to destructive interference and a 50 nm variation of the nano pyramid dimensions drops absorptance by more than 30% (absolute), which illustrates the precision required in the fabrication of high efficiency ultra-thin PPCs. Our results showed that multiple combinations of design space parameters yield similar absorptance at 1310 nm but with different absorptance spectra and resonance widths. Designs with overlapping resonances around the target wavelength combined with an ARC layer are less sensitive to the illuminated wavelength variations.

Single wavelength optimizations are faster and less computationally expensive, but only result in high absorptance at the wavelength of interest. In contrast, wide band wavelength optimization provides symmetric resonances around the target wavelength that result in designs with higher wavelength tolerance.

The approach proposed in this thesis can be applied to other illumination wavelengths, and the design principles outlined here can lead to better performing single and multi-junction PPCs.

7.2 Outlook

Currently, record PPC efficiencies of > 65% have been reported for wavelengths around 850 nm [25], [26]. The optical fiber attenuation loss at these wavelengths is ~3 dB/km (50% per kilometer)

which limits use of these devices to short-distance power-over-fiber transmission. The focus of this study was on the O-band telecommunications window near 1310 nm which provides much lower optical fiber attenuation loss of ~0.5 dB/km (11% per kilometer), resulting in potential for higher total system transmission efficiency in longer-reach future photonic power. However the minimum fiber loss lies at $\lambda \approx 1550$ nm (~0.5 dB/km, 5% per kilometer). The results of this work can be applied to development of PPCs for 1550 nm which would enable both longer distance power transmission and use of existing telecommunication equipment.

In this work, I applied numerical simulations to optimize ultra-thin PPC designs under narrow-band laser illumination at 1310 nm using the light trapping capability of flat BR and nanotextured BR with cubic and pyramidal structures. I also kept structures symmetric to avoid their polarization dependence. However, there are plenty of symmetric and asymmetric BR nanotexture types such as blazed gratings [114], skewed pyramids, nano cones [115], and cubes with zigzag or checkboard patterns [116], [117] that are worth examining and optimizing for trapping of monochromatic incident light.

Coupling the results of this work with machine learning techniques will accelerate the optimization of designs by minimizing computational cost and improving accuracy. This is especially relevant to designs with more extensive design space parameters such as thin PPCs with textured BRs and multijunction PPCs. It is also expected that the accuracy of these models would be improved by taking into account surface recombination in future simulations.

After optimizing these designs using simulations, the next step would be to fabricate and experimentally assess the performance of the proposed thin and ultra-thin PPCs with both flat and nanotextured BRs.

References

[1] J. B. Rosolem, *Power-Over-Fiber Applications for Telecommunications and for Electric Utilities*. IntechOpen, 2017. doi: 10.5772/68088.

[2] K. Worms *et al.*, "Reliable and lightning-safe monitoring of wind turbine rotor blades using optically powered sensors," *Wind Energy*, vol. 20, no. 2, pp. 345–360, 2017, doi: 10.1002/we.2009.

[3] M. M. Wilkins *et al.*, "Ripple-Free Boost-Mode Power Supply Using Photonic Power Conversion," *IEEE Trans. Power Electron.*, vol. 34, no. 2, pp. 1054–1064, Feb. 2019, doi: 10.1109/TPEL.2018.2843158.

[4] J. G. Werthen, M. J. Cohen, T.-C. Wu, and S. Widjaja, "Electrically Isolated Power Delivery for MRI Applications," in *Proc. Int. Soc. Magn. Reson. Med. Annu. Meeting*, Seattle, WA, 2006, p. 1353.

[5] D. Horwitz and R. Rickenbach, "Fiber Optic Sensors Enable New MRI Applications," *Medical Design and Outsourcing*, Jun. 16, 2014.

[6] C. Algora *et al.*, "Beaming power: Photovoltaic laser power converters for power-by-light," *Joule*, vol. 6, no. 2, pp. 340–368, Feb. 2022, doi: 10.1016/j.joule.2021.11.014.

[7] C. Algora and R. Peña, "Recharging the Battery of Implantable Biomedical Devices by Light," *Artif. Organs*, vol. 33, no. 10, pp. 855–860, 2009, doi: 10.1111/j.1525-1594.2009.00803.x.

[8] M. Schauerte, O. Höhn, T. Wierzkowski, G. Keller, and H. Helmers, "4-Junction GaAs Based Thin Film Photonic Power Converter with Back Surface Reflector for Medical Applications," in *2021 IEEE 48th Photovoltaic Specialists Conference (PVSC)*, Jun. 2021, pp. 1954–1959. doi: 10.1109/PVSC43889.2021.9518492.

[9] T. J. N. Jr and J. T. Kare, "Laser power beaming for defense and security applications," in *Unmanned Systems Technology XIII*, May 2011, vol. 8045, pp. 384–391. doi: 10.1117/12.886169.

[10] S. J. Wojtczuk, "Long-wavelength laser power converters for optical fibers," in *Conference Record of the Twenty Sixth IEEE Photovoltaic Specialists Conference - 1997*, Sep. 1997, pp. 971–974. doi: 10.1109/PVSC.1997.654250.

[11] https://powerlighttech.com/autonomous-vehicles

[12] L. Summerer and O. Purcell, "Concepts for wireless energy transmission via laser," Technical Report, Eur. Space Agency, 2009, p.10.

[13] J. Gowar, *Optical communication systems*, 2nd ed. New York: Prentice Hall, 1993.

[14] M. M. Rao, *Optical communication*. Universities press, 2001.

[15] W. M. Steen and J. Mazumder, *Laser Material Processing*. Springer Science & Business Media, 2010.

[16] H. Helmers, C. Armbruster, M. von Ravenstein, D. Derix, and C. Schöner, "6-W Optical Power Link With Integrated Optical Data Transmission," *IEEE Trans. Power Electron.*, vol. 35, no. 8, pp. 7904–7909, Aug. 2020, doi: 10.1109/TPEL.2020.2967475.

[17] S. Fafard *et al.*, "Ultrahigh efficiencies in vertical epitaxial heterostructure architectures," *Appl. Phys. Lett.*, vol. 108, no. 7, p. 071101, Feb. 2016, doi: 10.1063/1.4941240.

[18] Y. Zhao, Y. Sun, Y. He, S. Yu, and J. Dong, "Design and fabrication of six-volt vertically-stacked GaAs photovoltaic power converter," *Sci. Rep.*, vol. 6, no. 1, p. 38044, Dec. 2016, doi: 10.1038/srep38044.

[19] S. Hubbard, "Absorption and Generation," in *Photovoltaic Solar Energy*, John Wiley & Sons, Ltd, 2016, pp. 32–38. doi: 10.1002/9781118927496.ch4.

[20] M. Beattie, "Semiconductor Materials and Devices for High Efficiency Broadband and Monochromatic Photovoltaic Energy Conversion," Thesis, Université d'Ottawa / University of Ottawa, 2021. doi: 10.20381/ruor-26695.

[21] B. M. Kayes *et al.*, "27.6% Conversion efficiency, a new record for single-junction solar cells under 1 sun illumination," in *2011 37th IEEE Photovoltaic Specialists Conference*, Jun. 2011, pp. 000004–000008. doi: 10.1109/PVSC.2011.6185831.

[22] R. Saive, "Light trapping in thin silicon solar cells: A review on fundamentals and technologies," *Prog. Photovolt. Res. Appl.*, vol. 29, no. 10, pp. 1125–1137, 2021, doi: 10.1002/pip.3440.

[23] F. Cappelluti *et al.*, "Novel Concepts for High-Efficiency Lightweight Space Solar Cells," *E3S Web Conf.*, vol. 16, p. 03007, 2017, doi: 10.1051/e3sconf/20171603007.

[24] L. C. Hirst *et al.*, "Intrinsic radiation tolerance of ultra-thin GaAs solar cells," *Appl. Phys. Lett.*, vol. 109, no. 3, p. 033908, Jul. 2016, doi: 10.1063/1.4959784.

[25] S. Fafard and D. P. Masson, "74.7% Efficient GaAs-Based Laser Power Converters at 808 nm at 150 K," *Photonics*, vol. 9, no. 8, Art. no. 8, Aug. 2022, doi: 10.3390/photonics9080579.

[26] H. Helmers *et al.*, "68.9% Efficient GaAs-Based Photonic Power Conversion Enabled by Photon Recycling and Optical Resonance," *Phys. Status Solidi RRL – Rapid Res. Lett.*, vol. 15, no. 7, p. 2100113, 2021, doi: 10.1002/pssr.202100113.

[27] V. P. Khvostikov *et al.*, "Photovoltaic laser-power converter based on AlGaAs/GaAs heterostructures," *Semiconductors*, vol. 50, no. 9, pp. 1220–1224, Sep. 2016, doi: 10.1134/S1063782616090128.

[28] S. Fafard *et al.*, "High-photovoltage GaAs vertical epitaxial monolithic heterostructures with 20 thin p/n junctions and a conversion efficiency of 60%," *Appl. Phys. Lett.*, vol. 109, no. 13, p. 131107, Sep. 2016, doi: 10.1063/1.4964120.

[29] Y. Gou *et al.*, "1064 nm InGaAs metamorphic laser power converts with over 44% efficiency," *Opt. Express*, vol. 30, no. 23, pp. 42178–42185, Nov. 2022, doi: 10.1364/OE.474693.

[30] N. Singh, C. Kin Fai Ho, Y. Nelvin Leong, K. E. K. Lee, and H. Wang, "InAlGaAs/InP-Based Laser Photovoltaic Converter at 1070 nm," *IEEE Electron Device Lett.*, vol. 37, no. 9, pp. 1154–1157, Sep. 2016, doi: 10.1109/LED.2016.2591015.

[31] H. Helmers, A. Franke, D. Lackner, O. Höhn, F. Predan, and F. Dimroth, "51% Efficient Photonic Power Converters for O-Band Wavelengths around 1310 nm," in *2020 47th IEEE Photovoltaic Specialists Conference (PVSC)*, Jun. 2020, pp. 2471–2474. doi: 10.1109/PVSC45281.2020.9300717.

[32] S. Fafard and D. P. Masson, "High-Efficiency and High-Power Multijunction InGaAs/InP Photovoltaic Laser Power Converters for 1470 nm," *Photonics*, vol. 9, no. 7, Art. no. 7, Jul. 2022, doi: 10.3390/photonics9070438.

[33] J. Mukherjee, S. Jarvis, M. Perren, and S. J. Sweeney, "Efficiency limits of laser power converters for optical power transfer applications," *J. Phys. Appl. Phys.*, vol. 46, no. 26, p. 264006, Jun. 2013, doi: 10.1088/0022-3727/46/26/264006.

[34] K. R. Catchpole and A. Polman, "Plasmonic solar cells," *Opt. Express*, vol. 16, no. 26, pp. 21793–21800, Dec. 2008, doi: 10.1364/OE.16.021793.

[35] S. Mokkapati, F. J. Beck, A. Polman, and K. R. Catchpole, "Designing periodic arrays of metal nanoparticles for light-trapping applications in solar cells," *Appl. Phys. Lett.*, vol. 95, no. 5, p. 053115, Aug. 2009, doi: 10.1063/1.3200948.

[36] Y. Park *et al.*, "Absorption enhancement using photonic crystals for silicon thin film solar cells," *Opt. Express*, vol. 17, no. 16, pp. 14312–14321, Aug. 2009, doi: 10.1364/OE.17.014312.

[37] J. Mayer, B. Gallinet, T. Offermans, and R. Ferrini, "Diffractive nanostructures for enhanced light-harvesting in organic photovoltaic devices," *Opt. Express*, vol. 24, no. 2, pp. A358–A373, Jan. 2016, doi: 10.1364/OE.24.00A358.

[38] S. C. Baker-Finch and K. R. McIntosh, "Reflection of normally incident light from silicon solar cells with pyramidal texture," *Prog. Photovolt. Res. Appl.*, vol. 19, no. 4, pp. 406–416, 2011, doi: 10.1002/pip.1050.

[39] H. D. Omar, Md. R. Hashim, and M. Z. Pakhuruddin, "Ray tracing of inverted pyramids for light-trapping in thin crystalline silicon for solar cells," *Optik*, vol. 219, p. 165279, Oct. 2020, doi: 10.1016/j.ijleo.2020.165279.

[40] K. X. Wang, Z. Yu, V. Liu, Y. Cui, and S. Fan, "Absorption Enhancement in Ultrathin Solar Cells with Antireflection and Light-Trapping Nanocone Gratings," in *Renewable Energy and the Environment Optics and Photonics Congress*, Eindhoven, 2012, p. PT2C.2. doi: 10.1364/PV.2012.PT2C.2.

[41] L. Wen, Z. Zhao, X. Li, Y. Shen, H. Guo, and Y. Wang, "Theoretical analysis and modeling of light trapping in high efficicency GaAs nanowire array solar cells," *Appl. Phys. Lett.*, vol. 99, no. 14, p. 143116, Oct. 2011, doi: 10.1063/1.3647847.

[42] N. Vandamme *et al.*, "Ultrathin GaAs Solar Cells With a Silver Back Mirror," *IEEE J. Photovolt.*, vol. 5, no. 2, pp. 565–570, Mar. 2015, doi: 10.1109/JPHOTOV.2014.2371236.

[43] M. I. Hossain, W. Qarony, M. K. Hossain, M. K. Debnath, M. J. Uddin, and Y. H. Tsang, "Effect of back reflectors on photon absorption in thin-film amorphous silicon solar cells," *Appl. Nanosci.*, vol. 7, no. 7, pp. 489–497, Oct. 2017, doi: 10.1007/s13204-017-0582-y.

[44] V. E. Ferry *et al.*, "Light trapping in ultrathin plasmonic solar cells," *Opt. Express*, vol. 18, no. 102, pp. A237–A245, Jun. 2010, doi: 10.1364/OE.18.00A237.

[45] Y. S. Peng and S. F. Gong, “Light-trapping structure based on ultra-thin GaAs solar cell,” *J. Phys. Appl. Phys.*, vol. 53, no. 49, p. 495107, Oct. 2020, doi: 10.1088/1361-6463/abb434.

[46] A. Peter Amalathas and M. M. Alkaisi, “Nanostructures for Light Trapping in Thin Film Solar Cells,” *Micromachines*, vol. 10, no. 9, Art. no. 9, Sep. 2019, doi: 10.3390/mi10090619.

[47] M. S. Kim, J. H. Lee, and M. K. Kwak, “Review: Surface Texturing Methods for Solar Cell Efficiency Enhancement,” *Int. J. Precis. Eng. Manuf.*, vol. 21, no. 7, pp. 1389–1398, Jul. 2020, doi: 10.1007/s12541-020-00337-5.

[48] Y. Takeda, “Light trapping for photovoltaic cells used for optical power transmission,” *Appl. Phys. Express*, vol. 13, no. 5, p. 054001, May 2020, doi: 10.35848/1882-0786/ab8056.

[49] W. Yang *et al.*, “Ultra-thin GaAs single-junction solar cells integrated with a reflective back scattering layer,” *J. Appl. Phys.*, vol. 115, no. 20, p. 203105, May 2014, doi: 10.1063/1.4878156.

[50] N. P. Irvin *et al.*, “Monochromtic light trapping in photonic power converters,” in *2022 49th IEEE Photovoltaic Specialists Conference (PVSC)*, Philadelphia, 2022, pp. 0143-0143, doi: 10.1109/PVSC48317.2022.9938800.

[51] D. Masson, F. Proulx, and S. Fafard, “Pushing the limits of concentrated photovoltaic solar cell tunnel junctions in novel high-efficiency GaAs phototransducers based on a vertical epitaxial heterostructure architecture,” *Prog. Photovolt. Res. Appl.*, vol. 23, no. 12, pp. 1687–1696, 2015, doi: 10.1002/pip.2709.

[52] S. Fafard and D. P. Masson, “Perspective on photovoltaic optical power converters,” *J. Appl. Phys.*, vol. 130, no. 16, p. 160901, Oct. 2021, doi: 10.1063/5.0070860.

[53] M. N. Beattie and K. Hinzer, “Extending the reach of photonic power,” *Compound Semiconductor*, vol. 25, no. 7, pp. 56–63, 2019.

[54] M. Beattie, H. Helmers, C. E. Valdivia, D. Lackner, O. Höhn, and K. Hinzer, “Non-Uniform Illumination Impacts on O-Band InGaAsP and Metamorphic GaInAs Photonic Power Converters,” in *3rd Optical Wireless and Fiber Power Transmission Conference, OWPT 2021. Technical Digest*, 2021, pp. 37–38.

[55] J. D. López-Cardona, D. Sánchez Montero, and C. Vázquez, “Smart Remote Nodes Fed by Power Over Fiber in Internet of Things Applications,” *IEEE Sens. J.*, vol. 19, no. 17, pp. 7328–7334, Sep. 2019, doi: 10.1109/JSEN.2019.2915613.

[56] Z. Cheng and D. M. O’Carroll, “Photon Recycling in Semiconductor Thin Films and Devices,” *Adv. Sci.*, vol. 8, no. 20, p. 2004076, 2021, doi: 10.1002/advs.202004076.

[57] M. P. Lumb, M. A. Steiner, J. F. Geisz, and R. J. Walters, “Incorporating photon recycling into the analytical drift-diffusion model of high efficiency solar cells,” *J. Appl. Phys.*, vol. 116, no. 19, p. 194504, Nov. 2014, doi: 10.1063/1.4902320.

[58] I. Massiot, A. Cattoni, and S. Collin, “Progress and prospects for ultrathin solar cells,” *Nat. Energy*, vol. 5, no. 12, pp. 959–972, 2020.

[59] A. Rockett, *The Materials Science of Semiconductors*. Boston, MA: Springer US, 2008. doi: 10.1007/978-0-387-68650-9.

[60] R. F. Pierret and G. W. Neudeck, *Advanced semiconductor fundamentals*, vol. 6. Addison-Wesley Reading, MA, 1987.

[61] M. Massimi, *Pauli's Exclusion Principle: The Origin and Validation of a Scientific Principle*. Cambridge University Press, 2005.

[62] R. A. Serway, J. W. Jewett, *Physics for Scientists and Engineers with Modern Physics*, Brooks/Cole, 2010.

[63] P. Zaleski-Ejgierd, "Computational studies on new chemical species in the gas-phase and the solid-state," Thesis, University of Helsinki, 2009.

[64] N. Large, "Resonant Raman-Brillouin scattering in semiconductor and metallic nanostructures: from nano-acoustics to acousto-plasmonics," Thesis, Université de Toulouse/ Université Toulouse, 2011.

[65] S. R. Wenham, M. A. Green, M. E. Watt, R. Corkish, and A. Sproul, Eds., *Applied Photovoltaics*, 3rd ed. London: Routledge, 2011. doi: 10.4324/9781849776981.

[66] G. Dhanaraj, et al., *Springer handbook of Crystal Growth*, Springer, 2010.

[67] M. C. Gupta and J. Ballato, *The Handbook of Photonics*. CRC Press, 2018.

[68] Ben, "Why is the Fermi level (energy) shifited in doped semiconductors?," *Physics Stack Exchange*, Aug. 17, 2019. https://physics.stackexchange.com/q/497337.

[69] W. Raja *et al.*, "Photon recycling in perovskite solar cells and its impact on device design," *Nanophotonics*, vol. 10, no. 8, pp. 2023–2042, Jun. 2020, doi: 10.1515/nanoph-2021-0067.

[70] J. A. Nelson, *The Physics Of Solar Cells*. World Scientific Publishing Company, 2003.

[71] D. A. Neamen, *Semiconductor physics and devices: basic principles*. McGraw-hill, 2003.

[72] M. N. Beattie *et al.*, "Two-Junction III-V Photonic Power Converter Operating At Monochromatic Telecom Wavelengths," in *2020 47th IEEE Photovoltaic Specialists Conference (PVSC)*, Jun. 2020, pp. 1062–1066. doi: 10.1109/PVSC45281.2020.9300885.

[73] A. McEvoy, T. Markvart, and L. Castaner, *Practical Handbook of Photovoltaics: Fundamentals and Applications*. Elsevier, 2003.

[74] M. Zamiri, *et al.*, "Design for fabrication of high efficiency 1310 nm photonic power converter", in *19th International Conference on Numerical Simulation of Optoelectronic Devices (NUSOD)*, Ottawa, ON, July 8 to 12, 2019.

[75] H.-L. Chen *et al.*, "A 19.9%-efficient ultrathin solar cell based on a 205-nm-thick GaAs absorber and a silver nanostructured back mirror," *Nat. Energy*, vol. 4, no. 9, pp. 761–767, Sep. 2019, doi: 10.1038/s41560-019-0434-y.

[76] J. Piprek, *Handbook of Optoelectronic Device Modeling and Simulation: Lasers, Modulators, Photodetectors, Solar Cells, and Numerical Methods, Vol. 2*. CRC Press, 2017.

[77] https://www.lumerical.com

[78] J. A. Kong, *Electromagnetic wave theory*. Cambridge, MA: EMW Publishing, 2000.

[79] Kane Yee, “Numerical solution of initial boundary value problems involving maxwell’s equations in isotropic media,” *IEEE Trans. Antennas Propag.*, vol. 14, no. 3, pp. 302–307, May 1966, doi: 10.1109/TAP.1966.1138693.

[80] S. C. Hagness, A. Taflove, and S. D. Gedney, “Finite-Difference Time-Domain Methods,” in *Handbook of Numerical Analysis*, vol. 13, Elsevier, 2005, pp. 199–315. doi: 10.1016/S1570-8659(04)13003-2.

[81] https://www.slideshare.net/physicsImposible/fdtd-12204904

[82] R. Eberhart and J. Kennedy, “A new optimizer using particle swarm theory,” in *MHS’95. Proceedings of the Sixth International Symposium on Micro Machine and Human Science*, 1995, pp. 39–43.

[83] https://towardsdatascience.com/particle-swarm-optimization-visually-explained-289eeb2e14

[84] D. Wang, D. Tan, and L. Liu, “Particle swarm optimization algorithm: an overview,” *Soft Comput.*, vol. 22, no. 2, pp. 387–408, 2018.

[85] E. D. Palik, *Handbook of optical constants of solids*. Academic press, 1998.

[86] T. K. Chong, J. Wilson, S. Mokkapati, and K. R. Catchpole, “Optimal wavelength scale diffraction gratings for light trapping in solar cells,” *J. Opt.*, vol. 14, no. 2, p. 024012, Feb. 2012, doi: 10.1088/2040-8978/14/2/024012.

[87] C. K. Williams, T. H. Glisson, J. R. Hauser, and M. A. Littlejohn, “Energy bandgap and lattice constant contours of iii-v quaternary alloys of the form Ax By Cz D or ABx Cy Dz.,” *J. Electron. Mater.*, vol. 7, pp. 639–646, 1978.

[88] T. Mei, “Interpolation of quaternary III-V alloy parameters with surface bowing estimations,” *J. Appl. Phys.*, vol. 101, no. 1, p. 013520, Jan. 2007, doi: 10.1063/1.2404791.

[89] M. Levinshtein, *Handbook Series on Semiconductor Parameters*. World Scientific, 1997.

[90] R. K. Ahrenkiel, R. Ellingson, S. Johnston, and M. Wanlass, “Recombination lifetime of In0.53Ga0.47As as a function of doping density,” *Appl. Phys. Lett.*, vol. 72, no. 26, pp. 3470–3472, Jun. 1998, doi: 10.1063/1.121669.

[91] A. Schenk, “Finite-temperature full random-phase approximation model of band gap narrowing for silicon device simulation,” *J. Appl. Phys.*, vol. 84, no. 7, pp. 3684–3695, Oct. 1998, doi: 10.1063/1.368545.

[92] J. W. Slotboom, “The pn-product in silicon,” *Solid-State Electron.*, vol. 20, no. 4, pp. 279–283, Apr. 1977, doi: 10.1016/0038-1101(77)90108-3.

[93] N. Nouri, *et al.*, “Simulation of Thin High-Efficiency Photonic Power Converters Under 1310 nm Laser Illumination,” in *19th International Conference on Numerical Simulation of Optoelectronic Devices (NUSOD)*, Ottawa, ON, July 8 to 12, 2019.

[94] R. Rockstuhl, C., Lederer, F., Bittkau, K., & Carius, “Light localization at randomly textured surfaces for solar-cell applications,” vol. 171104, no. September, pp. 89–92, 2007, doi: 10.1063/1.2800374.

[95] N. Nouri, C. E. Valdivia, Meghan. N. Beattie, M. S. Zamiri, and K. Hinzer, “Thin Photonic Power Converters Designs with Back Reflector Operating at a 1310 nm Wavelength,” in *2020 47th IEEE Photovoltaic Specialists Conference (PVSC)*, Jun. 2020, pp. 2359–2362. doi: 10.1109/PVSC45281.2020.9300435.

[96] N. Nouri, *et al*., “Ultrathin monochromatic photonic power converters with nanostructured nm laser illumination-ng of 1310back mirror for light trappi,” presented at the *In Physics, Simulation, and Photonic Engineering of Photovoltaic Devices X; International Society for Optics and Photonics,* Bellingham, WA, USA, 2021.

[97] N. Nouri, C. E. Valdivia, M. N. Beattie, J. J. Krich, and K. Hinzer, “Light management in ultra-thin photonic power converters for 1310 nm laser illumination,” *Opt. Express*, vol. 30, no. 13, p. 23417, Jun. 2022, doi: 10.1364/OE.459680.

[98] K. Ali, S. A. Khan, and M. Z. M. Jafri, “Effect of Double Layer (SiO2/TiO2) Anti-reflective Coating on Silicon Solar Cells,” *Int J Electrochem Sci*, vol. 9, p. 10, 2014.

[99] N. Nouri *et al.*, “Tolerance Study of Thin Photonic Power Converters with Planar Back Reflectors,” in *The 4th Optical Wireless and Fiber Power Transmission Conference (OWPT)*, Yokohama, Japan, 2022.

[100] N. Nouri, C. E. Valdivia, M. N. Beattie, J. J. Krich and K. Hinzer, "Optical Design Considerations for Thin Photonic Power Converters with Textured Back Reflector," *2022 IEEE 49th Photovoltaics Specialists Conference (PVSC)*, 2022, pp. 1295-1298, doi: 10.1109/PVSC48317.2022.9938646.

[101] N. I. Khan, S. H. Choudhury, and A. A. Roni, “A comparative study of the temperature dependence of lasing wavelength of conventional edge emitting stripe laser and vertical cavity surface emitting laser,” in *Proceedings of the International Conference on Data Communication Networking and Optical Communication System*, Seville, Spain, 2011, pp. 1–5. doi: 10.5220/0003512101410145.

[102] C. E. R. Disney, S. Pillai, and M. A. Green, “The Impact of parasitic loss on solar cells with plasmonic nano-textured rear reflectors,” *Sci. Rep.*, vol. 7, no. 1, p. 12826, Dec. 2017, doi: 10.1038/s41598-017-12896-1.

[103] M. N. Beattie, H. Helmers, G. P. Forcade, C. E. Valdivia, O. Höhn, and K. Hinzer, “InP- and GaAs-Based Photonic Power Converters Under O-Band Laser Illumination: Performance Analysis and Comparison,” *IEEE J. Photovolt.*, pp. 1–9, 2022, doi: 10.1109/JPHOTOV.2022.3218938.

[104] D. Xia, M. M. Wilkins, S. S. Chahal, C. E. Valdivia, K. Hinzer, and J. J. Krich, “Opportunities for Increased Efficiency in Monochromatic Photovoltaic Light Conversion,” in *2018 IEEE 7th World Conference on Photovoltaic Energy Conversion (WCPEC) (A Joint Conference of 45th IEEE PVSC, 28th PVSEC & 34th EU PVSEC)*, Waikoloa Village, HI, Jun. 2018, pp. 3688–3692. doi: 10.1109/PVSC.2018.8547912.

[105] P. Sharma, A. W. Walker, J. F. Wheeldon, K. Hinzer, and H. Schriemer, “Enhanced Efficiencies for High-Concentration, Multijunction PV Systems by Optimizing Grid Spacing under Nonuniform Illumination,” *Int. J. Photoenergy*, vol. 2014, pp. 1–7, 2014, doi: 10.1155/2014/582083.

[106] D. Xia and J. J. Krich, “Efficiency Increase in Multijunction Monochromatic Photovoltaic Devices Due to Luminescent Coupling,” *J. Appl. Phys.*, vol. 128, no. 1, p. 013101, Jul. 2020, doi: 10.1063/5.0009870.

[107] B. Behaghel *et al.*, “Absorption enhancement through Fabry-Pérot resonant modes in a 430 nm thick InGaAs/GaAsP multiple quantum wells solar cell,” *Appl. Phys. Lett.*, vol. 106, no. 8, p. 081107, Feb. 2015, doi: 10.1063/1.4913469.

[108] S. Y. Chou, P. R. Krauss, and P. J. Renstrom, “Nanoimprint lithography,” *J Vac Sci Technol B*, vol. 14, no. 6, p. 6, 1996.

[109] M. C. Traub, W. Longsine, and V. N. Truskett, “Advances in Nanoimprint Lithography,” *Annu. Rev. Chem. Biomol. Eng.*, vol. 7, no. 1, pp. 583–604, 2016, doi: 10.1146/annurev-chembioeng-080615-034635.

[110] M. Zawierta *et al.*, “Control of Sidewall Profile in Dry Plasma Etching of Polyimide,” *J. Microelectromechanical Syst.*, vol. 26, no. 3, pp. 593–600, Jun. 2017, doi: 10.1109/JMEMS.2017.2681106.

[111] de Lafontaine, Mathieu, et al. “Influence of plasma process on III-V/Ge multijunction solar cell via etching, ” *Solar Energy Materials and Solar Cells* 195 (2019): 49-54.

[112] N. Gerges, C. Petit-Etienne, M. Panabière, J. Boussey, Y. Ferrec, and C. Gourgon, “Optimized ultraviolet grayscale process for high vertical resolution applied to spectral imagers,” *J. Vac. Sci. Technol. B*, vol. 39, no. 6, p. 062602, Dec. 2021, doi: 10.1116/6.0001273.

[113] I. W. Rangelow, “Critical tasks in high aspect ratio silicon dry etching for microelectromechanical systems,” *J. Vac. Sci. Technol. Vac. Surf. Films*, vol. 21, no. 4, pp. 1550–1562, Jul. 2003, doi: 10.1116/1.1580488.

[114] T. Aho *et al.*, “Metal/Polymer Back Reflectors with Diffraction Gratings for Light Trapping in III-V Solar Cells,” in *2018 IEEE 7th World Conference on Photovoltaic Energy Conversion (WCPEC) (A Joint Conference of 45th IEEE PVSC, 28th PVSEC & 34th EU PVSEC)*, Jun. 2018, pp. 2847–2851. doi: 10.1109/PVSC.2018.8547661.

[115] B. Hua, Q. Lin, Q. Zhang, and Z. Fan, “Efficient photon management with nanostructures for photovoltaics,” *Nanoscale*, vol. 5, no. 15, p. 6627, 2013, doi: 10.1039/c3nr01152f.

[116] K. Li *et al.*, “Light trapping in solar cells: simple design rules to maximize absorption,” *Optica*, vol. 7, no. 10, p. 1377, Oct. 2020, doi: 10.1364/OPTICA.394885.

[117] O. Höhn *et al.*, "Realization of Ultrathin GaAs Photonic Power Converters with Rear-Side Metal Grating on Full 4” Wafers," *2022 IEEE 49th Photovoltaics Specialists Conference (PVSC)*, 2022, pp. 0038-0042, doi: 10.1109/PVSC48317.2022.9938600.

Appendix

This appendix describes how SRH, Auger and radiative recombination processes are modeled in the commercial software Lumerical FDTD that was employed in this thesis.

1.Trap-Assisted (Shockley-Read-Hall) recombination

$$R_{SRH} = \frac{np - n_i^2}{\tau_p(n + n_1) + \tau_n(p + p_1)}$$

where τ_n and τ_p are the electron and hole lifetimes, respectively, and n_1 and p_1 are the effective densities of carriers in the trap states (E_t). While carrier lifetimes are taken as an input, the constants n_1 and p_1 are calculated as:

$$n_1 = n_i exp(E_t/k_B T)$$

$$p_1 = n_i exp(-E_t/k_B T)$$

where n_i is the intrinsic carrier density, E_t is the trap state energy, k_B is the Boltzmann constant, and T is the temperature.

2. Auger recombination

$$R_{aug} = \left(C_n n + C_p p\right)(np - n_i^2)$$

where C_n and C_p are electron and holes capture rate coefficient for Auger recombination, n and p are electron and hole carrier densities, and n_i is the intrinsic carrier density.

3. Radiative recombination

$$R_{rad} = B_{rad}(np - n_i^2)$$

where B_{rad} is the capture rate coefficient for radiative recombination, n and p are electron and hole carrier densities, and n_i is the intrinsic carrier density.